Fall 12-20-2018

Dynamic Response of a Hingeless Helicopter Rotor Blade at Hovering and Forward Flights

Pratik Sarker
psarker1@uno.edu

Dynamic Response of a Hingeless Helicopter Rotor Blade at Hovering and Forward Flights

A Dissertation

Submitted to the Graduate Faculty of the
University of New Orleans
in partial fulfillment of the
requirements for the degree of

Doctor of Philosophy
in
Engineering and Applied Sciences
Mechanical Engineering

by

Pratik Sarker

B.S. Bangladesh University of Engineering and Technology, 2007
M.S. University of New Orleans, 2014

December, 2018

Dedication

To

My Father

who taught me never to lose hope and always try to the end without expecting anything for

earning an honest living

My Mother

who always encouraged me to listen to my mind to do things as I think good and to have faith on me

and lastly

My Beloved Wife

who continuously kept supporting me in my very hard time to conduct this research

Acknowledgment

First of all, I would like to express my sincere gratitude to my advisor, Dr. Uttam K Chakravarty for the continuous support to my Ph.D. study and research and for his patience, motivation, enthusiasm, and immense knowledge. I am especially thankful for his guidance on fostering my professional problem-analyzing, problem-solving, and reporting skills. His guidance helped me all the time for continuing the research and writing this dissertation.

Besides my advisor, I would like to thank the rest of my dissertation committee members—Dr. Paul J Schilling, Dr. Martin J Guillot, Dr. Lothar Birk, and Dr. Leszek Malkinski for their consents to be my Ph.D. dissertation committee members. I am also grateful to Dr. Kazim M Akyuzlu and Dr. David Hui for their valuable advice and guidance regarding my dissertation.

I thank my fellow lab mates in the University of New Orleans Computational Solid Mechanics Group—Manohar Chidurala and Jose Enrique Rubio for the stimulating discussions and for all the fun we had in the past years. Also I express my heartiest thanks to my friends in the same group M Shafiqur Rahman, Mohammad Khairul Habib Pulok, Md Mosleh Uddin, Iftekhar Alam Riyad, Debabrata Mondal, Anvesh Nallabali, and Sri Charan Reddy Gudigopuram for their generous support to write this dissertation.

Last but not the least, I would like to thank my family: my parents Sribash Chandra Sarker and Dharitri Sarker for giving birth to me at the first place and supporting me throughout my life and my wife Sunita Roy for her great patience to be with me in this long journey, without whose support, it would not be possible for me to successfully finish this dissertation.

This research is supported by the NASA EPSCoR Research Infrastructure Development (RID) grant, contract no. LEQSF-EPS (2015)-RAP-17.

Table of Contents

Nomenclature

Symbols

A, B, C	terms used for local notations
$A_{11}, A_{12}, A_{22}, A_{66}$	elements of the extensional stiffness matrix of a composite laminate
A_c	cross-sectional area
$A_{c_{core}}, A_{c_{shell}}$	cross-sectional area of the composite core, the composite shell
A_d	rotor disk area
A_{c_h}, A_{c_r}	cross-sectional area of the Honeycomb structure, the Rohacell foam
A_n	coefficient related to the initial condition
B_n	coefficient related to the initial condition
B_{shell}	extensional stiffness of the composite shell per unit width
$C(k)$	Theodorsen's lift deficiency function
C_T	thrust coefficient
D	aerodynamic drag force per unit length acting through the aerodynamic center
D_b	bending stiffness
D_{bNA}	out-of-plane bending stiffness with respect to the neutral axis
D_{by}, D_{bz}	out-of-plane, in-plane bending stiffness with respect to global y axis, global z axis through the shear center
$D_{b\bar{y}_p}, D_{b\bar{z}_p}$	out-of-plane, in-plane bending stiffness with respect to principal $\bar{y}_p$ axis, $\bar{z}_p$ axis through the centroid
D_t	torsional stiffness about the shear center/elastic axis/global x axis
E	elastic modulus of the isotropic material
E_1, E_2	elastic modulus of the composite shell in the fiber direction, in the transverse direction
E_r, E_h	elastic modulus of the isotropic Honeycomb structure, the isotropic Rohacell foam
E_{core}, E_{shell}	equivalent extensional elastic modulus of the composite core, the composite shell
F	function before the decoupling of the governing equations
F_1, F_2, F_3	generalized forces along axes 1, 2, 3
F_Y, F_Z	total in-plane force per unit length acting along Y axis, out-of-plane force per unit length acting along Z axis through the aerodynamic center

F_{yn}, F_{zn}	terms used for local notations
F_{yng}, F_{zng}	n^{th} generalized force for out-of-plane bending/flapping, in-plane bending/lead-lag motion
G	function after the decoupling of the governing equations
G_{12}	in-plane shear modulus of the composite shell
G_{core}, G_{shell}	equivalent shear modulus of the composite core, the composite shell
H	function representing initial displacement
I_{NA}	area moment of inertia with respect to the neutral axis
$I_{NA_{core}}$, $I_{NA_{shell}}$	area moment of inertia of the composite core, the composite shell with respect to the neutral axis
$\bar{I}_p$	area moment of inertia with respect to the principal centroidal axis
$\bar{I}_{y_p}$, $\bar{I}_{z_p}$	area moment of inertia about the principal centroidal $\bar{y}_p$ axis, $\bar{z}_p$ axis
$\bar{I}_{z_{p_{core}}}$, $\bar{I}_{z_{p_{shell}}}$	area moment of inertia about the principal centroidal $\bar{z}_p$ axis for the composite core, the composite shell
K	function representing initial velocity
L	aerodynamic lift force per unit length acting through the aerodynamic center
L_s	steady lift term used for local notation
L_v	local function of w, v, and θ
L_w	local function of w, v, and θ
L_θ	local function of w, v, and θ
M	number of points considered on the beam/helicopter rotor blade
M_1, M_2, M_3	generalized moments about axes 1, 2, 3
M_A, M_{ac}	pitching moment about the aerodynamic center/centroid of the cross-section
M_{xn}	term used for local notation
M_{xng}	n^{th} generalized moment for torsional motion
M_y, M_z	bending moments about global y axis, global z axis
N	total number of degrees of freedom at point i on the beam/helicopter rotor blade after discretization
P_1, P_2	parameters in the forcing functions for numerical model validation
Q	torque about the global x axis/elastic axis
R	rotor radius

S_y, S_z	cross-sectional shear force along global y axis, global z axis
T	centrifugal tension in the rotor blade due to rotation of the blade
T_h	total thrust generated by the helicopter in the hovering flight
V_∞	level forward speed of the helicopter
V_{NE}	never exceed level forward speed of the helicopter
V_m, V_n	m^{th}, n^{th} normal mode due to in-plane bending/lead-lag motion
V_g	general velocity parallel to the rotor disk plane
V_{tip}	linear in-plane velocity at the tip of the rotor blade
W_m, W_n	m^{th}, n^{th} normal mode due to out-of-plane bending/flapping motion
W_g	total gross weight of the helicopter
X_1, X_2, Y_1, Y_2	local definite integrals
X_{1nf}, X_{1nt}, Y_{1nf}, Y_{1nt}	X_1 containing ω_{nf}, X_1 containing ω_{nt}, Y_1 containing ω_{nf}, and Y_2 containing ω_{nt}
a	lift curve slope
a_n	orthogonality constant corresponding to out-of-plane bending/flapping mode
a_{nf}, a_{nt}	values of a_n corresponding to ω_{nf}, ω_{nt}
b_n	orthogonality constant corresponding to in-plane bending/lead-lag mode
c	chord length of the airfoil
c_0, c_1	empirically derived coefficients
c_h, c_v	coordinate axis of the proposed cross-sectional profile of the blade parallel to the chord, perpendicular to the chord
c_{h1}, c_{v1}	known coordinates of the points on the outermost surface of the proposed cross-sectional profile along c_h axis, c_v axis
c_{h2}, c_{v2}	unknown coordinates of the points on the reference surface of the proposed cross-sectional profile along c_h axis, c_v axis
c_n	orthogonality constant corresponding to torsional mode
c_{nf}, c_{nt}	values of c_n corresponding to ω_{nf}, ω_{nt}
$c_{v_{lref}}$, $c_{v_{uref}}$	ordinate of the point on the upper reference curve, lower reference curve
$c_{v_{lower}}$, $c_{v_{upper}}$	ordinate of the point on the outermost lower, outermost upper surface along c_v axis from the centroid of the whole composite cross-section
Δc_h	distance between c_{h1} and c_{h2} along c_h axis
Δc_v	distance between c_{v1} and c_{v2} along c_v axis

d	distance between the neutral axis and the centroidal axis
$\bar{d}$	distance of the centroidal axis measured from c_h axis
d_0, d_1, d_2	empirically derived coefficients
d_{core}, d_{shell}	distance between the neutral axis and the centroidal axis of the cross-section of the composite core, the composite shell
d_r	radial distance between the outermost surface and the reference surface of the composite shell
e	distance between the centroid and the shear center of the cross-section of the beam/helicopter rotor blade, positive when the shear center is behind the centroid
e_1	distance between the fixed end and the axis of rotation of the beam/helicopter rotor blade
f_{nf}	n^{th} natural frequency governed by out-of-plane bending/flapping motion in Hz
f_{nl}	n^{th} natural frequency governed by in-plane bending/lead-lag motion in Hz
f_{nt}	n^{th} natural frequency governed by torsional motion in Hz
f_y	external force per unit length on the helicopter blade along global y axis
f_z	external force per unit length on the helicopter blade along global z axis
h	segment length of the beam after discretization
h_1, h_2	distance of the topmost point, the bottommost point, from the neutral axis of the proposed cross-section
$h_{airfoil}$	the maximum thickness of the NACA 23012 airfoil
h_p	downward displacement of the elastic axis
h_{shell}	total thickness of the composite shell
i	index representing location of points along the global x axis/elastic axis
j	complex number
k	index representing the number of degrees-of-freedom at point i on the beam after discretization
k_x, k_y	weighting factors in the Drees's inflow model representing the deviation of the inflow from the uniform value
l	length of the beam/helicopter rotor blade
l_1, l_2	lower limit, upper limit of integration for the reference curves
m	mass per unit length of the beam/helicopter rotor blade
m_0, m_1	empirically derived coefficients

m_i	mass per unit length of a constituent beam having i^{th} cross-section that makes up proposed whole composite cross-section
m_x	external torque per unit length about the global x axis/elastic axis
p_{ki}	degree-of-freedom at point i ($k = 1,2, \dots N; p_{1i} = w; p_{2i} = v; p_{3i} = \theta; \dots$)
q_n	generalized time coordinate for the n^{th} mode
s_{lref}, s_{uref}	arc length of the lower reference curve, upper reference curve
t	time
u	generalized deflection
u_p	air velocity perpendicular to the rotor disk plane
u_t	linear blade velocity parallel to the rotor disk plane
v	in-plane bending deflection along global y axis
v_c	climbing velocity of the helicopter
v_i	general induced/inflow velocity at the rotor disk
w	out-of-plane bending deflection along global z axis
x, y, z	global x axis or elastic axis/spatial variable along global x axis or elastic axis, global y axis, global z axis
x_1, y_1, z_1	x_1 axis, y_1 axis, z_1 axis with origin at the center of rotation; the global x axis coincides with x_1 axis if extended into the axis of rotation, y_1 axis is parallel to the global y axis, and z_1 axis coincides with the axis of rotation
$\bar{y}_p$, $\bar{z}_p$	principal axes through the centroid of the proposed composite cross-section
Θ_m, Θ_n	m^{th}, n^{th} normal mode due to torsional motion
Ω	angular velocity/rotational speed of the rotor blade in rad/s
α	total blade cross-section angle at any station x prior to any deformation
α_{1c}	lateral cyclic pitch angle
α_{1s}	longitudinal cyclic pitch angle
α_a	angle of attack
α_i	total blade cross-section angle at any station x_i prior to any deformation
α_{in}	inflow angle at the blade cross-section, $tan^{-1}(u_p/u_t)$
α_{p0}	collective pitch angle/collective pitch input, positive when leading edge is upward
α_p	pitching angle of the rotor blade, positive when leading edge is upward
α_s	angle between the hub plane and forward velocity direction/disk angle of attack

α_t	pretwist angle of the beam/helicopter rotor blade, positive when rotated counterclockwise/leading edge is upward
$\alpha_{t_{cr}}$	pretwist angle that the beam/helicopter rotor blade would have if extended into the center of rotation
$\alpha_{t_{root}}$, $\alpha_{t_{tip}}$	pretwist angle of the beam/helicopter rotor blade at the root, at the tip
α_v	angle between the vertical and the common normal perpendicular to the tangents at two different points on two curves of the proposed cross-sectional profile/slope angle
$\Delta\alpha_t$	angle of twist or washout between the center of rotation and the tip of the beam/helicopter rotor blade
β_f	flapping angle measured between the hub plane and the deformed blade
β_g	general time-dependent pitch angle
$\beta_n l$	root of the characteristic equation of transverse vibration of a cantilever beam
γ	torsional constant of a cross-section
γ_{core}, γ_{shell}	torsional constant of the composite core, the composite shell
δ	Kronecker delta
η, ξ	principal axes through the shear center of the cross-section of the beam/helicopter rotor blade at an angle α with global y-z axis system
θ	torsional deflection about the elastic axis, positive when rotated counterclockwise/leading edge is upward
θ_0	collective pitch angle
θ_{1c}	lateral cyclic pitch angle
θ_{1s}	longitudinal cyclic pitch angle
κ_m	polar mass radius of gyration about the elastic axis/global x axis
κ_{m1}, κ_{m2}	mass radius of gyration about the neutral axis, the axis normal to chord through the shear center
λ	total rotor inflow ratio, positive downward through the rotor disk
λ_0	rotor mean induced inflow ratio
λ_i	rotor induced inflow ratio
μ	advance ratio
ν	Poisson's ratio of an isotropic material
ν_{12}	major Poisson's ratio of the composite
ρ	density of material
τ	time

σ	rotor solidity/solidity ratio
ϕ_{nb}, ϕ_{nbr}	normal function governing out-of-plane/in-plane bending motion of a nonrotating beam, rotating beam
ϕ_{nt}	normal function governing torsional motion of a beam
ψ	azimuth angle of the rotor blade/nondimensional time, Ωt
ω	natural frequency in rad/s
ω_e	excitation frequency in rad/s
ω_m, ω_n	m^{th}, n^{th} natural frequency in rad/s

Abbreviations

AoA	angle of attack
BC	boundary condition
CA	centroidal axis
DL	disk loading
DOF	degree-of-freedom
FE	finite element
GDE	governing differential equation
IBVP	initial boundary value problem
IC	initial condition
MOL	method of lines
NA	neutral axis
ODE	ordinary differential equation

Other notations

$(^{*})$, $(^{**})$	$\frac{\partial}{\partial \psi}(\,)$, $\frac{\partial^2}{\partial \psi^2}(\,)$
$[\,]_i$	evaluation of any term at point x_i including the derivatives, $i = 1,2, \ldots M$

List of Figures

List of Tables

Abstract

The helicopter possesses the unrivaled capacity for vertical takeoff and landing which has made the helicopter suitable for numerous tasks such as carrying passengers and equipment, providing air medical services, firefighting, and other military and civil tasks. The nature of the aerodynamic environment surrounding the helicopter gives rise to a significant amount of vibration to its whole body. Among different sources of vibrations, the main rotor blade is the major contributor. The dynamic characteristics of the hingeless rotor consisting of elastic blades are of particular interest because of the strongly coupled equations of motion. The elastic rotor blades are subjected to coupled flapping, lead-lag, and torsional (triply coupled) deflections. Once these deflections exceed the maximum allowable level, the structural integrity of the rotor blade is affected leading to the ultimate failure. The maximum deflection that a blade can undergo for a specific operating condition needs to be estimated. Therefore, in this study, the triply coupled free and forced response of the Bo 105 hingeless, composite helicopter rotor blade is investigated at hovering and forward flights. At first, a model of the composite cross-section of the rotor blade is proposed for which a semi-analytical procedure is developed to estimate the sectional properties. These properties are used in the mathematical model of the free vibration of the rotor blade having the proposed cross-section to solve for the natural frequencies and the mode shapes. The aerodynamic loadings from the strip theory are used to estimate the time-varying forced response of the rotor blade for hovering and forward flights. The large flapping and inflow angles are introduced in the mathematical model of the forward flight and the corresponding nonlinear mathematical model requires a numerical solution technique. Therefore, a generalization of the method of lines is performed to develop a robust numerical solution in terms of time-varying deflections and velocities. The effect of the unsteady aerodynamics at the forward flight is included in the mathematical model to estimate the corresponding dynamic response. Both the analytical and the numerical models are validated by finite element results and the convergence study for the free vibration is performed.

Keywords: Vibration analysis; composite blade; forward flight; numerical solution; finite element; unsteady aerodynamics

CHAPTER 1

Introduction

1.1 Vibration in the Helicopter

The helicopter is a prolific and essential means of transport of everyday life for performing numerous important tasks; especially, in the military, medical emergency, and transportation of personnel and equipment. Compared to the fixed-wing aircraft, due to the unique capacity for vertical takeoff and landing, hovering for extended periods of time, and the low-speed maneuverability, the helicopter has become essential for military and civil missions. During hovering or flying forward, the helicopter stays in the space for considerable amount of time for which the rotor system needs to be operationally safe and efficient. However, the higher rotational speed of the main rotor causes rotary imbalance and consequently, gives rise to significant vibrations in the helicopter leading to the blade failure. Moreover, the unsteady aerodynamic loads acting on the rotor blades also contribute to increase the vibration level. These vibratory loads can reduce the life of the rotor hub by damaging the heavy rotational components limiting the helicopter's community acceptance and mission effectiveness. Since the sources of vibrations are linked to the flying mechanism of the helicopter and the aerodynamic environment in which it operates, it is unlikely to fully eliminate the vibration. Instead, the magnitude of the overall vibration could be suppressed by an efficient control system. For that, the primary focus is to get an estimation of the maximum allowable level of vibration for the helicopter for a specific operating condition that it can sustain safely without making any damage. Vibrations of the helicopter rotor blades are subjected to couplings from the blade materials and the degrees-of-freedom (DOFs) which affect the vibration frequencies and the time-varying deflections. While many sources including the main and the tail rotor, engine, and gearbox contribute to the overall vibration, the dominant source of the vibration and noise is the main rotor.

1.2 How Helicopter Works—Generation of the Aerodynamic Forces and Moments

The helicopter is a complex flying machine with numerous sources of applied forces and moments coming from the rotary engine components, the interaction between the rotor blades,

and the steady and unsteady aerodynamic environments. For any flight, the helicopter rotor can be described with a state subjected to six generalized forces and moments as shown in Fig. 1.1, which vary in magnitudes with different flight conditions and rotor configurations. The forces and moments that each blade experience, are also available to other blades as they change their positions with respect to the azimuth angle. In addition to this, the very high centrifugal force generated from the rotation of the blade keeps the blade almost straight making the rotation of the blade as the rigid body motion. Therefore, the basic motions of each blade are categorized into three unique DOFs of motion which are—the flapping, the lead-lag, and the torsional motions described in Fig. 1.2.

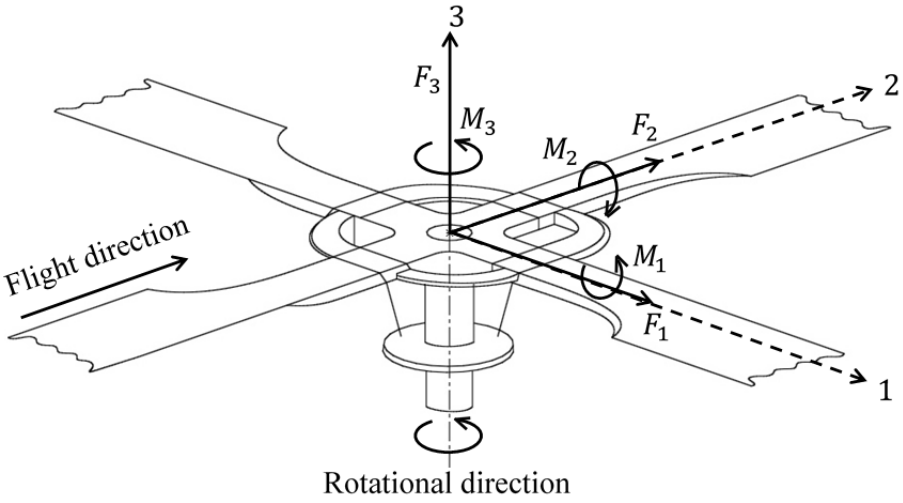

Fig. 1.1. Generalized forces and moments on the helicopter rotor

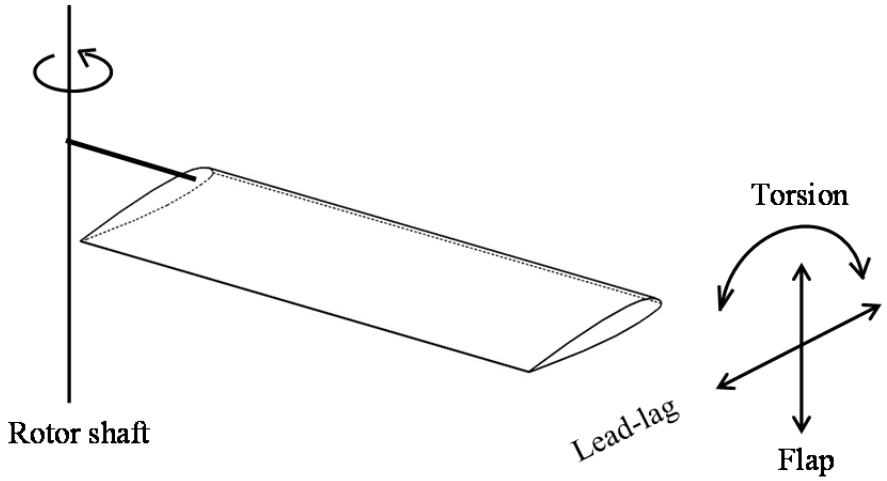

Fig. 1.2. Fundamental helicopter rotor blade motions

The three DOFs of motion are caused by three different aerodynamic loadings which are termed as the lift force creating the flapping motion, the drag force creating the lead-lag motion, and the pitching moment which creates the torsional motion. To understand the aeromechanics of the helicopter's flight comprehensively, the knowledge behind the mechanism of generation of these forces and moment are required. It is obvious that in order to fly, an object must have to generate lift, a force which tends to move the object upward. Lift is usually generated by wings having an airfoil like cross-section for both the fixed and rotary-wing aircrafts. However, unlike an airplane, a helicopter does not have to move quickly through the air to have lift. A helicopter generates lift by moving the air over its spinning rotor blades at a certain speed. Wings create lift because of a relationship between the speed of the relative air and the pressure in the air, known as the Bernoulli principle. Bernoulli principle states that when the air speed goes up, the pressure goes down. In the same way, when the air speed goes down, pressure goes up. The airfoil like cross-section is curved at the top and relatively flat at the bottom. Therefore, as the helicopter blade rotates, the airfoil shape makes the air flow over the top to move faster than that at the bottom. As a result, there is less air pressure on top of the wing compared to the bottom as shown in Fig. 1.3. The net pressure difference causes suction to move the wing in the upward direction and thus lift is generated.

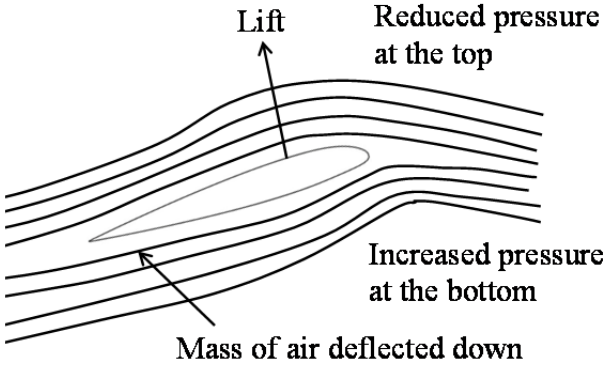

Fig. 1.3. The principle of lift generation for the helicopter

Sometimes, the term 'thrust' is used in the helicopter aeromechanics in parallel to 'lift'. However, the actual meaning of thrust differs from lift depending on a specific flight regime of the helicopter. In any flight condition with respective orientation of the helicopter and its rotor blades, there is a net 'resultant' force which always acts perpendicular to the rotor disk plane. For

the hovering flight, both the lift itself is the resultant force act perpendicular to the rotor disk plane; either of which can be termed as the thrust. However, for forward or other level flights, the rotor disk plane is tilted by a certain angle with respect to the vertical axis to generate the propelling force for the helicopter. Then, from Fig. 1.4, the resultant force acting perpendicular to the rotor disk plane is decomposed into the vertical force components, known as the lift and the horizontal component, which generates the propelling force. This horizontal force component is known as the thrust for forward or level flights. In a helicopter, the thrust can be forward, rearward, sideward, or vertical. The direction in which the helicopter will move is determined by the resultant of the lift and the thrust. The solidity ratio, σ of a specific helicopter rotor measures the potential of a rotor system to provide the thrust and lift.

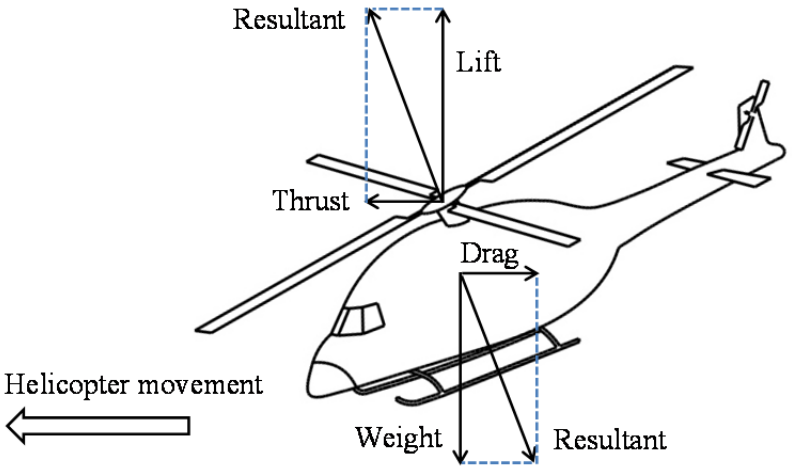

Fig. 1.4. Force balance in the helicopter for a general flight condition

The lift generated by the helicopter rotor blade depends on the following factors:

1) Speed of the airflow

2) Density of the air

3) The rotor blade planform area

4) The angle of attack (AoA)

It has to be remembered that, the lift is generated when an object changes the direction of flow of a fluid or when the fluid is forced to move by the object passing through it. To deflect the

air downwards, the rotor blade must be pitched up to create a positive lift which is controlled by the pilot. However, with the change of the pitch angle, the AoA is also changed. The AoA is defined as the angle at which the rotor blade airfoil meets the oncoming airflow defined as the relative airflow which is a combination of the downwash and the tangential airflow shown in Fig. 1.5.

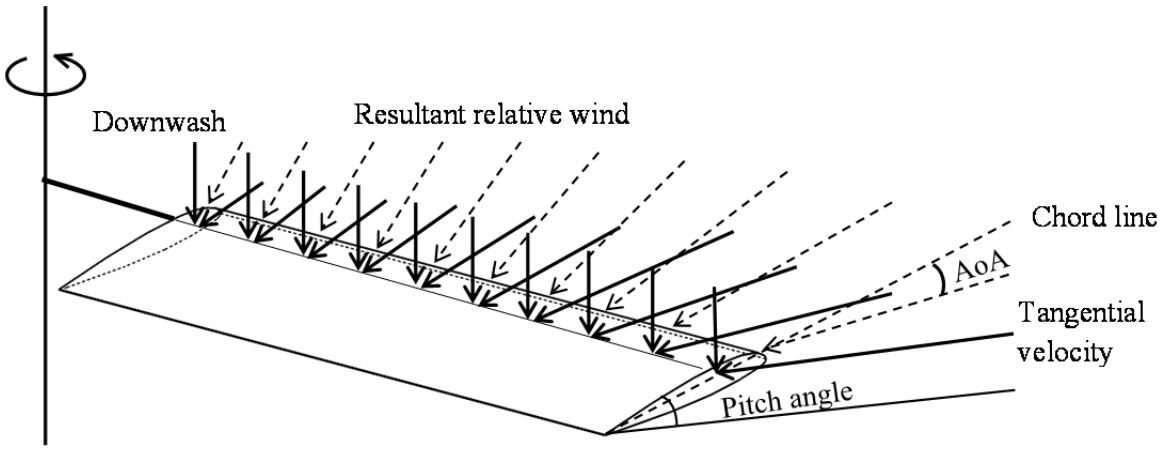

Fig. 1.5. Creation of lift, drag, and pitching moment in a typical helicopter rotor blade

As the helicopter moves through the air, a force is generated that tends to resist the movement of a helicopter through the air. During the hovering flight, this force comes only from the rotational motions of the blades through the air. But for forward flight, this force comes from the rotational motions of the blades as well as from the motion of the fuselage propagating through the air. This resistive force is the drag and the overall magnitude of the drag must be overcome by the engine power. The overall drag force is a combination of the lift induced drag and the profile drag, which always acts parallel to the relative wind. The profile drag is developed from the frictional resistance of the blades passing through the air. It does not change significantly with the airfoil's AoA, but increases moderately when airspeed increases. Lift induced drag comes from the contribution of the lift force which is not exactly vertical. In forward flight, the parasite drag is generated due to the movement of the helicopter body through the air mass and is proportional to the relative airspeed. The nonlifting components of the helicopter, such as the cabin, rotor mast, tail, and landing gear, contribute to the parasite drag which becomes the major drag in high speed forward flights.

The pitching moment for an airfoil is generated due to the aerodynamic lift force on the airfoil and the movement of the type of the airfoil through the air. The lift force is the distributed force assumed to act through the aerodynamic center. If the shear center of the airfoil cross-section does not coincide with the aerodynamic center, the lift force contributes to one part of the pitching moment. Another part of the pitching moment comes from the motion of the airfoil through the air which depends on the Reynolds number. For this case, depending on the type of the airfoil, the pitching moment coefficient is calculated from the chart for a specific airfoil shape. However, as the AoA changes for a cambered airfoil, the pitching moment coefficient changes only a little over the whole operating range of the AoA. For helicopter aeromechanics, the $1/4^{th}$ chord point is normally used as the point through which the pitching moment occurs and is considered to be the aerodynamic center. Chapters 4 and 5 explain the estimation of the lift, drag, and the pitching moment for the helicopter rotor blade in detail from the perspective of the aerodynamic strip theory.

1.3 Different Types of Helicopter Rotors

To investigate the vibration characteristics of the helicopter, the governing equations of motion for a specific flight condition need to be formulated. Solutions of the governing equations of motion are termed as the boundary value problems which require appropriate boundary conditions (BCs) to solve. Some of those BCs are determined directly from the end conditions of the helicopter rotor blades. The end condition, where the rotor blade is connected to the central hub, i.e., the root of the blade, is different for different helicopter models. The response of the rotor blade subjected to the aerodynamic forces and moments is governed by the blade root condition. The mechanical arrangement of the central rotor hub to accommodate the flapping and the lead-lag motion of the blade provides a fundamental classification of rotor types which is discussed below.

1.3.1 Fully Articulated Rotor

Generally, this kind rotor system is for the helicopters with more than two blades. In the fully articulated rotor system, the blades are attached to the hub with flapping (moving up and down about an inboard mounted hinge), lead-lag (moving back and forth in plane), and feathering (rotating about the pitch axis to change lift) hinges. Each of the blade motion is related

to the others. This flapping hinge is designed to compensate for the dissymmetry of lift and might be located at varying distances from the rotor hub. Examples are: AgustaWestland AW 109, Sikorsky S-300, etc.

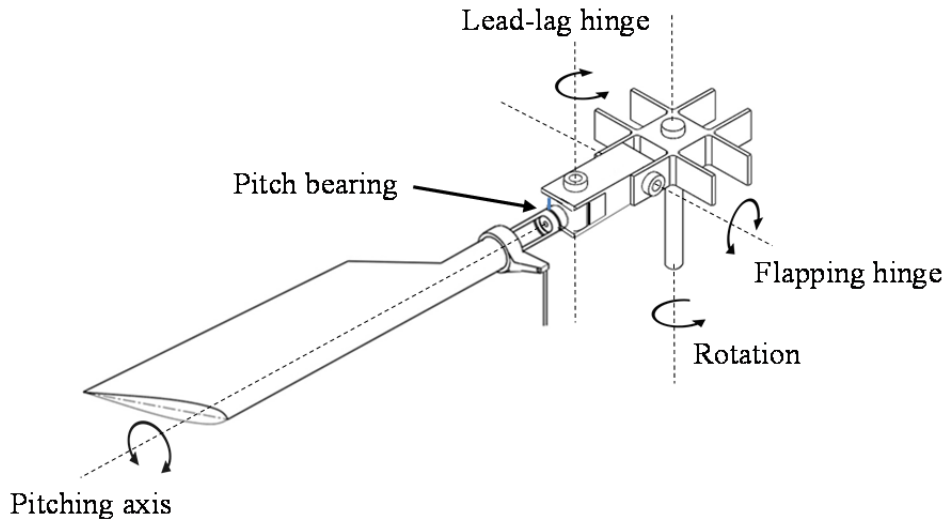

Fig. 1.6. Fully articulated rotor system

1.3.2 Semi-Rigid/Teetering/See-Saw Rotor

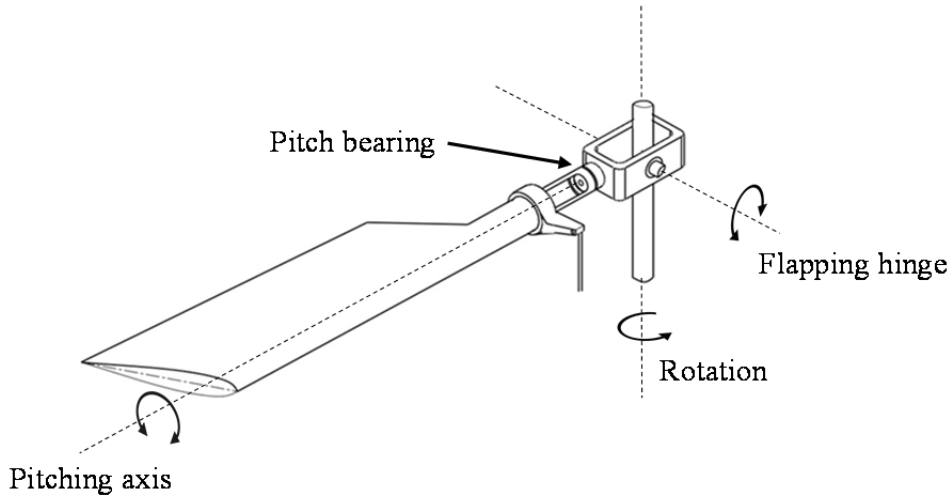

Fig. 1.7. Semi-Rigid rotor system

Semi-Rigid rotor systems are used with the helicopters with two blades. The two blades are rigidly mounted to the main rotor hub. The main rotor hub is free to tilt with respect to the main rotor shaft on what is known as a teetering hinge. This allows the blades to flap together as a single unit. As one blade flaps up, the other flaps down. The rotor has no lead-lag hinges and

therefore, the force that tends to create the lead-lag motion is absorbed by the blade flex. The semi-rigid rotor has a feathering hinge to change the pitch angles of the blades. Examples are: Robinson R22, Bell 47, etc.

1.3.3 Hingeless/Rigid Rotor

The blades are flexibly attached to the hub without flap or lag hinges, although often with a feathering bearing or hinge. Loads from flapping and lead-lag forces are accommodated through rotor blades flexing, rather than through hinges. By flexing, the blades themselves compensate for the forces. The blade is attached to the hub with cantilever root restraint, so that no deflection occurs at the root and all kinds of bending motion occur in the remaining part of the blade. Thus the hingeless rotor, also known as the rigid rotor, eliminates the danger of mast bumping inherent in the teetering rotor. Examples are: MBB Bo 105, Eurocopter EC 135, etc.

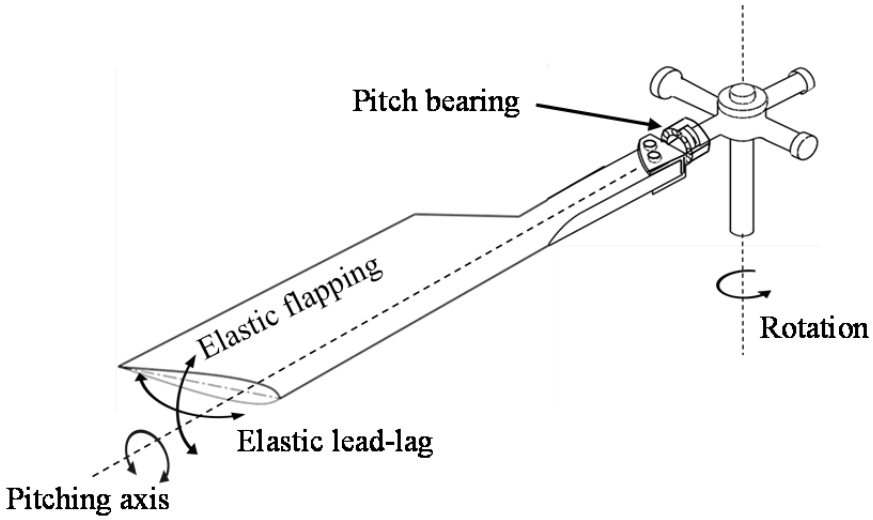

Fig. 1.8. Hingeless rotor system

1.4 Literature Survey

Vibration has been an inherent problem for the helicopter designers since Igor Sikorsky started building helicopters. The helicopter is a rotary-wing aircraft which has the capability to generate the lift and thrust by the rotational motion of the rotor blades. This rotational speed of the helicopter is kept constant by the pilot unless the loads on the rotor blades are changed. Vibratory loads transferred from the main rotor to the fuselage have been a critical concern from the earliest days of rotorcraft development (Gerstenberger et al., 1957; Loewy, 1980). Depending

on the flight regime, different phenomena become responsible for generating the vibratory loads on the blades. Previous studies that showed some investigations on the helicopter hovering performance, varied in the techniques used for analyzing the dynamics based on different assumptions. The first step was to understand the behavior of the aerodynamic environment which created the unbalanced forces acting on the helicopter (Johnson, 1994; Leishman, 2006) followed by the derivation of the fundamental equations of motion. For the hovering condition, motion of the helicopter rotor blade is considered as the rotation of a flexible cantilever beam around an axis based on which the free vibration theory is developed (Bramwell et al., 2001; Genta, 2005). The characteristics of the coupled vibration were investigated by researchers in the past (Jin and Koya, 2016; Pertsch and Sawodny, 2016) with different supports and BCs (Karimi and Ziaei-Rad, 2015). Also, vibrations of composite beams were analyzed in order to show the influence of the composite structures on the magnitudes of vibrations unlike homogeneous structures (Aksencer and Aydogdu, 2015; Ghafari and Rezaeepazhand, 2016; Qin et al., 2016; Sarker et al., 2016; Sheikh et al., 2015).

Previous studies showed that researchers continued their effort to develop the mathematical model of the vibration analysis for the rigid and flexible rotor blade simulation, based on which the groundwork for the proposed technical approach started. Besides deriving the free vibration equations of motion, rigid body simulations were also carried out. A dynamic model of rotor blades for real-time helicopter simulation was presented which was based on the rigid body simulations, rather than the fluid simulation methods (Park et al., 2012). Modeling of the helicopter rotor blade for flapping motion was done by some researchers; however, they considered only the rigid blade which, in reality, is flexible. A general equation describing the rigid helicopter blade dynamics for large flap angle and large induced inflow AoA was derived and numerical simulations were performed for steady-state conditions (Majhi and Ganguli, 2008). Gilad (2011) carried out a study of the ground influence on a hovering rotor of highly elastic blades in extreme ground proximity by using the finite element (FE) method for the deflections. Zaw et al. (2014) developed the mathematical model and carried out the stability analysis of an unmanned aerial helicopter using the minimum-complexity helicopter simulation model by MATLAB SIMULINK and considered rigid body dynamics. Numerical techniques were used for the formulation of the equations of motion of general dynamic systems with an emphasis on the equations of motion of helicopter blades (Rand and Barkai, 1995). Among the

research works related to the equations of motion of the flexible rotor blades, the most comprehensive work belongs to the analysis of the linear, coupled vibration equations developed by Houbolt and Brooks (1957). They derived the linear equations of motion of a rotating helicopter blade for forced vibrations including the coupling terms. Following this, Hodges and Ormiston (1976) studied the stability of elastic bending and torsion of a uniform cantilever beam in hover with various structural couplings.

Technical reports were documented after the wind-tunnel tests for the reduced and full scale helicopter and provided useful information about the pioneering research and specific design database (Bousman, 2003; Brooks et al., 1988; Peterson, 1995; Shinoda, 2004). Helicopter blades reported to be tested experimentally are made up of different types of materials. However, instead of metallic blades, composite blades are widely used in modern helicopters due to their high strength-to-weight ratio (Hopkins and Ormiston, 2003), although, research is still being continued on the challenges of fabricating nanomaterial reinforced prepregs for enhancing the mechanical properties of the composite materials (Islam and Kelkar, 2017a, 2017b). Garinis et al. (2012) carried out the modal analysis of the fully composite helicopter blade with honeycomb core to determine the structural mode shapes and natural frequencies. Friedmann et al. (2009) developed a moderate deflection composite helicopter rotor blade model with an improved cross-sectional analysis based on the variational asymptotic approach. The aeroelastic optimization analyses of the composite helicopter rotor blades were done where the composite material ply structure and blade tip swept angle were the primary design variables (Ganguli and Chopra, 1996; Guo and Xiang, 2004; Murugan et al., 2008; Yuan and Friedmann, 1998). Among various numerical tools, the FE techniques were known as powerful tools to model the rotor blade or a rotating beam for the vibration analysis. Hodges et al. (1991) presented the methodologies for predicting the natural frequencies and mode shapes of composite beams with arbitrary cross-sections by FE techniques. Different types of FE methods were examined to verify their efficiencies by finding the frequencies of vibrations (Banerjee and Williams, 1994; Hashemi and Rechard, 2000; Jin et al., 2015; Kaya and Ozgumus, 2007). However, the influence of several factors such as rotor geometry, blade pitching kinematics, and ground effect on the aerodynamic behavior make the FE modeling complex and needs some basic assumptions to simplify the complex aerodynamic behavior of the rotor blades (Benedict et al., 2013; Ganesh and Komerath, 2004).

To improve the performance of the helicopter, the rotor power of the helicopter needs to be investigated. An analytical model was developed to predict the rotor power by investigating the dynamic blade twist which was validated by the flight data of the UH-60A helicopter (Han et al., 2016a). A combination of the variable blade twist and variable rotor power was used to reduce the rotor power for improving the helicopter performance based on the empirical and the CFD models. It was found that, the rotor power can be reduced more by varying the rotor speed than by variable blade twist in addition to the reduction of the rotor speed (Han et al., 2016b). It was shown that, in high speed forward flight, the power reduction by the prescribed dynamic blade twist is more significant than in hover and low-speed forward flight. A method to obtain the optimal helicopter rotor blade planform and airfoil shape was proposed to investigate the aerodynamic performance of the helicopter in forward flight by the shape function transformation (Vu and Lee, 2015). The design variables used represented the airfoil shape with the aerodynamic constraints composed of the lift, drag, and moment coefficients for critical flow condition occurring on rotor blades. An approach to improve the helicopter performance by reducing the helicopter drag was investigated by Gibertini et al. (2015). They investigated the performance of the vortex generators by CFD analysis and wind-tunnel tests on a heavy-class helicopter fuselage model. Numerical investigation on the effect of periodic blade pitching on rotor aerodynamics was carried out at a Reynolds number typical of micro-air vehicles (Jardin et al., 2016). From the study, it was found that, proper tuning of pitching variables could lead to an increase in the rotational efficiency and thrust.

Compared to linear vibration models, nonlinear vibrations are studied in a much narrower margin. This is due to the effectiveness of the approximate solution obtained from the linear models. However, the linear models are restricted up to certain conditions beyond which noninclusion of the geometric and material nonlinearity underpredicts the result. Alonso and Ribeiro (2008) analyzed the free, nonlinear longitudinal, torsional, and bending vibrations of beams with circular cross-sections. Damping was also considered to study the nonlinear forced vibrations with small and large vibration amplitudes using higher order theories (Youzera et al., 2012). Bekhoucha et al. (2016) studied the nonlinear free bending vibrations of a centrifugally stiffened beam with uniform cross-section with a constant angular velocity. They considered the coupling and warping terms in the nonlinear equations of motion of isotropic beams by combining the Galerkin method with the harmonic balance method. Carrera et al. (2016) studied

the free vibration characteristics and tailoring of laminated composite box structures by the refined beam theory. The developed methodology was utilized to analyze the single- and multi-bay composite laminated box beams for aerospace applications.

When the aerodynamic loading is included in the structural dynamics, then the resulting dynamic phenomena is known as aeroelasticity. Researchers worked to predict the behavior of the airfoil subjected to both the steady and unsteady aerodynamic loading. However, unlike the steady aerodynamic characteristics, the unsteady behavior is still challenging to model in terms of elastic deformations. Wang and Zhao (2016) simulated the unsteady aerodynamic characteristics of the SC 1095 airfoil with variational freestream velocity. Lind and Jones (2016) investigated the behaviors of the four rotor blade airfoils subjected to unsteady airloads at high AoA in the reverse flow. The unsteady airloads were calculated by integrating time-resolved pressure measurements along the midspan of the airfoil and were found to be periodic and greater at higher AoAs. The unsteady aerodynamic load behavior can be visualized either from the analytical model or from experimental results. A reduced order modeling approach was presented by Fossati (2015) for the evaluation of steady aerodynamic loads by using proper orthogonal decomposition-based methodology. Carrión et al. (2015) showed that, prediction of the wake instability and the physical mechanism of its breakdown downstream of a rotating wing could be important for a specific fluid-structure interacting domain. The fluid-structure interaction and efficient numerical techniques were also implemented by researchers to characterize the unsteady aerodynamic behavior (Yang et al., 2015; Zhang et al., 2015).

In contrast to the fixed-wing aircraft, the flow field around the helicopter main rotor blade is highly influenced by the wake effect which contributes to the generation of the vibration. The wake behind the rotor disk determines the induced inflow distribution over the disk and plays a key role to affect the corresponding vibratory loads and the blade response (Murugan and Ganguli, 2008). The linear inflow model is useful for performance predictions but greatly unpredictable to estimate the vibratory loads when the inflow distribution becomes highly nonuniform over the rotor disk. Therefore, different inflow models including the dynamic inflow model and the finite state inflow model were studied by researchers to provide the insight on the characteristics of the inflow distribution over the airfoil (Peters and He, 1989; Peters et al., 2007; Pitt and Peters, 1981). Zhao (2005) developed the dynamic inflow wake distortion model to

account for the rotor transient wake distortion effect. An efficient actuating blade model was presented for the simulation of unsteady rotating system wakes with application to wind turbine blades in CFD method (Lynch et al., 2014). Farrugia et al. (2016) presented the aerodynamic analysis of a full-scale floating offshore wind turbine rotor by using a free-wake code. They concluded that at high tip speed ratios, the turbine operation might result in significant aerodynamic load fluctuations and the difference between the mean and the steady power coefficients depended on the platform surge frequency and amplitude. Sometimes, the nature of the inflow helps to understand the flow visualization. Li et al. (2016a, 2016b) studied the effect of the turbulent inflow to investigate the aerodynamic characteristics and performance of the horizontal axis wind turbine for turbulent inflows. Taha et al. (2014) presented a state-space formulation for the flapping aerodynamics by extending the Duhamel's principle for linear unsteady flows in order to capture the leading edge vortex contribution. They derived a reduced order model from the full model suitable for flight dynamics and control which was validated by numerical simulation of the Navier-Stokes model on hovering insects.

In most of the previous cases, simulations for rotor blades with different aerodynamic conditions were done considering the blade as a rigid one or FE simulations were done for free vibrations of a blade subjected to uncoupled bending. However, still, the available research studies are not sufficient to quantitatively analyze the bending-bending-torsion coupled (triply coupled) free and forced vibration characteristics for a rotating, flexible composite helicopter rotor blade and there is a great scope to proceed further from this stage.

1.5 Scope of the Study

1.5.1 Motivation

From the overview of the literature survey, it is of no wonder that vibration in the helicopter is inherent due to its flying mechanism. There is no way to fully eliminate the vibration but has some options to control or suppress it. The different sources of vibrations mainly include the vibration that propagates from the rotary engine components to the fuselage, the vibration induced from the main rotor blades under steady airloads, and the same due to the unsteady airloads. Engine transmitted vibration is considered intrinsic to the helicopter. The main rotor blade induced vibration under steady airloads is the major vibration source often generating

from the moderate deflection of the rotor blades. This, when assisted by the unsteady airloads, causes the overall vibration to increase significantly, thereby, affecting the helicopter performance harshly. To minimize it, the magnitude and the characteristics of the blade response need to be properly estimated. Knowing this fact, the motivation behind this study was triggered so that a realistic helicopter rotor blade model could be studied to investigate the dynamic characteristics of the forced response subjected to steady and unsteady aerodynamic environments.

The potential and uniqueness of the analysis upon inclusion of the relevant, existing but unexplored features are the primary incentives behind this study. The helicopter rotor blade can be modeled as a rotating beam which was extensively studied by the researchers in the past. In most of the cases, those studies were focused on the linear forced response of a beam with material homogeneity and single DOF or with conventional forcing functions. Hence, there exists a great scope to extend the analysis further having applications in the fields of other fluid driven machineries, e.g., steam turbines, ship propeller blades, wind turbines, etc. Part of the motivation for conducting this study originates from these applications to correlate the analogy of the rotating beam to the helicopter rotor blade so that a generalized forced response theory can be formulated. Moreover, in majority of the cases, realistic beam vibration problems include nonlinear governing equations with more than one strongly coupled DOF for which the numerical solution technique is a suitable approach. For this reason, a numerical method is adopted for solving a general, coupled forced beam vibration problem having multiple DOFs. The accomplishment of the overall task comes from the combination of:

a) Study of the coupled, free vibration characteristics of a helicopter rotor blade with a proposed cross-sectional profile similar to a specific helicopter rotor blade model

b) Study of the forced response of that specific helicopter rotor blade model subjected to steady and unsteady airloads

For part a), once the natural frequencies are estimated for the coupled, free vibration of the helicopter rotor blade having the proposed cross-section, they can be used further to conduct the modal analysis for predicting the corresponding mode shapes. In part b), to estimate the forced response, the time-varying airloads on the helicopter rotor blade need to be accurately

predicted to incorporate into the corresponding mathematical models for hovering and forward flights. The combination of part a) and part b) summarizes the comprehensive aeroelastic analysis which is the ultimate goal of this study.

1.5.2 Objectives

In order to conduct the aeroelastic analysis composed of part a) and part b), the first thing is to understand the basic difference between the ordinary rotating beam and the helicopter rotor blade. In reality, the helicopter rotor blades are subjected to flapping, lead-lag, and torsional vibrations under complex aerodynamic forcing functions accompanied by different types of couplings. One type of coupling includes the coupling existing between different types of DOFs because of the different elastic and inertial axes of the airfoil, i.e., the rotor blade cross-section. Besides this, the blades are made of composite materials with different fiber orientations which create additional couplings. From the literature survey, a few studies are carried out so far for the nonlinear forced response analysis of a flexible helicopter rotor blade considering large flapping and inflow angles including the built-in blade twist, specifically, for the forward flight. For this analysis, the Bo 105 helicopter is considered as the base model because of the flexible nature of the rotor blades and the simplicity of the hingeless rotor to be used as a cantilevered beam end condition in the mathematical model. The outcome of this analysis can be fruitful for the design purpose of the rotor blade and for the justification of the promising potential of the developed generalized numerical solution. Keeping that in mind, the objectives of this analysis are sequentially broken down and are mentioned below:

a) Study of the coupled, free vibration characteristics of a helicopter rotor blade with a proposed cross-sectional profile similar to a specific helicopter rotor blade model

1. To carry out the coupled, free vibrational analysis of a helicopter rotor blade having a proposed cross-sectional profile similar to the Bo 105 helicopter rotor blade.

2. To derive a semi-analytical method for estimating the sectional properties of the proposed cross-section applicable to other similar composite beam/blade sections for design purpose.

3. To utilize the analogy of the general governing equations of motion of the triply coupled free vibration of a thin and slender, axially loaded rotating beam with built-in twist for the free vibration analysis of the helicopter rotor blade having the proposed cross-section.

4. To derive an analytical solution of the coupled governing equations of motion in Task 3 for estimating the natural frequencies of free vibration of the rotor blade and to develop the corresponding FE model to compare the analytical frequencies with that obtained from the FE model.

b) Study of the forced response of that specific helicopter rotor blade model subjected to steady and unsteady airloads

5. To develop the mathematical model for estimating the steady-state dynamic response of the Bo 105 helicopter rotor blade at the hovering flight subjected to forced vibration induced from the aerodynamic loadings in terms of the lift, the drag, and the pitching moment.

6. To develop the comprehensive mathematical model for the dynamic response of the Bo 105 helicopter rotor blade during the forward flight subjected to both steady-state and unsteady aerodynamic loadings by incorporating the large flapping and inflow angles in the mathematical model.

7. To develop a numerical algorithm for the solution of the governing equations of motion of the coupled, forced beam vibration with multiple DOFs by the generalization of the method of lines (MOL). The algorithm is generalized in such a way so that it applies to any linear/nonlinear, coupled/uncoupled initial boundary value problem (IBVP) having single DOF/multiple DOFs with classical/moving BCs.

8. To validate the numerical method by comparing the forced response of a rotating beam obtained by the MOL to that of the same beam estimated by the corresponding FE model.

9. To calculate the corresponding dynamic responses of the Bo 105 helicopter rotor blade at hovering and forward flights subjected to respective aerodynamic loadings specified in Tasks 5 and 6 by utilizing the numerical technique developed in Task 7.

CHAPTER 2

Modeling of the Composite Helicopter Rotor Blade

2.1 History of Composites

The history of helicopter blades dates back before 1960, when the primary constituent materials of the rotor blades were laminated wood and fabric. Wood is an excellent material for the rotor blades, however, one disadvantage of wood is that it has a tendency to absorb moisture and therefore, the mass of the blades are altered. To overcome this problem, metallic blades appeared having greater strength compared to wood such as steel or aluminum. However, metallic blades possessed poor fatigue resistance and low strength-to-density ratio. Also, when a metal blade was damaged or cracked in a critical area, it experienced a catastrophic failure with little warning. In quest of a strong, lightweight, and reliable helicopter rotor blade material, it was found that no specific material was as tough as the metal and as light as wood. The only solution is to manufacture the blades composed of composite materials. The most attractive feature of the composite materials is their highest strength-to-weight ratio. Following this, perhaps, the most important use of the composite materials in the modern history of the rotary-wing aircrafts is their presence as the major constituent materials. Also, composite materials are much easier to process and manufacture, can be joined with adhesives negating the need for riveting and simplifying the assembly, and can be manufactured using much cheaper tooling than using metals.

Among various types of composites used as the constituent materials of the helicopter rotor blade, the carbon-epoxy, the fiberglass-epoxy, and the boron-epoxy composites are the most common. For all of them, the epoxy matrix (Ahmed et al., 2018) is reinforced with the fiber, where the volume fraction of the fiber and the epoxy can be varied. Moreover, different orientations of fibers in the composite blade give different directional stiffness properties which can be used to control the aeroelastic deformation, known as the aeroelastic tailoring. In modern helicopters, there is no alternative of using composite materials with suitable fiber orientations to affect the aerodynamic and structural performance in a beneficial way. In this chapter, a model of the cross-section for the Bo 105 helicopter rotor blade is proposed made of composite and other types of materials which represents the cross-section of a sandwich beam. The primary

objective is to develop an analytical method for estimating the cross-sectional properties that can be applied to other similar sandwich beam sections. The estimated properties of the proposed section are used later for the analytical solution of the free vibration in Chapter 3.

2.2 Geometric Construction of the Proposed Composite, Sandwich Beam Cross-Section

The proposed cross-section of the rotor blade for the free vibration analysis is similar to that of the Messerschmitt-Bölkow-Blohm Bo 105 helicopter rotor blade, which is a light, twin-engine, multi-purpose helicopter developed by Bölkow of Ottobrunn, Germany. Figure 2.1 shows the proposed asymmetric, solid, and composite cross-section made of a thin, outer shell of orthotropic fiberglass-epoxy (Salkind and Hollister, 1973) composite with the fiber volume fraction as 0.6 and a thick, inner, composite core made of an isotropic polymethacrylimide (PMI) foam called Rohacell (Product Information–Rohacell) and an isotropic Honeycomb structure (HexWeb Honeycomb Attributes and Properties). The profile of the cross-section resembles the NACA 23012 airfoil (Goulos et al., 2015). The geometric construction in Fig. 2.1 gives the basic components of a typical rotor blade cross-section where the composite shell acts as a balanced laminate composed of four plies with a high strength-to-weight ratio compared to the inner core of the cross-section which altogether, is considered as a sandwich beam cross-section.

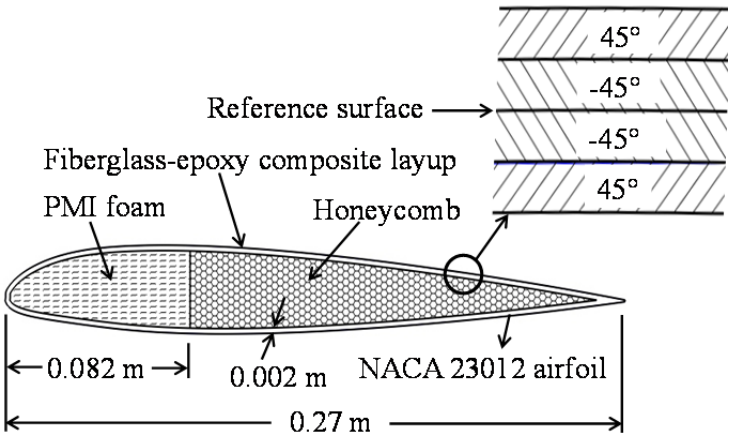

Fig. 2.1. Proposed cross-section of the Bo 105 helicopter rotor blade

The specific features of the Bo 105 helicopter rotor blade are as follows:

1. The Bo 105 main helicopter rotor blade is uniform throughout its length from the blade root to the blade tip. However, there is a twist distribution from the blade root to the tip

which is not included in the free vibration analysis but used in the forced response analysis.

2. The rotor blade features a hingeless rotor system (Panda and Chopra, 1986), which can be treated as a cantilever blade, i.e., the blade with a fixed/bolted end at the root.

All the necessary parameters and properties regarding the Bo 105 helicopter rotor blade for the free vibration and for the dynamic response analyses are given in Table 8.3.

2.3 Cross-Sectional Analysis

The accurate estimation of the properties of the cross-section described in Fig. 2.1 requires considerable effort and time because of the composite nature of the section and the asymmetry involved with respect to the chord. However, some reasonable assumptions make the cross-sectional analysis approximate but accurate enough by using the fundamental principles of composite mechanics and classical lamination plate theory. The helicopter rotor blade can be considered as a long, thin plate so that the plane stress assumptions hold good. However, the curvature effect of the blade section contour must be taken into account. The following sub-sections explain the procedures for estimating the properties of the composite beam/blade cross-section shown in Fig. 2.1.

2.3.1 Calculation of the Profile of the Reference Surface

The key part of the cross-sectional analysis is to find the profile of the reference surface in Fig. 2.1, which is a closed curve parallel to the outermost or the innermost profile of the cross-section and is located exactly in the middle of the outermost and the innermost profiles. In that sense, it can be treated as the offset curve either from the outermost or the innermost shell profile separated by a distance of $h_{shell}/2$, where h_{shell} is the total thickness of the composite shell. To determine the profile of the reference surface, at first, the profile of the outermost or the innermost shell surface of the section needs to be known. Therefore, the outermost shell profile in Fig. 2.1 is generated from the NACA 23012 data. Both the generated outermost upper profile and outermost lower profile of the rotor blade section are fitted into MATLAB (MathWorks Corporation, 2015) by the 10^{th} degree polynomial curves to get the corresponding profile equations.

A convenient way to generate a curve parallel to another curve is to formulate the parametric equations of the original curve. However, this method is not very feasible to implement for determining the profile of the reference surface of Fig. 2.1. This is because, parametric equations, in general, are applied to well defined simple geometries and have limitations to be used with higher order polynomials. Therefore, data points on the reference surface are generated analytically from the differential calculus slope theory for sufficient number of points. The whole procedure of generating the coordinates of the points on the reference surface from the outermost surface of the composite shell is demonstrated in Fig. 2.2.

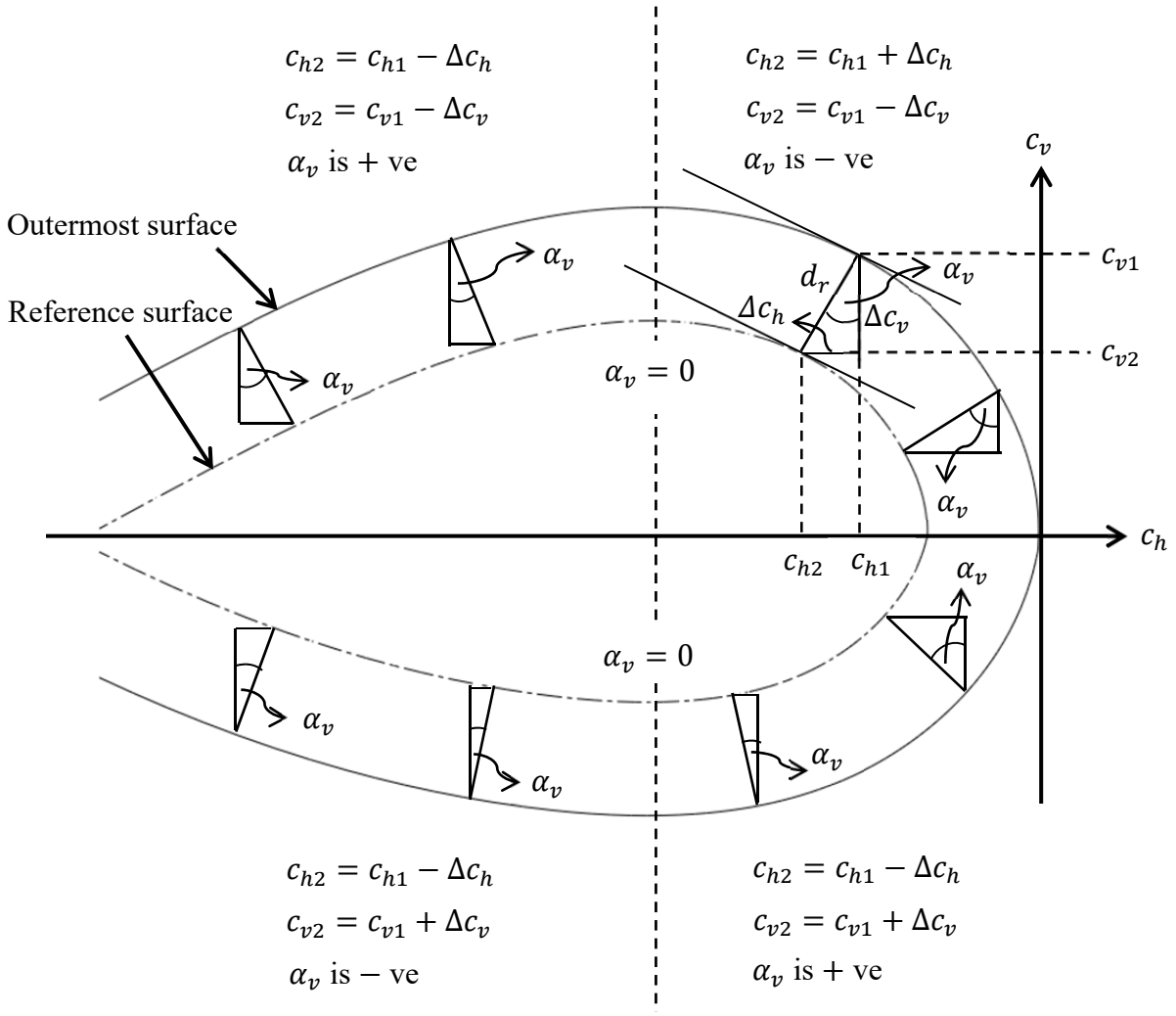

c_{h1}, c_{v1}: Known coordinates of the points on the outermost surface

c_{h2}, c_{v2}: Unknown coordinates of the points on the reference surface

Fig. 2.2. Generation of the reference surface from the outermost surface of the composite shell

Figure 2.2 utilizes the fundamental rule for generating two parallel curves which states that the radial distance between them must be the same. This radial distance between the outermost surface and the reference surface is denoted by d_r in Fig. 2.2, which also represents the length of the common normal perpendicular to the respective tangents at two different points on the two curves. To apply the slope theory, the whole airfoil cross-sectional area is segmented into four regions, depending on the directional change of the tangents. Starting from the leading edge of the airfoil, all the four segments show drastic changes of the slope angle, α_v depending on which c_{h2} and c_{v2} are calculated from the respective formula mentioned in each segment of Fig. 2.2.

Since c_{h1} and c_{v1} are already known from the NACA 23012 airfoil data, the only remaining formula to calculate Δc_h, Δc_v, and d_n are:

$$\Delta c_h = d_r sin\alpha_v \tag{2.1}$$

$$\Delta c_v = d_r cos\alpha_v \tag{2.2}$$

$$d_r = \frac{h_{shell}}{2} \tag{2.3}$$

where Δc_h is the distance between c_{h1} and c_{h2} along the c_h axis and Δc_v is the distance between c_{v1} and c_{v2} along the c_v axis. Once the coordinates of sufficient number of points on the reference surface are known, the curves (upper and lower reference curves) are approximately fitted in MATLAB (MathWorks Corporation, 2015) by 10^{th} degree polynomial curves. These polynomial curves give the profile equations of the upper and the lower reference surfaces which are used in the next section to obtain the properties of the proposed composite cross-section of the rotor blade.

2.3.2 Estimation of the Composite Section Properties

The fitted equations of the upper and the lower reference surfaces of the composite shell is introduced to the thin walled composite beam theory in order to find the properties of the proposed composite cross-section of Fig. 2.1. The major cross-sectional properties required for the composite beam or the helicopter rotor blade vibration analysis are: the extensional stiffness, the bending stiffness (flapping and lead-lag stiffness), and the torsional stiffness. Vasiliev and

Morozov (2013) derived an analytical procedure to find the bending stiffness of the composite shell once the extensional stiffness per unit width of the composite shell, B_{shell} is known. However, the calculation of B_{shell}, in turn, requires the estimation of the equivalent extensional modulus of elasticity of the composite shell, E_{shell}. Interestingly, the basic principle considered here is that E_{shell} is the same for any arbitrarily curved thin composite shell or plate which has the same number of layers, is composed of the same composite material, and has the same length, described in Fig. 2.3. Using this principle, E_{shell} is estimated based on the classical lamination theory (Yu et al., 2011) from which B_{shell} is calculated. Following the same procedure, equivalent shear modulus of the composite shell, G_{shell} is also calculated (Yu et al., 2011).

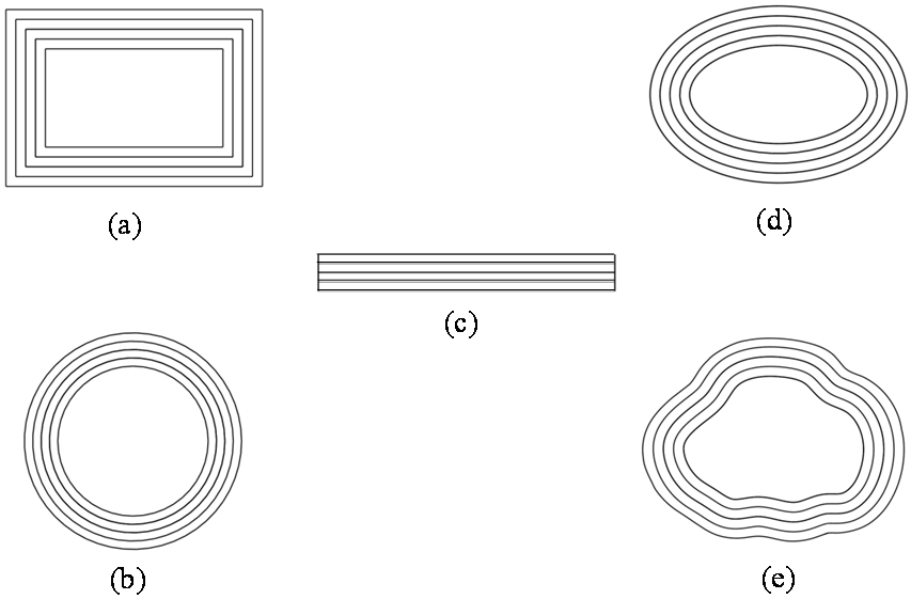

Fig. 2.3. Various types of cross-sections of thin composite structures (a) rectangular (b) elliptic (c) laminated (d) circular (e) arbitrary

The theory discussed above is applied to find the natural frequencies of free vibration of a thin-walled beam having a circular, composite cross-section consisting of four layers with ply orientations 45°, −45°, −45°, and 45° from the inner side to the outer side of the circular cross-section (Hodges et al., 1991). Excellent agreement is found between the natural frequencies obtained from this theory and that given by Hodges et al. (1991) which substantiates a good validation of the theory.

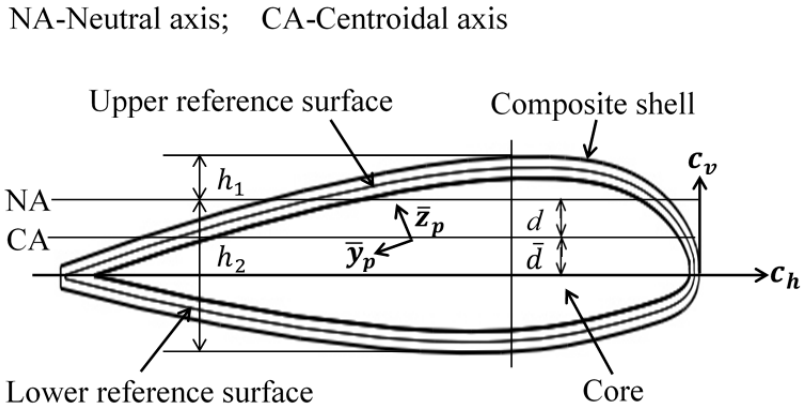

Fig. 2.4. Locations of the CA and NA of the cross-section

Figure 2.4 shows the schematic of the cross-section given in Fig. 2.1 with the presence of the centroidal axis (CA) and the neutral axis (NA). From Fig. 2.4, the CA and the principal centroidal axis $\bar{y}_p$ are not exactly aligned. However, the separation angle is found approximately 1° from SolidWorks (Dassault Systèmes, 2015), which is small enough to significantly affect the sectional properties of the shell and the core. The bending stiffness of the whole cross-section is to be calculated with respect to the NA of the section which is not located at the geometric centroid of the cross-section. This is because of the composite nature of the cross-section and therefore, the NA is shifted by a distance d from the centroid. Due to the small separation angle between the CA and the NA, the NA can be assumed horizontal and parallel to the CA. The geometric parameters of the cross-section $\bar{d}_{shell}$, $\bar{d}_{core}$, $A_{c_{shell}}$, $A_{c_{core}}$, $\bar{I}_{y_{p_{shell}}}$, $\bar{I}_{y_{p_{core}}}$, γ_{shell}, γ_{core}, and e are determined by using SolidWorks (Dassault Systèmes, 2015), where $\bar{d}$, A_c, $\bar{I}_{y_p}$, γ, and e are the distance of the CA from the c_h axis, cross-sectional area, area moment of inertia about the principal centroidal $\bar{y}_p$ axis, torsional constant of the cross-section, and distance between the centroid and the shear center, respectively. The subscripts $shell$ and $core$ stand for the composite shell and the composite core of the whole cross-section, respectively.

2.3.3 Extensional Stiffness Per Unit Width

From lamination theory (Yu et al., 2011), E_{shell} can be expressed as:

$$E_{shell} = \frac{A_{11}A_{22} - A_{12}^2}{h_{shell}A_{22}} \tag{2.4}$$

where A_{11}, A_{12}, and A_{22} are the elements of the extensional stiffness matrix of a composite laminate. Then B_{shell} is evaluated as,

$$B_{shell} = \frac{E_{shell} A_{c_{shell}}}{s_{uref} + s_{lref}} \tag{2.5}$$

where s_{uref} and s_{lref} are the arc lengths of the upper and the lower reference curves, respectively, shown in Fig. 2.2.

2.3.4 Bending Stiffness

Using the value of B_{shell} and including the curvature effect of the cross-sectional profile, bending stiffness of the composite shell is estimated as (Vasiliev and Morozov, 2013):

$$E_{shell} \bar{I}_{y_{p_{shell}}} = B_{shell} \left[\int_{c_h=l_1}^{c_h=l_2} c_{v_{uref}}^2 ds_{uref} + \int_{c_h=l_1}^{c_h=l_2} c_{v_{lref}}^2 ds_{lref} \right] \tag{2.6}$$

with $c_{v_{uref}}$ and $c_{v_{lref}}$ are the ordinates of the points on the upper and the lower reference curves obtained from MATLAB (MathWorks Corporation, 2015) curve fitting and l_1 and l_2 are the lower limit and the upper limit of integration, respectively, for the reference curves.

A reasonable expression of the equivalent extensional elastic modulus of the composite core, E_{core} can be provided by the following equation when the constituent materials have relatively close values of the elastic modulus, E for the isotropic materials:

$$E_{core} = \frac{E_r A_{c_r} + E_h A_{c_h}}{A_{c_r} + A_{c_h}} = \frac{E_r A_{c_r} + E_h A_{c_h}}{A_{c_{core}}} \tag{2.7}$$

where $A_{c_{core}} = A_{c_r} + A_{c_h}$ with the subscripts r and h standing for the Rohacell foam and the Honeycomb structure (HexWeb Honeycomb Attributes and Properties; Product Information–Rohacell), respectively, which are used for further notations from now onwards.

Using the linear strain assumption, location of the NA of the section can be found from the following equations:

$$E_{shell} d_{shell} A_{c_{shell}} + E_{core} d_{core} A_{c_{core}} = 0 \tag{2.8}$$

$$\Rightarrow E_{shell}\left(c_{v_{upper}} - h_1 - \bar{d}_{shell}\right)A_{c_{shell}} + E_{core}\left(c_{v_{upper}} - h_1 - \bar{d}_{core}\right)A_{c_{core}} = 0 \qquad (2.9)$$

$$h_1 + h_2 = h_{airfoil} \qquad (2.10)$$

where $c_{v_{upper}}$ is the ordinate of the point on the outermost upper surface measured along the c_v axis from the centroid of the whole section while h_1 and h_2 give the distances of the topmost and the bottommost points from the NA of the combined section, respectively, as shown in Fig. 2.4. The term $h_{airfoil}$ indicates the maximum thickness of the NACA 23012 airfoil which is 12% of the total chord length of the airfoil. Ultimately, the flapping stiffness is calculated from the following equations by using the inertia properties for both the shell and the core:

$$I_{NA_{shell}} = \bar{I}_{y_{p_{shell}}} + A_{shell}d_{shell}^2 \qquad (2.11)$$

$$I_{NA_{core}} = \bar{I}_{y_{p_{core}}} + A_{core}d_{core}^2 \qquad (2.12)$$

$$D_{bNA} = E_{shell}I_{NA_{shell}} + E_{core}I_{NA_{core}} \qquad (2.13)$$

where D_{bNA} indicates the bending stiffness with respect to the NA of the whole cross-section and I_{NA} represents the area moment of inertia of either the composite shell or the core about the respective NA. Due to the small angle assumption, the axis perpendicular to the NA of the whole composite cross-section is considered to be almost vertical passing through the centroid and can be defined approximately with respect to the $\bar{z}_p$ axis. Therefore, the corresponding bending stiffness can be written as:

$$D_{b\bar{z}_p} \cong E_{shell}\bar{I}_{z_{p_{shell}}} + E_{core}\bar{I}_{z_{p_{core}}} \qquad (2.14)$$

where $D_{b\bar{z}_p}$ and $\bar{I}_{z_p}$ are the bending stiffness with respect to the centroidal $\bar{z}_p$ axis of the whole cross-section and the area moment of inertia of either the composite shell or the core with respect to the corresponding $\bar{z}_p$ axis, respectively. The cross-section of the rotor blade in Fig. 2.1 or in Fig. 2.4 is asymmetric with respect to the CA. If d and $\bar{d}$ in Fig. 2.4 are very small for an asymmetric cross-section, then the NA and the CA become very close and consequently, c_h or the chord axis can be considered as the axis of symmetry. At the same time, a small separation

angle between the CA and the $\bar{y}_p$ axis in Fig. 2.4 makes the cross-section to be considered as approximately symmetric with respect to the $\bar{y}_p$ axis, i.e., the c_h axis of Fig. 2.4.

In this study, y and z axes are termed as the global orthogonal axes passing through the shear center of the cross-section, described in Chapter 3. If the section is approximately symmetric with respect to the $\bar{y}_p$ axis and maintains a small angle with the global y axis, then from the above discussion, the out-of-plane bending (flapping) stiffness with respect to the global y axis through the shear center can be approximated as:

$$D_{by} \cong D_{b\bar{y}_p} = D_{bNA} \tag{2.15}$$

Similarly, the in-plane bending stiffness with respect to the global z axis through the shear center for small value of e is:

$$D_{bz} \cong D_{b\bar{z}_p} \tag{2.16}$$

2.3.5 Torsional Stiffness

The individual shear modulus G_{shell} and G_{core} for the shell and the core, respectively, can be approximated as (Yu et al., 2011),

$$G_{shell} = \frac{A_{66}}{h_{shell}} \tag{2.17}$$

$$G_{core} = \frac{E_{core}}{2(1+\nu)} \tag{2.18}$$

where A_{66} is the element of the extensional stiffness matrix of a composite laminate and ν is the Poisson's ratio of an isotropic material. Eq. (2.18) is an approximation since both the Rohacell and the Honeycomb structures (HexWeb Honeycomb Attributes and Properties; Product Information–Rohacell) are considered isotropic and use the same ν. If the shear center and the centroid of the cross-section are relatively close to each other, then the total torsional stiffness, D_t is written as,

$$D_t = G_{shell}\gamma_{comp} + G_{core}\gamma_{core} \tag{2.19}$$

2.3.6 Mass Per Unit Length

The mass per unit length, m of the whole beam having the proposed composite cross-section is the sum of the masses per unit length, m_i of the individual constituent beams and is expressed as,

$$m = \sum_{i=1}^{3} m_i \tag{2.20}$$

$$\Rightarrow m = \rho_{shell} A_{c_{shell}} + \rho_r A_{c_r} + \rho_h A_{c_h} \tag{2.21}$$

where ρ is the material density with the appropriate meaning of the already defined subscripts.

CHAPTER 3

Triply Coupled Vibration Analysis

3.1 Overview of Coupled Vibrations

In Chapter 1, it is already discussed that there exists coupling between the three DOFs of motion for the rotating helicopter blade. This coupling can be treated as one coming from two different sources—the dynamic coupling and the geometric coupling. The dynamic coupling is caused by the angular velocity of the rotor blades while the geometric coupling is caused by the pretwist angle and/or distance between the mass and the shear center. The dynamic coupling solely depends on the rotational speed of the blades, which is constant for a steady flight condition and is considered as an integrated coupling for a helicopter. However, the geometric coupling indicates that one DOF resulting specifically from, either pure bending or pure torsion is affected by another and thus is not independent to each other. This happens when the mass center and the shear center of the cross-section of the rotor blade is different. The shear center is defined as the point on the cross-section of the blade, through which, if a transverse force is applied, it results in pure bending with no elastic torsional rotation about the center. This point is also the center of twist in response to a pure applied twisting moment. The locus of the shear centers at each segment of the cross-section is known as the elastic axis. When the cross-section of the rotor blade has two axes of symmetry, the mass center and the shear center coincide and the bending and torsional vibrations are uncoupled. If the cross-section of the blade has only one axis of symmetry, the shear center lies on the axis of symmetry. If the mass center and the shear center are very close, the proximity of the mass center and the shear center renders small coupling. The net aerodynamic forces and moment acting on a helicopter rotor blade are considered to pass through the aerodynamic center of the cross-section which is considered to be located around $1/4^{th}$ chord length from the leading edge which is, sometimes, also the center of gravity of the rotor blade. However, if the shear center is different and the net force does not act through the shear center, the blade undergoes twisting in addition to bending. Chapter 3 aims to develop the analytical formulations to solve for the natural frequency and time-varying deflections from the governing equations of motion of the triply coupled rotor blade. The triply coupled helicopter rotor blade vibration is also known as the flap-lag-torsion coupled vibration.

The blade section properties estimated in Chapter 2 will remain the same in this chapter for the frequency analysis.

3.2 Triply Coupled Vibration Analysis: Governing Equations of Motion

Depending on the nature of the constructional geometry of the helicopter rotor blade, different methodologies are proposed to develop the mathematical model of the triply coupled vibration analysis. Generally, for any kind of helicopter main rotor, the blades are treated as vibrating beams under different aerodynamic forcing functions. However, consideration of each helicopter rotor blade as a beam offers different solution strategies depending on the end conditions of the rotor blades. These end conditions vary from helicopter to helicopter models as fully articulated, teetering, or hingeless roots which are discussed in detail in Chapter 1. The mathematical model of the triply coupled vibration analysis in Chapter 3 is based on the one-dimensional (1-D) analysis with the configuration of the Bo 105 helicopter rotor blade in which the blade roots are bolted to connect with the rotor hub and are appropriately considered to have the cantilevered beam fixed end conditions (Panda and Chopra, 1986).

The bolted end condition of the Bo 105 helicopter rotor blade allows it to be considered as the type of a hingeless rotor blade where there is no physical hinge present to support the flapping motion of the blades. Instead of the whole blade flapping, the blade itself flexes to compensate for the forces as described in Chapter 1. Although complex in structural configuration, the unique feature of the cantilevered end condition of the Bo 105 helicopter rotor blade is, it is mechanically simple thereby requiring less maintenance and at the same time, the rotor system is provided with a high degree of control power. With the passage of time, the hingeless rotor system becomes more common because of the design flexibility. In addition to that, the fixed end condition of the Bo 105 rotor blade has made it ideal and simple to be used in the mathematical model of triply coupled vibration analysis by using the analogy of a rotating beam.

The governing equations of motion of a triply coupled beam might be different for different structural geometries. This is due to the inclusion or noninclusion of several other terms which involve the coupling terms due to the centrifugal force, the Coriolis component, shear deformation, rotary inertia, warping rigidity, and thermal changes. For some structures,

noninclusion of some of these terms significantly affects the vibrational response. For example, for thin walled beams, the warping rigidity has a great impact on the natural frequency and therefore, is considered as an important parameter in the mathematical model. For operating in an environment where the temperature gradient is very high and the materials are susceptible to that temperature gradient, thermal parameters play a key role. Consideration of the shear deformation and the rotary inertia are important for beams having relatively shorter length compared to the cross-sectional dimensions. For this analysis, the Bo 105 helicopter rotor blade model is ideal to be considered as the Euler-Bernoulli beam because the blade can be closely approximated as a long, thin plate with a solid, closed cross-section for which the effect of the cross-sectional warping can be ignored due to its relatively minor role (Hashemi and Richard, 2000).

The geometric features of the Bo 105 helicopter rotor blade which is long and thin, have made it suitable to model appropriately so that the cross-section can be approximately considered as singly symmetric with respect to the principal centroidal axis aligned with the chord as explained in Chapter 2. The rotor blade is subjected to the out-of-plane bending (flapping) force, $f_z(x,t)$ along global z axis; the in-plane bending (lead-lag) force, $f_y(x,t)$ along global y axis; and the torsional load, $m_x(x,t)$ about global x axis as shown in Figs. 3.1 and 3.2. The corresponding mathematical model of a 1-D, singly symmetric rotor blade can be represented by the following governing equations:

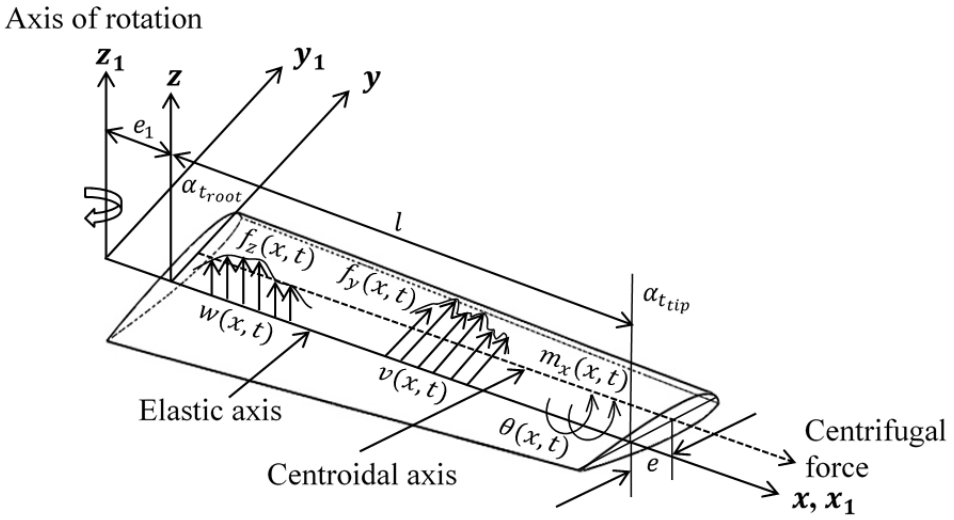

Fig. 3.1. The helicopter rotor blade subjected to bending-bending-torsion deformations

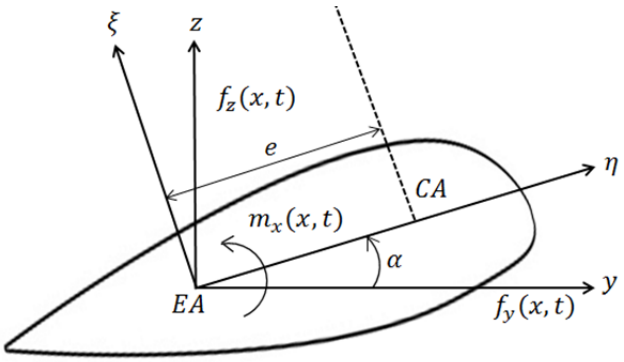

Fig. 3.2. Cross-section of the rotor blade with the externally applied aerodynamic loadings

$$[D_{by}(x,t)w''(x,t) + D_{bzy}(x,t)v''(x,t)]'' - [T(x)w'(x,t)]' - [\Omega^2 me(x+e_1)\theta(x,t)\,cos\alpha(x,t)]' + m[\ddot{w}(x,t) + e\ddot{\theta}(x,t)cos\alpha(x,t)] = f_z(x,t) + [\Omega^2 mexsin\alpha(x,t)]' \tag{3.1}$$

$$[D_{bz}(x,t)v''(x,t) + D_{bzy}(x,t)w''(x,t)]'' - [T(x)v'(x,t)]' + [\Omega^2 me(x+e_1)\theta(x,t)sin\alpha(x,t)]' + \Omega^2 me\theta(x,t)sin\alpha(x,t) + m[\ddot{v}(x,t) - e\ddot{\theta}(x,t)sin\alpha(x,t)] - \Omega^2 mv(x,t) = f_y(x,t) + [\Omega^2 me(x+e_1)cos\alpha(x,t)]' + \Omega^2 mecos\alpha(x,t) \tag{3.2}$$

$$-[D_t(x)\theta'(x,t)]' - \Omega^2 me(x+e_1)[v'(x,t)sin\alpha(x,t) - w'(x,t)cos\alpha(x,t)] + \Omega^2 mev(x,t)sin\alpha(x,t) + \Omega^2 m\,cos\,2\alpha(x,t)\,(\kappa_{m2}^2 - \kappa_{m1}^2)\theta(x,t) + m\kappa_m^2\ddot{\theta}(x,t) - me[\ddot{v}(x,t)sin\alpha(x,t) - \ddot{w}(x,t)cos\alpha(x,t)] = m_x(x,t) - \Omega^2 m[(\kappa_{m2}^2 - \kappa_{m1}^2)sin\alpha(x,t)cos\alpha(x,t)] \tag{3.3}$$

with

$$T(x) = \int_x^l \Omega^2 m(x+e_1)dx \tag{3.4}$$

$$\alpha(x,t) = \alpha_t(x) + \alpha_p(t) + \theta(x,t) \tag{3.5}$$

$$D_{by}(x,t) = D_{b\eta}\,cos^2\,\alpha(x,t) + D_{b\xi}sin^2\alpha(x,t) \tag{3.6}$$

$$D_{bz}(x,t) = D_{b\xi}\,cos^2\,\alpha(x,t) + D_{b\eta}sin^2\alpha(x,t) \tag{3.7}$$

$$D_{bzy}(x,t) = (D_{b\xi} - D_{b\eta})sin\alpha(x,t)cos\alpha(x,t) \tag{3.8}$$

where D_{by} and D_{bz} are the bending stiffnesses with respect to the y axis and z axis, respectively, and $D_{b\eta}$ and $D_{b\xi}$ are the bending stiffnesses with respect to the principal η axis and ξ axis through the shear center, respectively, in Fig. 3.2. w, v, and θ are termed as the out-of-plane or flapping, in-plane or lead-lag, and torsional deflections, respectively. α is the total blade cross-section angle at any station x prior to any deformation. T, l, α_p, α_t, e_1, e, m, and Ω indicate the centrifugal tension, the blade length, the blade pitch angle, the pretwist angle, the hinge offset, the offset between the shear center and the centroid, the mass per unit length of the blade, and the angular speed of the rotor, respectively. κ_m is the polar mass radius of gyration about the elastic axis and κ_{m1} and κ_{m2} are the mass radii of gyration about the neutral axis and the axis normal to chord through the shear center, respectively, with $\kappa_m^2 = \kappa_{m2}^2 + \kappa_{m1}^2$. For expressing the derivative terms, " $'$ " and " $\dot{}$ " indicate the derivatives with respect to x and t, respectively. Unless stated specifically, for the convenience of writing, only the dependent variable symbols will be used from now onwards without showing the respective independent variables of which the dependent variables are the functions.

3.3 Boundary Conditions

Equations (3.1)–(3.3) represent an IBVP and involve ten BCs for the most general case: four for out-of-plane bending, four for in-plane bending, and two for torsion measured with respect to the elastic axis. For small torsional load and hence the corresponding deformation compared to bending, values of D_{by}, D_{bz}, and D_{bzy} are negligibly affected by θ in Eqs. (3.6)–(3.8). However, in contrast to that, magnitudes of the aerodynamic loads are significantly affected by θ since they are sensitive to small change in α described in Eq. (3.5). Therefore, Eqs. (3.1)–(3.3) can be modified with reasonable accuracy in terms of bending stiffnesses and the corresponding BCs for the clamped-free end conditions of the helicopter blade are specified as:

at $x = 0$: $\quad w(0,t) = 0; \quad w'(0,t) = 0; \quad v(0,t) = 0; \quad v'(0,t) = 0; \quad \theta(0,t) = 0$ (3.9)

at $x = l$: $\quad S_z(l,t) = M_y(l,t) = S_y(l,t) = M_z(l,t) = Q(l,t) = 0$ (3.10)

where

$$S_z = -M_y' + Tw' + \Omega^2 me(x + e_1)(sin\alpha + \theta cos\alpha) \tag{3.11}$$

$$S_y = -M_z' + Tv' + \Omega^2 me(x + e_1)(cos\alpha - \theta sin\alpha) \tag{3.12}$$

$$M_y = D_{by}w'' + D_{bzy}v'' \tag{3.13}$$

$$M_z = D_{bz}v'' + D_{bzy}w'' \tag{3.14}$$

$$Q = D_t\theta' \tag{3.15}$$

where S_y and S_z are the shear forces along global y and z axis, respectively, M_y and M_z are the bending moments about global y and z axis, respectively, and Q is the torque about the global x axis. Equations (3.1)–(3.3) along with the BCs in Eqs. (3.9) and (3.10) contain the term α, which has a very little contribution to significantly change the vibration frequency. However, when calculating the forcing functions, α must be included appropriately since the aerodynamic forcing functions vary considerably with the spanwise change of α. From the specifications of the Bo 105 helicopter rotor blade, α varies linearly from the blade root to the blade tip. For free vibration (with no externally applied loadings), $\alpha = f_z = f_y = m_x = 0$, Eqs. (3.1)–(3.3) can be written with the stiffness terms which are considered piecewise linear or constant.

3.4 Method of Solution: Natural Frequencies of Free Vibration

Approximate techniques are required to solve Eqs. (3.1)–(3.3) in terms of the natural frequencies. This study uses the modified Galerkin approach to solve the governing equations with some approximations, in which the displacements are expressed in finite series of known functions as,

$$w(x) = W_n(x) = a_n\phi_{nb}(x) \qquad n = 1,2,3,\ldots \tag{3.16}$$

$$v(x) = V_n(x) = b_n\phi_{nb}(x) \qquad n = 1,2,3,\ldots \tag{3.17}$$

$$\theta(x) = \Theta_n(x) = c_n\phi_{nt}(x) \qquad n = 1,2,3,\ldots \tag{3.18}$$

where $W_n(x)$, $V_n(x)$, and $\Theta_n(x)$ are the fundamental uncoupled out-of-plane bending, in-plane bending, and torsional vibration mode shapes of the rotor blade, respectively. a_n, b_n, and c_n are the unknown coefficients and ϕ_{nb} and ϕ_{nt} are the normal functions governing bending and torsion, respectively. Properties of ϕ_{nb} and ϕ_{nt} are such that they satisfy the geometric or essential BCs in Eq. (3.9). Evaluation of a_n, b_n, and c_n is carried out by forming a set of linear simultaneous equations derived from the application of the following relationships:

$$\int_0^l W_n L_w(w,v,\theta)dx + \left[M_y W_n'\right]_0^l + \left[S_z W_n\right]_0^l = 0 \tag{3.19}$$

$$\int_0^l V_n L_v(w,v,\theta)dx + \left[M_z V_n'\right]_0^l + \left[S_y V_n\right]_0^l = 0 \tag{3.20}$$

$$\int_0^l \Theta_n L_\theta(w,v,\theta)dx + \left[Q\Theta_n\right]_0^l = 0 \tag{3.21}$$

where $L_w(w,v,\theta)$, $L_v(w,v,\theta)$, and $L_\theta(w,v,\theta)$ denote Eqs. (3.1), (3.2), and (3.3), respectively, with all the right-hand terms transferred to the left hand side. For static or externally applied loads, the set of equations formed by Eqs. (3.19)–(3.21) are nonhomogeneous. For a characteristic value problem, such as free vibrations, Eqs. (3.19)–(3.21) are homogeneous.

Equations (3.19)–(3.21) are known as the modified Galerkin procedure because of the presence of the boundary terms in the equations. In the conventional Galerkin method, the modal functions in Eqs. (3.16)–(3.18) are to be chosen in such a way so that they satisfy both the geometric and the force BCs, which is a little challenging to execute. Therefore, the force BCs are added in Eqs. (3.19)–(3.21) leaving the modal functions to satisfy only the geometric BCs. In this way, the stipulations on the chosen modal functions to satisfy both types of BCs are relaxed and therefore, the procedure is called as the modified Galerkin method.

In order to solve Eqs. (3.19)–(3.21), the frequency term, ω needs to be introduced in the functions $L_w(w,v,\theta)$, $L_v(w,v,\theta)$, and $L_\theta(w,v,\theta)$. To do that, at first, Eqs. (3.1)–(3.3) are written for the free vibration. There are some coupling terms in Eqs. (3.1)–(3.3) associated with the centrifugal force. Among them, some terms take the forms of the applied loadings which tend to deflect the blade even in the absence of the externally applied loads. Because of this fact, they are written on the right-hand side of the equations along with the externally applied loadings. For the free vibration, those terms as well as the externally applied loadings are cancelled out from the equations. Using separation of variables technique and simple harmonic motion assumptions, the governing equations of the free vibration of the rotating blade are:

$$(D_{by}w'' + D_{bzy}v'')'' - (Tw')' - [\Omega^2 me(x+e_1)\theta cos\alpha]' - m\omega^2(w + e\theta cos\alpha) = 0 \tag{3.22}$$

$$(D_{bz}v'' + D_{bzy}w'')'' - (Tv')' + [\Omega^2 me(x+e_1)\theta sin\alpha]' + \Omega^2 me\theta sin\alpha - m\omega^2(v - e\theta sin\alpha) - \Omega^2 mv = 0 \tag{3.23}$$

$$-(D_t\theta')' - \Omega^2 me(x+e_1)(v'sin\alpha - w'cos\alpha) + \Omega^2 mevsin\alpha + \Omega^2 m\,cos(2\alpha)(\kappa_{m2}^2 - \kappa_{m1}^2)\theta - m\omega^2\kappa_m^2\theta + me\omega^2(vsin\alpha - wcos\alpha) = 0 \tag{3.24}$$

Since α has little significance on the frequency, setting $\alpha = 0$ (zero pitched untwisted blade) in Eqs. (3.22)–(3.24) decouples the governing equations up to a certain extent. Moreover, from Chapter 2, the cross-section of the Bo 105 rotor blade can be approximately considered as singly symmetric for which the product of the moment of inertia vanishes. Once D_{by}, D_{bz}, and D_t are piecewise constant along the length of the blade, using $\alpha = 0$ in Eqs. (3.22)–(3.24) gives,

$$D_{by}w'''' - (Tw')' - [\Omega^2 me(x+e_1)\theta]' - m\omega^2(w + e\theta) = 0 \tag{3.25}$$

$$D_{bz}v'''' - (Tv')' - m\omega^2 v - \Omega^2 mv = 0 \tag{3.26}$$

$$-D_t\theta'' + \Omega^2 me(x+e_1)w' + \Omega^2 m(\kappa_{m2}^2 - \kappa_{m1}^2)\theta - m\omega^2\kappa_m^2\theta - m\omega^2 ew = 0 \tag{3.27}$$

When the left side expressions of Eqs. (3.25)–(3.27) are substituted for the left side expressions in Eqs. (3.1)–(3.3), respectively, and the right-hand side expressions in Eqs. (3.1)–(3.3) are transferred to the left for no externally applied loading (free vibration) with $\alpha = 0$, then, $L_w(w, v, \theta)$, $L_v(w, v, \theta)$, and $L_\theta(w, v, \theta)$ are expressed for any mode n as,

$$L_w(w, v, \theta) = D_{by}w'''' - (Tw')' - [\Omega^2 me(x+e_1)\theta]' - m\omega_n^2 w - m\omega_n^2 e\theta \tag{3.28}$$

$$L_v(w, v, \theta) = D_{bz}v'''' - (Tv')' - m\omega_n^2 v - \Omega^2 mv - [\Omega^2 me(x+e_1)]' - \Omega^2 me \tag{3.29}$$

$$L_\theta(w, v, \theta) = -D_t\theta'' + \Omega^2 me(x+e_1)w' + \Omega^2 m(\kappa_{m2}^2 - \kappa_{m1}^2)\theta - m\omega_n^2\kappa_m^2\theta - m\omega_n^2 ew \tag{3.30}$$

Using the above expressions in Eqs. (3.19)–(3.21) with the application of Eqs. (3.11)–(3.15),

$$\int_0^l \left(D_{by}w''''W_n - (Tw')'W_n - [\Omega^2 me(x+e_1)\theta]'W_n - m\omega_n^2 wW_n - m\omega_n^2 e\theta W_n\right)dx + \left[D_{by}w''W_n'\right]_0^l + \left[-D_{by}w'''W_n + Tw'W_n + \Omega^2 me(x+e_1)\theta W_n\right]_0^l = 0 \tag{3.31}$$

$$\int_0^l (D_{bz}v''''V_n - (Tv')'V_n - m\omega_n^2 vV_n - \Omega^2 mvV_n - [\Omega^2 me(x+e_1)]'V_n - \Omega^2 meV_n)dx + [D_{bz}v''V_n']_0^l + [-D_{bz}v'''V_n + Tv'V_n + \Omega^2 me(x+e_1)V_n]_0^l = 0 \quad (3.32)$$

$$\int_0^l (-D_t\theta''\Theta_n + \Omega^2 me(x+e_1)w'\Theta_n + \Omega^2 m(\kappa_{m2}^2 - \kappa_{m1}^2)\theta\Theta_n - m\omega_n^2\kappa_m^2\theta\Theta_n - m\omega_n^2 ew\Theta_n)dx + [D_t\theta'\Theta_n]_0^l = 0 \quad (3.33)$$

Performing integration by parts in Eqs. (3.31)–(3.33), the following seven relationships are obtained:

$$\int_0^l D_{by}w''''W_n dx = \left[D_{by}w'''W_n\right]_0^l - \left[D_{by}w''W_n'\right]_0^l + \int_0^l D_{by}\, w''W_n'' dx \quad (3.34)$$

$$\int_0^l (Tw')'W_n dx = [Tw'W_n]_0^l - \int_0^l Tw'W_n'\, dx \quad (3.35)$$

$$\int_0^l [\Omega^2 me(x+e_1)\theta]'W_n dx = [\Omega^2 me(x+e_1)\theta W_n]_0^l - \int_0^l \Omega^2 me(x+e_1)\theta W_n' dx \quad (3.36)$$

$$\int_0^l D_{bz}v''''V_n dx = [D_{bz}v'''V_n]_0^l - [D_{bz}v''V_n']_0^l + \int_0^l D_{bz}\, v''V_n'' dx \quad (3.37)$$

$$\int_0^l (Tv')'V_n dx = [Tv'V_n]_0^l - \int_0^l Tv'V_n'\, dx \quad (3.38)$$

$$\int_0^l [\Omega^2 me(x+e_1)]'V_n dx = [\Omega^2 me(x+e_1)V_n]_0^l - \int_0^l \Omega^2 me(x+e_1)V_n' dx \quad (3.39)$$

$$\int_0^l -D_t\theta''\Theta_n dx = -[D_t\theta'\Theta_n]_0^l + \int_0^l D_t\theta'\Theta_n' dx \quad (3.40)$$

The above relationships are applied in Eqs. (3.31)–(3.33) and after the limiting terms have been cancelled out, the following equations are obtained:

$$\int_0^l \left[D_{by}w''W_n'' + Tw'W_n' + \Omega^2 me(x+e_1)\theta W_n' - m\omega_n^2(w+e\theta)W_n\right]dx = 0 \quad (3.41)$$

$$\int_0^l [D_{bz}v''V_n'' + Tv'V_n' + \Omega^2 me(x+e_1)V_n' - m\omega_n^2 vV_n - \Omega^2 m(v+e)V_n]dx = 0 \quad (3.42)$$

$$\int_0^l [D_t\theta'\Theta_n' + \Omega^2 me(x+e_1)w'\Theta_n + \Omega^2 m(\kappa_{m2}^2 - \kappa_{m1}^2)\theta\Theta_n - m\omega_n^2(\kappa_m^2\theta + ew)\Theta_n]dx = 0 \tag{3.43}$$

where the mode shapes are defined by Eqs. (3.16)–(3.18) as,

$$\phi_{nb}(x) = cosh(\beta_n x) - cos(\beta_n x) - N[sinh(\beta_n x) - sin(\beta_n x)] \tag{3.44}$$

$$\phi_{nt} = sin\left[\frac{(2n-1)\pi x}{2l}\right] \tag{3.45}$$

and,

$$N = \frac{\sin(\beta_n l) + \sinh(\beta_n l)}{\cos(\beta_n l) + \cosh(\beta_n l)} \tag{3.46}$$

with $\beta_n l$ as the root of the characteristic equation of transverse vibration of a cantilever beam (Sarker et al., 2016). From Eqs. (3.16) and (3.17), it is obvious that both $W_n(x)$ and $V_n(x)$ share the common normal function ϕ_{nb} for the bending behavior of a nonrotating beam clamped at one end and free at the other end. This is also true for the rotating beam, however, in that case, ϕ_{nb} is changed and expressed as (Genta, 2005),

$$\phi_{nbr} = sin(\beta_n x) - sinh(\beta_n x) - N_r[cos(\beta_n x) - cosh(\beta_n x)] \tag{3.47}$$

with

$$N_r = \frac{sin(\beta_n l) + sinh(\beta_n l)}{cos(\beta_n l) + cosh(\beta_n l)} \tag{3.48}$$

where the suffix r in ϕ_{nbr} and N_r indicates that they are applicable for the rotating beam or blade.

Careful review of Eqs. (3.41)–(3.43) reveals that some terms in Eq. (3.42) do not include any dependent variable unlike Eqs. (3.41) and (3.43) and the whole equation contains only one variable, v. This indicates that, Eq. (3.42) has been decoupled completely from the other two equations and requires a separate solution method. To find the out-of-plane bending and torsional vibration frequencies from Eqs. (3.41) and (3.43), approximations to the displacements are

chosen as mentioned in Eqs. (3.16) and (3.18). This, when applied into Eqs. (3.41) and (3.43) with the expressions stated in Eqs. (3.44) and (3.45), gives the following algebraic equations:

$$a_n \int_0^l \left[D_{by}(\phi''_{nb})^2 + T(\phi'_{nb})^2 - m\omega_n^2\phi_{nb}^2\right]dx + c_n \int_0^l [\Omega^2 me(x+e_1)\phi_{nt}\phi'_{nb} - m\omega_n^2 e\phi_{nt}\phi_{nb}]dx = 0 \tag{3.49}$$

$$a_n \int_0^l [\Omega^2 me(x+e_1)\phi_{nt}\phi'_{nb} - m\omega_n^2 e\phi_{nt}\phi_{nb}]dx + c_n \int_0^l [D_t(\Theta_n{}')^2 + \Omega^2 m(\kappa_{m2}^2 - \kappa_{m1}^2)\Theta_n^2 - m\omega_n^2\kappa_m^2\Theta_n^2]dx = 0 \tag{3.50}$$

Equations (3.49) and (3.50) are written in the matrix form,

$$\begin{bmatrix} X_1 & Y_1 \\ X_2 & Y_2 \end{bmatrix} \begin{bmatrix} a_n \\ c_n \end{bmatrix} = \begin{bmatrix} 0 \\ 0 \end{bmatrix} \tag{3.51}$$

where

$$X_1 = \int_0^l \left[D_{by}(\phi''_{nb})^2 + T(\phi'_{nb})^2 - m\omega_n^2\phi_{nb}^2\right]dx \tag{3.52}$$

$$Y_1 = X_2 = \int_0^l [\Omega^2 me(x+e_1)\phi_{nt}\phi'_{nb} - m\omega_n^2 e\phi_{nt}\phi_{nb}]dx \tag{3.53}$$

$$Y_2 = \int_0^l [D_t(\phi'_{nt})^2 + \Omega^2 m(\kappa_{m2}^2 - \kappa_{m1}^2)\phi_{nt}^2 - m\omega_n^2\kappa_m^2\phi_{nt}^2]dx \tag{3.54}$$

The values of X_1, X_2, Y_1, and Y_2 are evaluated using MATLAB (MathWorks Corporation, 2015) by utilizing Eqs. (3.44)–(3.46). The expression of T is to be found from Eq. (3.4). In order to obtain a nontrivial solution, the vanishing of the determinant of Eq. (3.51) below gives a quadratic equation in terms of ω_n^2, after solving which, the natural frequency, ω_n is obtained for out-of-plane bending and torsional vibration.

$$\begin{vmatrix} X_1 & Y_1 \\ X_2 & Y_2 \end{vmatrix} = 0 \tag{3.55}$$

Solution of Eq. (3.42) gives the frequency for the in-plane bending vibration which requires Eq. (3.17) to be used. This time, ϕ_{nbr} from Eq. (3.47) will be used in Eq. (3.17) in place of ϕ_{nb}. From Eq. (3.17), V_n is given in terms of a unit tip displacement and Eq. (3.42) becomes,

$$\int_0^l [D_{bz}(\phi''_{nbr})^2 + T(\phi'_{nbr})^2 + \Omega^2 me(x+e_1)\phi'_{nbr} - m\omega_n^2\phi_{nbr}^2 - \Omega^2 m(\phi_{nbr}+e)\phi_{nbr}]dx = 0$$

$$\Rightarrow \omega_n^2 = \frac{1}{m\int_0^l \phi_{nbr}^2 dx}\int_0^l [D_{bz}(\phi''_{nbr})^2 + T(\phi'_{nbr})^2 + \Omega^2 me(x+e_1)\phi'_{nbr} - \Omega^2 m(\phi_{nbr}+e)\phi_{nbr}]dx \tag{3.56}$$

As before, T is evaluated from Eq. (3.4) and the above integrals are evaluated by MATLAB (MathWorks Corporation, 2015). The out-of-plane and in-plane bending vibration frequencies of the helicopter rotor blade are also known as the flapping and the lead-lag frequencies, respectively.

3.5 Method of Solution: Time-Varying Deflections for Forced Vibration

For forced vibration, the time-varying deflections will be estimated from the normal mode method. To apply this method, it is assumed that the solutions are harmonic for the free vibration with the following forms:

$$w(x,t) = W_n(x)e^{j\omega_n t} \tag{3.57}$$

$$v(x,t) = V_n(x)e^{j\omega_n t} \tag{3.58}$$

$$\theta(x,t) = \Theta_n(x)e^{j\omega_n t} \tag{3.59}$$

Substitution of Eqs. (3.57)–(3.59) into Eqs. (3.1)–(3.3) for the free vibration analysis and the nonrotating case of the helicopter rotor blade ($\Omega = 0$) with $\alpha = 0$ results in the following equations:

$$D_{by}W_n'''' - m\omega_n^2 W_n - me\omega_n^2\Theta_n = 0 \tag{3.60}$$

$$D_{bz}V_n'''' - m\omega_n^2 V_n = 0 \tag{3.61}$$

$$-D_t\Theta''_n - m\omega_n^2\kappa_m^2\Theta_n - me\omega_n^2 W_n = 0 \tag{3.62}$$

Since the rotor blade is subjected to triply coupled vibratory loads, the conventional uncoupled orthogonality relationships are not applicable. Therefore, the corresponding

orthogonality relationship has to be developed for the forced vibration of the nonrotating case which is also used for the rotating case.

3.5.1 Orthogonality Relationship for the Forced Vibration of a Triply Coupled Beam/Helicopter Rotor Blade

Multiplying Eq. (3.60) with W_m and integrating from 0 to l,

$$\int_0^l \left(D_{by} W_n'''' W_m - m\omega_n^2 W_n W_m - me\omega_n^2 \Theta_n W_m\right) dx = 0 \tag{3.63}$$

Interchanging m and n in Eq. (3.63),

$$\int_0^l \left(D_{by} W_m'''' W_n - m\omega_m^2 W_m W_n - me\omega_m^2 \Theta_m W_n\right) dx = 0 \tag{3.64}$$

Subtracting Eq. (3.64) from Eq. (3.63), applying integration by parts using the BCs in Eqs. (3.9) and (3.10) for $\Omega = \alpha = 0$,

$$(m\omega_m^2 - m\omega_n^2) \int_0^l W_m W_n dx + m\omega_m^2 \int_0^l eW_n \Theta_m dx - m\omega_n^2 \int_0^l eW_m \Theta_n dx = 0 \tag{3.65}$$

Similarly, multiplying Eq. (3.61) by V_m and Eq. (3.62) by Θ_m and following the above procedure,

$$(m\omega_m^2 - m\omega_n^2) \int_0^l V_m V_n dx = 0 \tag{3.66}$$

$$(m\omega_m^2 - m\omega_n^2) \int_0^l \kappa_m^2 \Theta_m \Theta_n dx + m\omega_m^2 \int_0^l eW_m \Theta_n dx - m\omega_n^2 \int_0^l eW_n \Theta_m dx = 0 \tag{3.67}$$

Adding Eqs. (3.65)–(3.67) altogether,

$$(m\omega_m^2 - m\omega_n^2) \int_0^l [W_m W_n + V_m V_n + e(W_m \Theta_n + W_n \Theta_m) + \kappa_m^2 \Theta_m \Theta_n] dx = 0 \tag{3.68}$$

For two different modes m and n, ω_m and ω_n are different, therefore, from Eq. (3.68), $(m\omega_m^2 - m\omega_n^2) \neq 0$. Consequently, the orthogonality condition for the triply coupled beam is written as,

$$\int_0^l [W_m W_n + V_m V_n + e(W_m \Theta_n + W_n \Theta_m) + \kappa_m^2 \Theta_m \Theta_n] dx = \delta_{mn} \tag{3.69}$$

where δ_{mn} is the Kronecker delta and is defined as,

$$\delta_{mn} = 1; \quad m = n \tag{3.70}$$

$$\delta_{mn} = 0; \quad m \neq n \tag{3.71}$$

The orthogonality condition in Eq. (3.69) can be used for the estimation of the time-varying deflections of the helicopter rotor blade which are expressed as series solutions:

$$w(x,t) = \sum_{n=1}^{\infty} W_n(x) q_n(t) \tag{3.72}$$

$$v(x,t) = \sum_{n=1}^{\infty} V_n(x) q_n(t) \tag{3.73}$$

$$\theta(x,t) = \sum_{n=1}^{\infty} \Theta_n(x) q_n(t) \tag{3.74}$$

where q_n is the generalized time coordinate for the n^{th} mode. For the forced vibration of a nonrotating beam, Eqs. (3.1)–(3.3) for $\alpha = 0$ reduce to,

$$D_{by} w'''' + m\ddot{w} + me\ddot{\theta} = f_z \tag{3.75}$$

$$D_{bz} v'''' + m\ddot{v} = f_y \tag{3.76}$$

$$-D_t \theta'' + m\kappa_m^2 \ddot{\theta} + me\ddot{w} = m_x \tag{3.77}$$

Substituting Eqs. (3.72)–(3.74) into Eqs. (3.75)–(3.77),

$$\sum_{n=1}^{\infty} D_{by} W_n'''' q_n + \sum_{n=1}^{\infty} m W_n \ddot{q_n} + \sum_{n=1}^{\infty} me\Theta_n \ddot{q_n} = f_z \tag{3.78}$$

$$\sum_{n=1}^{\infty} D_{bz} V_n'''' q_n + \sum_{n=1}^{\infty} m V_n \ddot{q_n} = f_y \tag{3.79}$$

$$\sum_{n=1}^{\infty} -D_t \Theta_n{}'' \, q_n + \sum_{n=1}^{\infty} m\kappa_m^2 \Theta_n \ddot{q_n} + \sum_{n=1}^{\infty} meW_n \ddot{q_n} = m_x \tag{3.80}$$

Multiplying Eqs. (3.78), (3.79), and (3.80) by W_m, V_m, and Θ_m, respectively, using the relationships from Eqs. (3.60)–(3.62), and adding them altogether,

$$\begin{aligned}\sum_{n=1}^{\infty} [&(m\omega_n^2 W_n + me\omega_n^2 \Theta_n) W_m q_n + mW_n W_m \ddot{q_n} + me\Theta_n W_m \ddot{q_n} + m\omega_n^2 V_n V_m q_n \\ &+ mV_n V_m \ddot{q_n} + (m\omega_n^2 \kappa_m^2 \Theta_n + me\omega_n^2 W_n)\Theta_m q_n + m\kappa_m^2 \Theta_n \Theta_m \ddot{q_n} \\ &+ meW_n \Theta_m \ddot{q_n}] = f_z W_m + f_y V_m + m_x \Theta_m\end{aligned} \tag{3.81}$$

After rearranging the terms and integrating from 0 to l,

$$\begin{aligned}\sum_{n=0}^{\infty} \Big\{ &m\ddot{q_n} \int_0^l [W_n W_m + V_n V_m + e(W_m \Theta_n + W_n \Theta_m) + \kappa_m^2 \Theta_n \Theta_m] dx \\ &+ m\omega_n^2 q_n \int_0^l [W_n W_m + V_n V_m + e(W_m \Theta_n + W_n \Theta_m) \\ &+ \kappa_m^2 \Theta_n \Theta_m] \, dx \Big\} = \int_0^l (f_z W_m + f_y V_m + m_x \Theta_m) \, dx\end{aligned} \tag{3.82}$$

Using the orthogonality condition from Eqs. (3.69) and (3.70) for $n = m$,

$$\ddot{q_n} + \omega_n^2 q_n = \frac{1}{m} \int_0^l (f_z W_n + f_y V_n + m_x \Theta_n) \, dx = F_{zn} + F_{yn} + M_{xn} \tag{3.83}$$

with

$$F_{zn} = F_{zn}(t) = \frac{1}{m} \int_0^l f_z(x,t) W_n(x) \, dx = \frac{1}{m} F_{zng}(t) \tag{3.84}$$

$$F_{yn} = F_{yn}(t) = \frac{1}{m} \int_0^l f_y(x,t) V_n(x) \, dx = \frac{1}{m} F_{yng}(t) \tag{3.85}$$

$$M_{xn} = M_{xn}(t) = \frac{1}{m} \int_0^l m_x(x,t) \Theta_n(x) \, dx = \frac{1}{m} M_{xng}(t) \tag{3.86}$$

where $F_{zng}(t)$ and $F_{yng}(t)$ are the n^{th} generalized forces for the out-of-plane bending/flapping motion and the in-plane bending/lead-lag motion, respectively, and $M_{xng}(t)$ is the n^{th} generalized moment for torsional motion. Equation (3.83) is a second-order ordinary differential equation (ODE) the solution of which is obtained by Duhamel's integral as below,

$$q_n(t) = A_n\, cos(\omega_n t) + B_n\, sin(\omega_n t) + \frac{1}{\omega_n}\int_0^t [F_{zn}(\tau) + F_{yn}(\tau) + M_{xn}(\tau)]\, sin[\omega_n(t-\tau)]\, d\tau \tag{3.87}$$

where A_n and B_n are coefficients related to the ICs and ω_n is the natural frequency of the beam/helicopter rotor blade.

3.5.2 Time-Varying Deflections: Nonrotating Case

Equation (3.87) is derived for a general purpose uniform nonrotating subjected to the arbitrary forces, $F_{zn}(t)$ and $F_{yn}(t)$ and arbitrary moment, $M_{xn}(t)$. Substituting Eq. (3.87) into Eqs. (3.72)–(3.74), the forced response of the nonrotating beam/helicopter rotor blade in terms of the time-varying deflections become:

$$w(x,t) = \sum_{n=1}^{\infty} W_n(x)\{A_n\, cos(\omega_n t) + B_n\, sin(\omega_n t) + \frac{1}{\omega_n}\int_0^t [F_{zn}(\tau) + F_{yn}(\tau) + M_{xn}(\tau)]\, sin[\omega_n(t-\tau)]\, d\tau\} \tag{3.88}$$

$$v(x,t) = \sum_{n=1}^{\infty} V_n(x)\{A_n\, cos(\omega_n t) + B_n\, sin(\omega_n t) + \frac{1}{\omega_n}\int_0^t [F_{zn}(\tau) + F_{yn}(\tau) + M_{xn}(\tau)]\, sin[\omega_n(t-\tau)]\, d\tau\} \tag{3.89}$$

$$\theta(x,t) = \sum_{n=1}^{\infty} \Theta_n(x)\{A_n\, cos(\omega_n t) + B_n\, sin(\omega_n t) + \frac{1}{\omega_n}\int_0^t [F_{zn}(\tau) + F_{yn}(\tau) + M_{xn}(\tau)]\, sin[\omega_n(t-\tau)]\, d\tau\} \tag{3.90}$$

3.5.3 Time-Varying Deflections: Rotating Case

Equations (3.88)–(3.90) are not applicable for the forced response of the triply coupled beam/helicopter rotor blade. This is because, the helicopter rotor blade is treated as a rotating

beam which develops additional stiffness due to the rotation in addition to the geometric stiffness. The additional stiffness changes the value of the ω_n in Eqs. (3.88)–(3.90). Therefore, in order to find the forced response of the triply coupled rotating beam/helicopter rotor blade, the natural frequency of the nonrotating blade in Eqs. (3.88)–(3.90) must be replaced by the frequency of the rotating beam/helicopter rotor blade. In that sense, the basic forms of the Eqs. (3.88)–(3.90) are not changed and the only difference is made by ω_n corresponding to the nonrotating and the rotating cases.

Equations (3.72)–(3.74) represents the general solutions of the triply coupled helicopter rotor blade vibration due to the arbitrary aerodynamic lift, drag, and moment loadings in relation to Eqs. (3.84)–(3.86).

3.5.4 Evaluation of the Orthogonality Constants

Values of the orthogonality constants a_n, b_n, and c_n involved in Eqs. (3.88)–(3.90) with W_n, V_n, and Θ_n expressed by Eqs. (3.16)–(3.18) are required to be estimated in order to calculate the time-varying deflections. Since the value of e affects w significantly than v, therefore, for a specific case, the lead-lag motion can be thought of decoupled from the flapping and torsion for which the orthogonality condition in Eq. (3.69) for $n = m$ becomes,

$$\int_0^l (W_n^2 + 2eW_n\Theta_n + \kappa_m^2\Theta_n^2)dx = 1 \tag{3.91}$$

$$\Rightarrow \int_0^l (a_n^2\phi_{nb}^2 + 2ea_nc_n\phi_{nb}\phi_{nt} + c_n^2\kappa_m^2\phi_{nt}^2)dx = 1 \tag{3.92}$$

Separating the first equation from the matrix in Eq. (3.51), the following relationship between a_n and b_n is obtained:

$$c_n = -\frac{a_nX_1}{Y_1} \tag{3.93}$$

by using which, a_n from Eq. (3.92) is evaluated as,

$$a_n^2 = \frac{1}{\int_0^l \left(\phi_{nb}^2 - 2e\frac{X_1}{Y_1}\phi_{nb}\phi_{nt} + \kappa_m^2\frac{X_1^2}{Y_1^2}\phi_{nt}^2\right)dx} \tag{3.94}$$

where X_1 and Y_1 are to be evaluated by substituting the already obtained ω_n for the rotating beam/helicopter rotor blade. Both X_1 and Y_1 contain the two different values of ω_n^2 obtained from the polynomial resulted after the expansion of the determinant given by Eq. (3.55). These two values are ω_{nf}^2 and ω_{nt}^2, where the subscripts f and t stand for the flapping (out-of-plane bending) motion and the torsional motion, respectively. Consequently, c_n and a_n in Eqs. (3.93) and (3.94) also have two values corresponding to ω_{nf}^2 and ω_{nt}^2 and are expressed as below:

$$c_{nf} = -\frac{a_{nf} X_{1nf}}{Y_{1nf}} \tag{3.95}$$

$$c_{nt} = -\frac{a_{nt} X_{1nt}}{Y_{1nt}} \tag{3.96}$$

$$a_{nf}^2 = \frac{1}{\int_0^l \left(\phi_{nb}^2 - 2e \frac{X_{1nf}}{Y_{1nf}} \phi_{nb} \phi_{nt} + \kappa_m^2 \frac{X_{1nf}^2}{Y_{1nf}^2} \phi_{nt}^2 \right) dx} \tag{3.97}$$

$$a_{nt}^2 = \frac{1}{\int_0^l \left(\phi_{nb}^2 - 2e \frac{X_{1nt}}{Y_{1nt}} \phi_{nb} \phi_{nt} + \kappa_m^2 \frac{X_{1nt}^2}{Y_{1nt}^2} \phi_{nt}^2 \right) dx} \tag{3.98}$$

where a_{nf} and a_{nt} denote the values of a_n corresponding to ω_{nf} and ω_{nt}, respectively; c_{nf} and c_{nt} denote values of c_n corresponding to ω_{nf} and ω_{nt}, respectively; and X_{1nf}, X_{1nt}, Y_{1nf}, and Y_{1nt} indicate X_1 containing ω_{nf}, X_1 containing ω_{nt}, Y_1 containing ω_{nf}, and Y_2 containing ω_{nt}, respectively.

Since the lead-lag or in-plane bending motion can be considered as decoupled from the out-of-plane/flapping and torsional motions, the corresponding orthogonality constant b_n can be expressed as,

$$b_n^2 = \frac{1}{\int_0^l \phi_{nbr}^2 dx} \tag{3.99}$$

where expressions of ϕ_{nb}, ϕ_{nt}, and ϕ_{nbr} in Eqs. (3.95)–(3.99) are to be used from Eqs. (3.44)–(3.48) and the corresponding definite integrals can be obtained from MATLAB (MathWorks Corporation, 2015).

CHAPTER 4

Dynamics in the Hovering Flight

4.1 Hovering—A Unique Feature of Rotary-Wing Aircrafts

Hovering is the one of the unique features of the helicopter flight options which is not available in the fixed-wing aircrafts. The capacity of hovering has made the helicopter suitable for specific tasks to be performed. Among all the powered flights (hovering, vertical, forward, sideward, or rearward), hovering is the most challenging part of flying a helicopter. The reason is, in the hovering flight, the helicopter generates its own air velocity acting against the fuselage and the flight control surfaces, which is gusty in nature. The end result is the constant control inputs and corrections by the pilot to keep the helicopter in an equilibrium position. The ability of the helicopter to hover comes from the lift component which is the force developed by the main rotor blades to overcome the aircraft weight due to gravity. All helicopters spend considerable time in hover for different purposes. Therefore, they are specifically designed to be operationally efficient in the hovering flight for which the vibratory airloads need to be calculated. Chapter 4 aims to analytically formulate the blade airloads of the triply coupled Bo 105 helicopter rotor blade for the hovering flight.

4.2 Principle of the Hovering Flight

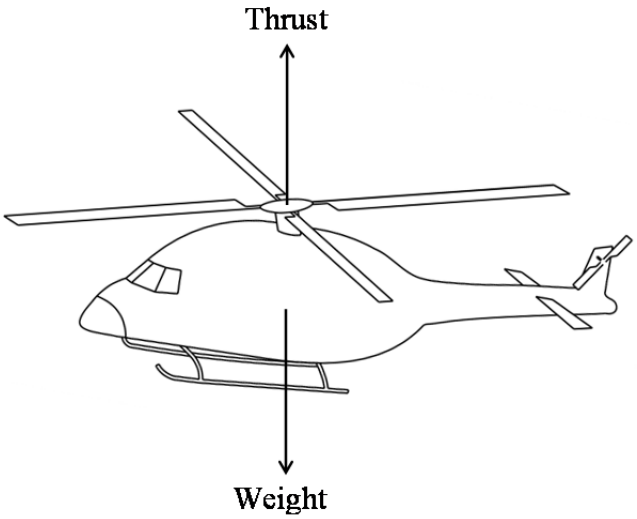

Fig. 4.1. Force balance of a helicopter during hovering flight

The helicopter is a lift producing machine with a constant rotational speed of the of rotor blades. The lifting capability of any part of a rotating blade is related to its local AoA, α_a and the local dynamic pressure. As the blades of the helicopter rotate, the velocity difference between the airstreams passing over the top surface and beneath the bottom surface of the airfoil creates the net lift force. If the airfoil is symmetric in shape, the velocity difference is zero. Therefore, for a helicopter rotor blade having a symmetric airfoil with no built-in twist angle α_t, no lift force is produced unless the pilot exerts a positive collective input to achieve a nonzero pitching angle, α_p for all the rotor blades, simultaneously. However, in this analysis, the Bo 105 helicopter rotor blade uses NACA 23012 airfoil which is asymmetric in nature. For that, although, no collective input is required at least to generate a positive lift force, still the pilot exerts the collective input to provide a vertical acceleration of the helicopter in order to reach a specific height within the shortest time. Once it is done, the collective input is adjusted to stop generating the extra lift more than the weight of the helicopter for a constant rotational speed of the main rotor, so that, the helicopter hovers in an equilibrium position. In that position, the rotor blades generate as much thrust, T_h as necessary to overcome its weight, W_g and from Newton's second law,

$$T_h = W_g \tag{4.1}$$

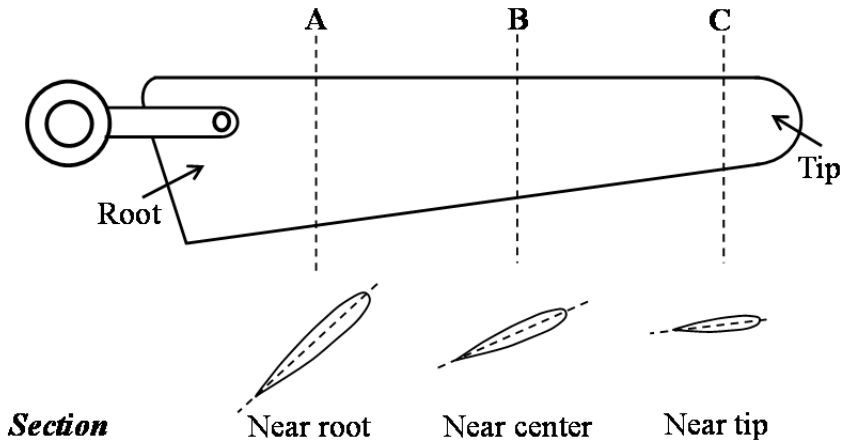

Fig. 4.2. Distribution of the spanwise twist for a typical helicopter rotor blade

Because of the lift differential due to different rotational relative wind values along the blade, the blade needs to be designed with a twist to alleviate the internal blade stress and to distribute the lifting force more evenly along the length. The Bo 105 helicopter blade is a built-in

twist of −8°, and the rate of twist varies with a ‘nose down’ tendency from the root to the tip demonstrated in Fig. 4.2.The sign convention states that the nose up rotation is positive and the nose down rotation is negative. Hence, the linear rate of twist is negative from the root to the tip of the blade. The built-in blade twist produces higher overall pitch angles near the root where the velocity is low and lower pitch angles near the tip where the velocity is high. On the other hand, the lift generated is proportional to the tangential velocity which increases linearly from the blade root to the blade tip. Therefore, such distribution of the twist angle shown in Fig. 4.2 helps to distribute the lift force more evenly on the helicopter rotor blade.

4.3 Estimation of the Blade Loadings at Hovering Flight—The Aerodynamic Strip Theory

The external forces and moment acting on the helicopter rotor blade for any flight condition are the aerodynamic lift, drag, and the pitching moment induced due to the movement of the airfoil through the air. The helicopter is treated as a lifting machine with low disk loading (DL) (Leishman, 2006) and the two dimensional quasi-steady strip theory can be applied to estimate the aerodynamic forces and moment. The aerodynamic strip theory considers the individual element of a rotor blade as a thin strip, the blade geometry, and the elemental forces and torque. The overall lift, drag, and pitching moment can be obtained by integrating along the entire blade over a rotor revolution. To implement the aerodynamic strip theory successfully, there are certain assumptions to be applied which are discussed in the following section.

4.3.1 Basic Assumptions

The geometric, elastic, and aerodynamic environmental assumptions regarding the rotor blade include the following in order to appropriately apply the strip theory:

1. The rotor blade can be considered to be a thin, flexible rotating cantilever beam attached to the hub with a root offset.

2. The blade does not stall.

3. Shear is negligible.

4. The helicopter rotor disk plane is subjected to low DL.

5. The compressibility effect is small and the reverse flow effect is neglected.

6. During deformation, the cross-section of the blade is assumed to remain plane and normal to the elastic axis.

7. The flow always remains attached to the airfoil.

4.3.2 Aerodynamic Lift, Drag, and Pitching Moment in Hovering Flight

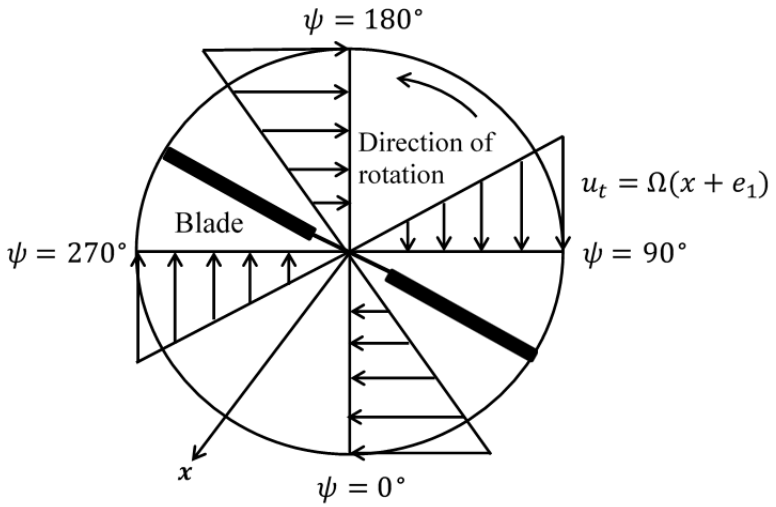

Fig. 4.3. Axisymmetric nature of the in-plane velocity distribution in hovering flight

From Fig. 4.3 in case of the hovering flight, the tangential velocity u_t, parallel to the rotor disk plane varying along the rotor blade length is azimuthally axisymmetric and radially linear with zero flow velocity at the rotational axis. Therefore, in the hovering flight, u_t is independent of the azimuth angle, $\psi(t) = \Omega t$ and is only the function of the radial distance, x from the blade root.

Figure 4.4 shows a typical cross-section of the helicopter rotor blade with all the induced aerodynamic force and moment components where L, D, and M_{ac} indicate the lift, drag, and the pitching moment, respectively, per unit length. All the forces and the moment are acting at the aerodynamic center, A. From Fig. 4.4, L is always perpendicular to the line of action of the relative wind velocity and D acts parallel to that. From aerodynamic theory, L, D, and M_{ac} are all functions of the velocity distributions parallel and perpendicular to the rotor disk. The air velocity seen by the blade has two components u_t and u_p, where u_p is the induced velocity acting perpendicular to the rotor disk plane. For the hovering flight, there is no axial climb

velocity, v_c and therefore, u_p consists of only the induced or inflow velocity at the rotor disk, v_i, also known as the downwash. For hovering flight, v_i is the function of the rotor thrust, the density of the air, and the rotor disk area, and therefore, is independent of x and ψ. For the hovering flight, since the velocity components do not contain periodic terms as in the case of the forward flight, they are expressed as below for any airfoil section:

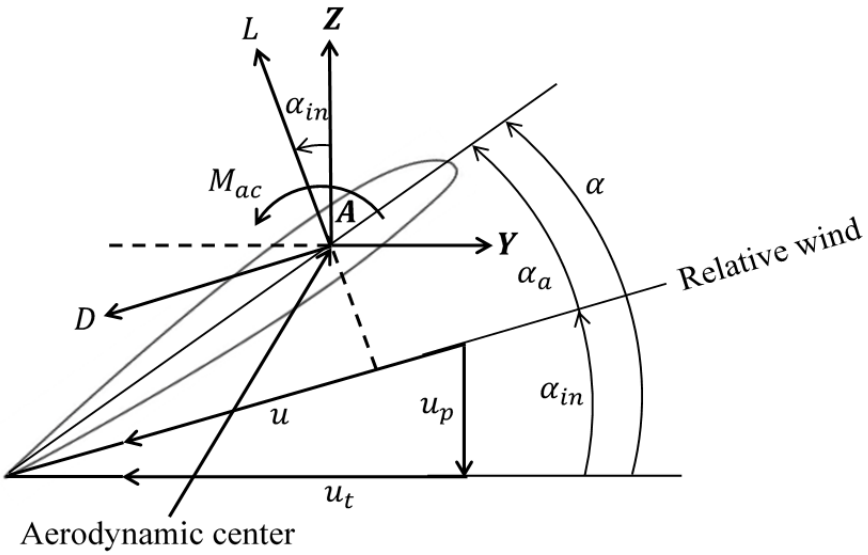

Fig. 4.4. Aerodynamic force and moment components at a typical blade element

$$v_i(x) = v_i = \sqrt{T_h/2\rho_{air}A_d} \tag{4.2}$$

$$u_t(x) = \Omega(x + e_1) \tag{4.3}$$

$$u_p(x) = u_p = v_c + v_i = v_i \tag{4.4}$$

where ρ_{air} is the density of the air, A_d is the rotor disk area.

The resultant velocity magnitude is then given by,

$$u(x) = \sqrt{u_t^2(x) + u_p^2} \approx \sqrt{u_t^2(x)} \approx u_t(x) \tag{4.5}$$

because, compared to u_t, u_p is smaller. The inflow angle, α_{in} and the AoA, α_a are defined as,

$$\alpha_{in}(x) = tan^{-1}\left[\frac{u_p}{u_t(x)}\right] \tag{4.6}$$

$$\alpha_a(x) = \alpha(x) - \alpha_{in}(x) = \alpha_t(x) + \alpha_p - \alpha_{in}(x) \tag{4.7}$$

After setting all the assumptions and $u(x) \approx u_t(x)$, the aerodynamic strip theory gives the aerodynamic lift, drag, and pitching moment per unit length for the hovering flight as below:

$$L(x) = \frac{1}{2}\rho_{air} u_t^2(x) c c_l(x) \tag{4.8}$$

$$D(x) = \frac{1}{2}\rho_{air} u_t^2(x) c c_d(x) \tag{4.9}$$

$$M_{ac}(x) = \frac{1}{2}\rho_{air} u_t^2(x) c^2 c_m(x) \tag{4.10}$$

where c_l, c_d, and c_m are the lift, the drag, and the pitching moment coefficients, respectively.

From Fig. 4.4, the total force and moment components for the hovering flight acting on the airfoil along Y and Z directions through the aerodynamic center A are expressed as,

$$F_Z(x) = L(x)cos\alpha_{in}(x) - D(x)sin\alpha_{in}(x) \tag{4.11}$$

$$F_Y(x) = -L(x)sin\alpha_{in}(x) - D(x)cos\alpha_{in}(x) \tag{4.12}$$

$$M_A(x) = M_{ac}(x) \tag{4.13}$$

where F_Z, F_Y, and M_A are the total out-of-plane bending force, total in-plane bending force, and the pitching moment acting through the aerodynamic center, A, respectively.

4.4 Transformations of the Aerodynamic Forces and Moment

For the Bo 105 helicopter rotor blade, it is assumed that the aerodynamic center coincides with the centroid of the blade cross-section and the elastic axis coincides with the axis of twist (Friedmann and Tong, 1972). Since the aerodynamic forces and moment acting on the airfoil in Fig. 4.4 act through the aerodynamic center, therefore, in this analysis, ultimately, they are considered to act through the centroid. Moreover, according to Friedmann and Tong (1972), the shear center has a chordwise offset from the centroid of the blade cross-section. However, in Chapter 3, Eqs. (3.1)–(3.3) are derived by considering the point of application of the forces and moment through the shear center. Since the aerodynamic center/centroid and the shear center of

the airfoil are not the same, therefore, the forces and the pitching moment in Eqs. (4.8)–(4.10) must be transformed as appropriate to be applicable for the shear center. To do that, the overall force-couple system in Fig. 4.4 is transformed into an equivalent force-couple system from the law of statics demonstrated in Fig. 4.5. Depending on the location of the shear center, fore or aft of the aerodynamic center, the magnitude of the pitching moment will be different. However, the magnitudes of the lift and the drag forces will be the same. Figure 4.5 shows two possible configurations of the locations of the shear center, E with respect to the aerodynamic center, A. Figure 4.5(b) shows the aerodynamic forces and moment acting through A. Figure 4.5(a) explains how the aerodynamic pitching moment combines with the pitching moments coming from F_Y and F_Z, when E is behind A. Similarly, Fig. 4.5(c) describes the combined pitching moment when E is in front of A. M_{FY_E} and M_{FZ_E} indicate the pitching moments acting through E coming from the forces F_Y and F_Z, respectively. Since the change in the pitching moment contributing from drag is very small, it can be concluded that only the pitching moment coming from the lift force effectively influences the overall pitching moment.

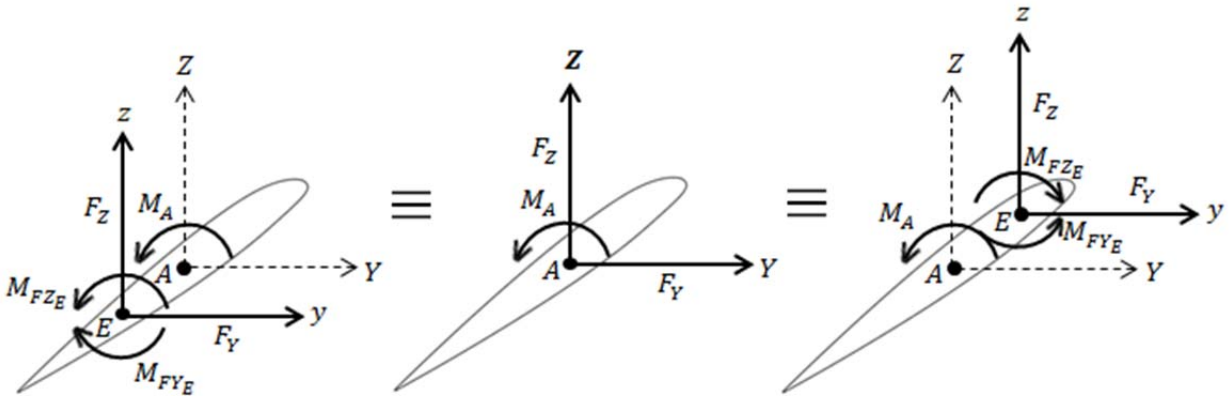

(a) (b) (c)

Fig. 4.5. Transformation of the aerodynamic force from aerodynamic center to shear center (a) the shear center is below the aerodynamic center (b) no shear center is present (c) the shear center is over the aerodynamic center

For Fig. 4.5(a),

$$M_E(x) \cong M_A(x) + M_{FZ_E}(x) = M_{ac}(x) + F_Z(x)AE = M_{ac}(x) + F_Z(x)e \qquad (4.14)$$

For Fig. 4.5(c),

$$M_E(x) \cong M_A(x) - M_{FZ_E}(x) = M_{ac}(x) - F_Z(x)AE = M_{ac}(x) + F_Z(x)e \qquad (4.15)$$

where $e = \mp AE$ and is used with proper sign convention. The sign convention for the any torque is positive when counterclockwise and e is positive if E is behind A.

4.5 Estimation of the Lift, Drag, and Moment Coefficients

Magnitudes of c_l, c_d, and c_m in Eqs. (4.8)–(4.10) depend on the values of α_a and the Mach number in addition to the Reynolds number. In low α_a regime and for subsonic Mach numbers, c_l, c_d, and c_m are expressed as below (Johnson, 1994; Leishman, 2006):

$$c_l = c_0 + c_1\alpha_a \tag{4.16}$$

$$c_d = d_0 + d_1\alpha_a + d_2\alpha_a^2 \tag{4.17}$$

$$c_m = m_0 + m_1\alpha_a \tag{4.18}$$

where c_0, c_1, d_0, d_1, d_2, m_0, and m_1 are empirically derived coefficients obtained through curve fitting to the airfoil measurements.

According to Johnson (1994), c_l can be approximated as below along with α_a:

$$c_l = a\alpha_\alpha(x) \tag{4.19}$$

$$\alpha_a(x) = \alpha(x) - \alpha_{in}(x) = \alpha_t(x) + \alpha_p - \alpha_{in}(x) = \alpha_t(x) + \alpha_{p0} - \alpha_{in}(x) \tag{4.20}$$

where a is the lift curve slope and $\alpha_p = \alpha_{p0}$ for hovering flight, also known as the blade collective pitch angle or collective pitch input exerted by the pilot. As the collective pitch input is given, α_{po} is set equally in the same direction on all rotor blades simultaneously. This action changes the AoA which changes c_l and affects overall lift. A specific value of α_{p0} is required for the helicopter to hover at a specific altitude by overcoming the weight of the helicopter. A linear twist distribution for the Bo 105 helicopter rotor blade can be expressed as below:

$$\alpha_t(x_1) = \frac{\Delta\alpha_t}{R}x_1 + \alpha_{t_{cr}} \tag{4.21}$$

where R is the rotor radius, $\Delta\alpha_t$ is the angle of twist or washout between the center of rotation and the tip of the blade, and $\alpha_{t_{cr}}$ is the pretwist angle that the blade would have if extended into the center of rotation. In Eq. (4.21), α_t is expressed as a function of x_1 instead of x

which is due to the evaluation of the twist from the center of rotation. Therefore, for the sake of consistency, Eq. (4.21) must be expressed in terms of the global x axis which is:

$$\alpha_t(x) = \frac{\Delta\alpha_{t_{tr}}}{l}x + \alpha_{t_{root}} \tag{4.22}$$

where $\Delta\alpha_{t_{tr}} = \alpha_{t_{tip}} - \alpha_{t_{root}}$ with the subscripts $root$ and tip indicating the evaluations of α_t at the blade root and at the blade tip, respectively.

Using Eqs. (4.3), (4.4), (4.6), and (4.22) into Eq. (4.20), the final form of $\alpha_a(x)$ becomes,

$$\alpha_a(x) = \frac{\Delta\alpha_{t_{tr}}}{l}x + \alpha_{t_{root}} + \alpha_{p0} - tan^{-1}\left[\frac{v_i}{\Omega(x+e_1)}\right] \tag{4.23}$$

Bo 105 helicopter uses the NACA 23012 airfoil in the rotor blade for which $a \approx 5.7$/rad from Bailey's expression for a Reynolds number of 2×10^6 (Johnson, 1994). Values of the coefficients d_0, d_1, and d_2 are selected as 0.0087, -0.0121, and 0.4, respectively (Johnson, 1994).

The magnitude of pitching moment with respect to the aerodynamic center is zero for a symmetric airfoil. However, for an asymmetric airfoil, the pitching moment as well as c_m with respect to the aerodynamic center is not zero which largely depends on the type and the shape of the airfoil for a standard range of Reynolds number. To calculate c_m, it is customary to use the data table generated for a particular type of airfoil for different α_a and c_l values. For the NACA 23012 airfoil, the values of c_m are approximately constant for different values of α_a and c_l ranging from $-4°$ to $16°$ and -0.4 to 1.6, respectively, and is approximated as -0.008 for this analysis (Abbott et al., 1945).

4.6 Estimation of the Global Forces and Moment

Finally, the forces and moment for the hovering flight along the global z and y axes and about global x axis are written as:

$$f_z(x) = F_Z(x) \tag{4.24}$$

$$f_y(x) = F_Y(x) \tag{4.25}$$

$$m_x(x) = M_E(x) \tag{4.26}$$

where the expression of $M_E(x)$ can be found either from Eq. (4.14) or (4.15), depending on relative location of the shear center with respect to the aerodynamic center. If α_{in} is small, Eqs. (4.11) and (4.12) can be approximated as,

$$f_z(x) \cong F_Z(x) \cong L(x) \tag{4.27}$$

$$f_y(x) \cong F_Y(x) \cong -L(x)\alpha_{in}(x) - D(x) \cong -L(x)\frac{u_p}{u_t(x)} - D(x) \tag{4.28}$$

For the vibration analysis in the hovering flight, the loads are approximated as,

$$f_z(x,t) = pF_Z(x)sin\omega_e t \tag{4.29}$$

$$f_y(x,t) = pF_Y(x)sin\omega_e t \tag{4.30}$$

$$m_x(x,t) = pM_E(x)sin\omega_e t \tag{4.31}$$

where p indicates a small fraction of the magnitudes of F_Z, F_Y, and M_E and ω_e is the excitation frequency of the vibratory loads. The terms $pF_Z(x)$, $pF_Y(x)$, and $pM_E(x)$ are the magnitudes of the vibratory forces in Eqs. (4.29)–(4.31). For this study, p is considered as 0.1 and ω_e is considered as 12 rad/s.

CHAPTER 5

Dynamics in the Forward Flight

5.1 Forward Flight—A Combination of Collective and Cyclic Controls

In the forward flight, also known as the level flight in absence of the climbing velocity, the asymmetric velocity distribution throughout the rotor disk produces a time-varying blade sectional AoA and thereby creates an uneven lift distribution in the advancing and the retreating sides of the rotor disk. In addition to that, the inflow distribution throughout the rotor disk is not uniform which also varies with time, i.e., in the azimuth domain. In order to ensure a steady, level forward flight, the uneven lift distribution must be corrected. Therefore, in contrast with the hovering flight, the pilot requires some additional controls to apply in the forward flight which in turn depends on the behavior of the time-varying aerodynamic loadings acting on the helicopter rotor blade. Therefore, proper understanding of the characteristics of these time-varying aerodynamic loads is of utmost importance to efficiently direct the helicopter in a steady forward flight. In Chapter 5, the primary objective is to estimate the time-varying aerodynamic loads acting on the Bo 105 helicopter rotor blade at the forward flight to predict the corresponding dynamic response by using the numerical solution technique described in Chapter 7.

5.2 Principle of the Forward Flight

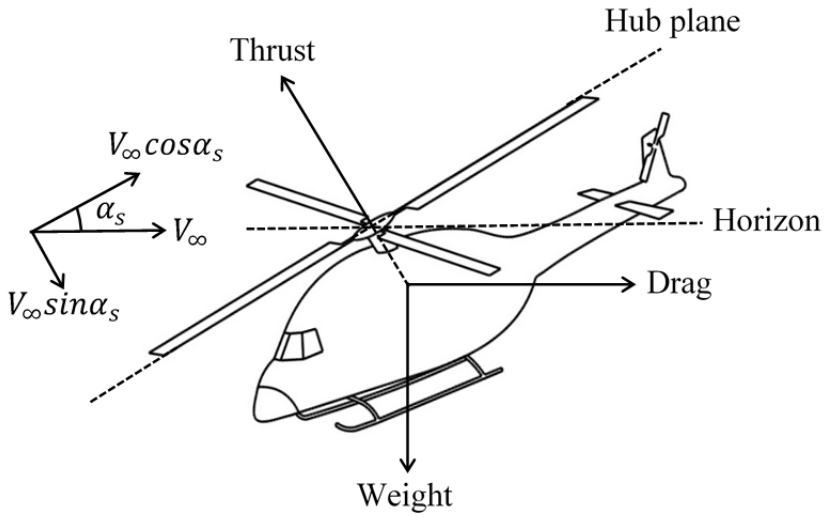

Fig. 5.1. Force balance of a helicopter during forward flight

When the helicopter transits from the hovering flight to the forward flight, the rotor is required to produce both the lifting force to overcome the weight of the helicopter and the propulsive force to propel the helicopter forward at the same time. Therefore, in order to attain the equilibrium of all the forces acting on the helicopter, the rotor disk must be tilted forward at an AoA, α_s relative to the oncoming flow or the horizontal forward speed of the helicopter, V_∞ as shown in Fig. 5.1. $V_\infty cos\alpha_s$ and $V_\infty sin\alpha_s$ are the velocity components parallel and perpendicular to the rotor disk, respectively. The thrust is acting normal to the hub plane, the vertical and horizontal components of which balance the weight of the helicopter and the parasitic drag, respectively. To define the aerodynamic forces and moment in the forward flight, at first it is necessary to identify the unique features below that characterize the forward flight from the hovering flight:

1. There exists a dissymmetry of lift or in-plane velocity distribution over the rotor disk depicted in Fig. 5.2 which needs to be corrected for a stable flight.

2. To correct the dissymmetry of lift, the cyclic control needs to be applied by the pilot in addition to the collective control thereby allowing the helicopter rotor blade to flap and pitch at the same time.

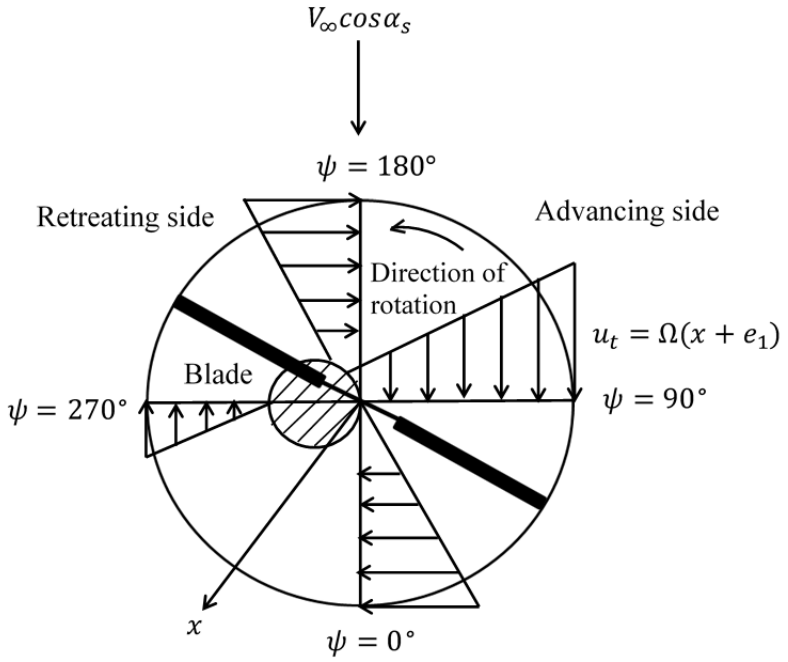

Fig. 5.2. Dissymmetry of the in-plane velocity distribution for the forward flight

In forward flight, the aerodynamic environment varies periodically as the blade goes around the azimuth and experiences a periodically varying relative air velocity due to the forward speed as well as its angular motion. This is because, a component of the forward speed is either added to or subtracted from the blade linear velocity at each section as shown in Fig. 5.2 thus creating an asymmetric and periodic velocity distribution around the azimuth in one complete rotor revolution. The advancing blade has a higher velocity relative to the air than the rotational velocity, while the retreating blade has a lower velocity relative to the air. Since the lift is proportional to the square of the in-plane linear blade velocity, if a constant AoA is assumed, distribution of the lift is uneven on the two halves of the rotor disk with the advancing side producing more lift than the retreating side. This phenomenon is known as the dissymmetry of lift that tends to roll the helicopter toward the retreating side and therefore, must be corrected.

To compensate for the dissymmetry of lift, the AoA on the advancing side of the blade needs to be reduced which on the contrary, requires to be increased on the retreating side of the blade. This mechanism is inherent in the flapping action of a hinged blade which is the primary means of compensating for the dissymmetry of lift. However, the Bo105 has a hingeless/rigid rotor system for which no physical vertical or horizontal hinges are present. Instead of that, there exists an apparent cantilevered root with a specially designed elastic rotor blade which is strong and flexible enough to withstand the aerodynamic load. These blades themselves can flex to provide elastic flapping motion as part of correcting the dissymmetry of lift instead of providing direct flapping or lead-lag motion as is the case with a hinged rotor. It occurs in response to changes in lift due to changing velocity or cyclic feathering which in combination with blade flapping maintains the symmetry of lift over the rotor disk.

In order to counter act the dissymmetry of lift in the forward flight, the pilot has to apply the cyclic control to individual rotor blades in addition to the collective control applied to all rotor blades equally at once. Both the control inputs change the pitch angle which in turn changes the AoA, thereby changing the overall lift. Similar to the hovering flight, the collective pitch input sets α_{p0} equally and simultaneously for all the blades. Then, the cyclic pitch input controls the pitch differentially around the rotor system thereby creating a differential lift by finely adjusting the AoA so that the total lift generated over the rotor disk is balanced. This involves increasing the AoA of the retreating blades and decreasing that of the advancing blades.

As the forward speed increases, the pitch angles on the advancing and the retreating blades continue to further decrease and increase, respectively, and at the same time, the rotor disk is tilted more and more toward the forward direction.

Unlike hover, in forward flight, the rotor blades experience once per revolution (l/rev) variation in the aerodynamic loads due to the asymmetry in the airflow, or, in other words, the blade airloads are periodic with a fundamental frequency equal to the rotor angular speed, Ω. In response to this variation in the load, there is also 1/rev dynamic response of the blade in terms of flapping, lead-lag, and torsional motions. It means, both the blade load and the blade response undergo a periodic variation in one rotor revolution around the azimuth with period $\psi = 2\pi$. Therefore, the cyclic control must be applied in accordance with the same periodic variation in one rotor revolution. Once applied, it is repeated in the same way for each rotor revolution and hence, is termed as the cyclic control.

While traveling forward, if the speed of the helicopter continues to increase, it eventually reaches a point where the AoA of the retreating rotor blade is too high to generate the lift, i.e., high enough to reach above the stall angle and consequently, the retreating blade stalls. This retreating blade stall can be avoided by not exceeding the never-exceed speed of the helicopter, V_{NE}.

5.3 Estimation of the Blade Loadings at Forward Flight—The Aerodynamic Strip Theory

In Chapter 4, the aerodynamic strip theory and the relevant assumptions are already discussed to define the airloads in the hovering flight. In this section, the same strip theory is applied for the forward flight to express the aerodynamic forces and moment in terms of the periodic velocity components u_p and u_t. Despite having similar expressions like the hovering flight, they may contain additional terms which upon inclusion in Eqs. (3.1)–(3.3) result in nonlinear governing differential equations (GDEs) and will be discussed in the later sections.

5.3.1 The Periodic Velocity Components with Large Angle Deflections

In forward flight, u_p and u_t are functions of both x and t (or ψ) which contain periodic terms with period 2π and frequency equal to Ω. To estimate the comprehensive expression of the in-plane velocity u_t, Fig. 5.2 describes that in addition to the in-plane velocity $\Omega(x + e_1)$, a

component of the in-plane velocity $V_\infty cos\alpha_s$ is added to or subtracted from $\Omega(x + e_1)$ to create an asymmetric velocity distribution in the azimuth domain at each section of the blade. At the same time, another part of u_t can be contributed to the perturbation in the velocity $\dot{v}$ generated from the lead-lag motion of the blade. Similarly, the out-of-plane velocity u_p consists of several parts among which some also contain periodic terms. One such term is the perturbation in velocity $\dot{w}$ produced as a result of the flapping motion of the blade about the root as showed in Fig. 5.3. Here, β_f represents the flapping angle that the deformed blade makes with the hub plane which is the function of both x and t. In previous research studies, β_f was considered small to express u_p, which is not the case in reality. Therefore, another term contributes to u_p from the perturbation in $V_\infty cos\alpha_s cos(\Omega t) sin\,\beta_f$ because of the blade flapping displacement. Lastly, the total inflow $V_\infty sin\alpha_s + v_i$, perpendicular to the hub plane also has the component acting perpendicular to the deformed blade expressed as $(V_\infty sin\alpha_s + v_i)cos\beta_f$. Considering the overall physics described above, for a level (horizontal) forward flight with $v_c = 0$, the periodic velocity components of a flexible helicopter rotor blade are explicitly written below for the large angle β_f as:

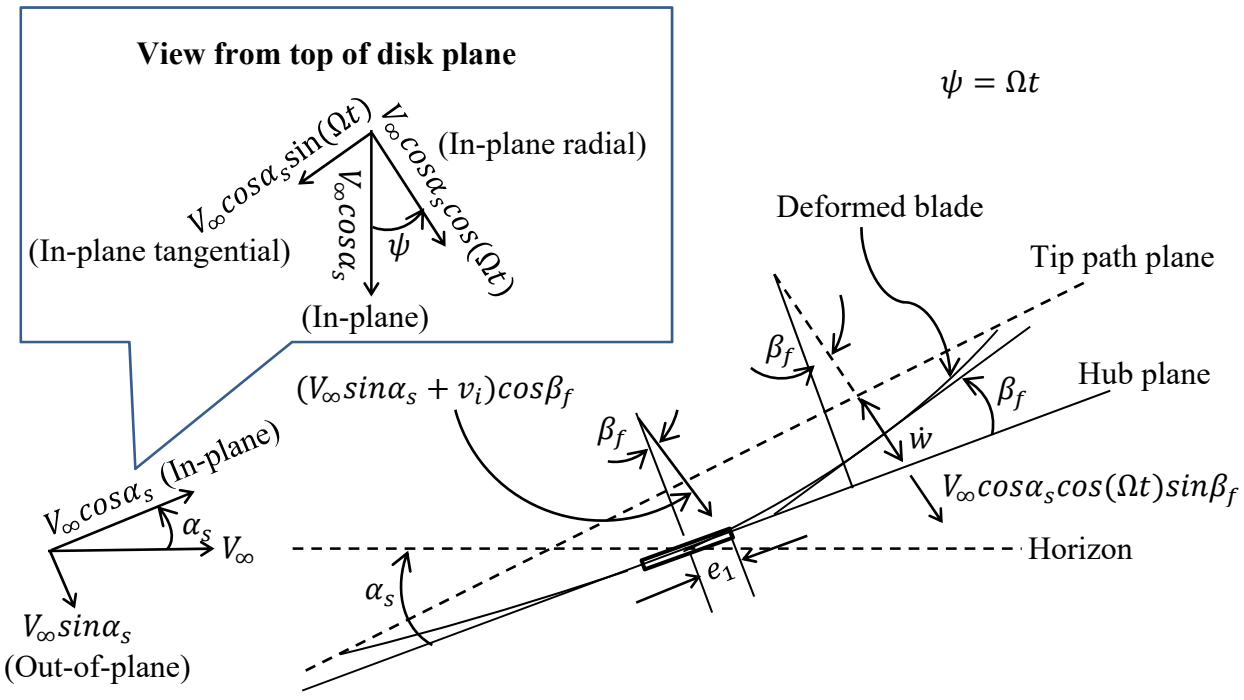

Fig. 5.3. Perturbation velocities on the blade resulting from blade flapping in forward flight

$$u_t(x,t) = \Omega(x + e_1) + \dot{v}(x,t) + V_\infty cos\alpha_s sin(\Omega t) \tag{5.1}$$

$$u_p(x,t) = (V_\infty sin\alpha_s + v_i)cos\,\beta_f(x,t) + \dot{w}(x,t) + V_\infty cos\alpha_s cos(\Omega t) sin\,\beta_f(x,t) \tag{5.2}$$

From Eqs. (5.1) and (5.2), both u_p and u_t are expressed in terms of the independent variables, x and t which can be directly used to formulate f_z, f_y, and m_x to be used in Eqs. (3.1)–(3.3). However, instead of t, it is customary in helicopter dynamics to express all the relevant components of the GDEs in terms of the independent variable ψ, also known as the nondimensional time. This is due to the periodic nature the loading and the consequent response of the blade followed by the corresponding repetition after each rotor revolution which makes it more convenient to replace t with ψ. Since $\psi = \Omega t$, therefore, the transformation between t and ψ can be performed as below:

$$\dot{w} = \frac{\partial w}{\partial t} = \Omega \frac{\partial w}{\partial \psi} = \Omega \overset{*}{w} \tag{5.3}$$

$$\dot{v} = \frac{\partial v}{\partial t} = \Omega \frac{\partial v}{\partial \psi} = \Omega \overset{*}{v} \tag{5.4}$$

$$\ddot{w} = \frac{\partial^2 w}{\partial t^2} = \Omega^2 \frac{\partial^2 w}{\partial \psi^2} = \Omega^2 \overset{**}{w} \tag{5.5}$$

$$\ddot{v} = \frac{\partial^2 v}{\partial t^2} = \Omega^2 \frac{\partial^2 v}{\partial \psi^2} = \Omega^2 \overset{**}{v} \tag{5.6}$$

$$\dot{\theta} = \frac{\partial \theta}{\partial t} = \Omega \frac{\partial \theta}{\partial \psi} = \Omega \overset{*}{\theta} \tag{5.7}$$

where $(^*) = \frac{\partial}{\partial \psi}(\,)$ and $(^{**}) = \frac{\partial^2}{\partial \psi^2}$. These notations will be used from now onwards to express the derivatives with respect to ψ. Using Eqs. (5.3) and (5.4) into Eqs. (5.1) and (5.2), u_p and u_t are expressed as functions of x and ψ as below:

$$u_t(x,\psi) = \Omega(x + e_1) + \Omega \overset{*}{v}(x,\psi) + V_\infty cos\alpha_s sin\psi \tag{5.8}$$

$$u_p(x,\psi) = (V_\infty sin\alpha_s + v_i)cos\beta_f(x,\psi) + \Omega \overset{*}{w}(x,\psi) + V_\infty cos\alpha_s cos\psi sin\beta_f(x,\psi) \tag{5.9}$$

Equations (5.8) and (5.9) can be written more conveniently in terms of two nondimensional parameters, the advance ratio, μ and the total rotor inflow ratio, λ defined as:

$$\mu = \frac{V_\infty cos\alpha_s}{\Omega R} \tag{5.10}$$

$$\lambda = \frac{V_\infty sin\alpha_s + v_i}{\Omega R} = \frac{V_\infty sin\alpha_s}{\Omega R} + \frac{v_i}{\Omega R} = \mu tan\alpha_s + \lambda_i \tag{5.11}$$

where R is the rotor radius, λ_i is rotor induced inflow ratio, and ΩR is the tip velocity of the rotor blade. Using Eqs. (5.10) and (5.11) into Eqs. (5.8) and (5.9), the velocity components are rewritten as:

$$u_t(x,\psi) = \Omega(x + e_1) + \Omega\overset{*}{v}(x,\psi) + \mu\Omega R sin\psi \tag{5.12}$$

$$u_p(x,\psi) = \lambda\Omega R cos\beta_f(x,\psi) + \Omega\overset{*}{w}(x,\psi) + \mu\Omega R cos\psi sin\beta_f(x,\psi) \tag{5.13}$$

5.3.2 Rotor Inflow Distribution: Drees's Nonuniform Inflow Model

The parameters that influence λ depend on the type of the inflow model to be used in the expression of u_p. In quest of a suitable inflow model, researchers found that the inherent nature of the inflow distribution was complicated visualized from the conducted experiments. During the transition from hover into level forward flight, i.e., $0 \leq \mu \leq 0.1$, the induced velocity in the plane of the rotor is the most nonuniform because of the strong effects of the discrete tip vortices that sweep downstream near the rotor plane. However, in high-speed forward flight for which $\mu \geq 0.15$, the time-averaged longitudinal inflow becomes more linear and can be approximately represented by the model suggested by Glauert (1926). This model simulated a longitudinal variation of the induced velocity with an upwash at the leading edge and an increase in the induced velocity at the trailing edge of the rotor disk. Later, other researchers refined that theory by considering both longitudinal and lateral variations in the inflow which can be written in a general form of a nonuniform flow for the steady, level forward flight as:

$$\lambda_i = \lambda_i(x,\psi) = \lambda_0\left(1 + k_x\frac{x + e_1}{R}cos\psi + k_y\frac{x + e_1}{R}sin\psi\right) \tag{5.14}$$

where λ_0 is the mean induced inflow ratio at the center of the rotor given by the momentum theory (Leishman, 2006) and k_x and k_y are the weighting factors that represent the deviation of the inflow from the uniform value predicted by the simple momentum theory

(Leishman, 2006). Equation (5.14) expresses the variation of the induced inflow as functions of both spatial and azimuthal locations on the rotor disk. If C_T is the thrust coefficient, then for uniform inflow:

$$\lambda_0 = \frac{C_T}{2\sqrt{\mu^2 + \lambda_0^2}} \tag{5.15}$$

For a given C_T, Eq. (5.15) can be solved for λ_0 by the Newton-Raphson method. To estimate the values of the weighting factors, different inflow models can be consulted among which Drees's model (Leishman, 2006; Ramanujam et al., 2015) is one of the most popular models because it is easy to implement and gives reasonably good description of the rotor inflow. Therefore, in this analysis, Drees's approximations (Leishman, 2006; Ramanujam et al., 2015) are considered to estimate k_x and k_y which take the following forms:

$$k_x = \frac{4}{3}\left[(1 - 1.8\mu^2)\sqrt{1 + \left(\frac{\lambda}{\mu}\right)^2} - \frac{\lambda}{\mu}\right] \tag{5.16}$$

$$k_y = -2\mu \tag{5.17}$$

The terms $cos\beta_f$ and $sin\beta_f$ in Eq. (5.13) can be expressed as,

$$cos\beta_f = \frac{1}{sec\beta_f} = \frac{1}{\sqrt{1 + tan^2\,\beta_f}} = \frac{1}{\sqrt{1 + (w')^2}} \tag{5.18}$$

$$sin\beta_f = \frac{1}{cosec\beta_f} = \frac{1}{\sqrt{1 + cot^2\,\beta_f}} = \frac{tan\,\beta_f}{\sqrt{1 + tan^2\,\beta_f}} = \frac{w'}{\sqrt{1 + (w')^2}} \tag{5.19}$$

where $w' = w'(x, \psi)$. Using Eqs. (5.18) and (5.19) into Eq. (5.13), the final form of $u_p(x, \psi)$ becomes,

$$u_p(x, \psi) = \frac{\lambda(x, \psi)\Omega R}{\sqrt{1 + [w'(x, \psi)]^2}} + \Omega\overset{*}{w}(x, \psi) + \frac{w'(x, \psi)\mu\Omega R cos\psi}{\sqrt{1 + [w'(x, \psi)]^2}} \tag{5.20}$$

5.3.3 Aerodynamic Lift, Drag, and Pitching Moment in Forward Flight

The aerodynamic forces and moment acting on the airfoil per unit length for the forward flight are similar to that of the hovering flight with respect to Fig. 4.4 in Chapter 4 given by Eqs.

(4.8)–(4.10). Assuming $u \approx u_t$ from Chapter 4, the strip theory gives the aerodynamic lift, drag, and pitching moment per unit length for the forward flight as below:

$$L(x,\psi) = \frac{1}{2}\rho_{air} u_t^2(x,\psi) c c_l(x,\psi) \tag{5.21}$$

$$D(x,\psi) = \frac{1}{2}\rho_{air} u_t^2(x,\psi) c c_d(x,\psi) \tag{5.22}$$

$$M_{ac}(x,\psi) = \frac{1}{2}\rho_{air} u_t^2(x,\psi) c^2 c_m(x,\psi) \tag{5.23}$$

c_l, c_d, and c_m in addition to u_t are functions of both x and ψ in Eqs. (5.21)–(5.23), which are unlike for the hovering flight. Since for the forward flight, $u_p = u_p(x,\psi)$ and $u_t = u_t(x,\psi)$, Eq. (4.6) in Chapter 4 can be updated as:

$$\alpha_{in}(x,\psi) = tan^{-1}\left[\frac{u_p(x,\psi)}{u_t(x,\psi)}\right] \tag{5.24}$$

From Fig. 4.4 with reference to Eq. (5.24), the total force and moment components for the forward flight acting on the airfoil along Y and Z directions through the aerodynamic center A are expressed as,

$$F_Z(x,\psi) = L(x,\psi) cos\alpha_{in}(x,\psi) - D(x,\psi) sin\alpha_{in}(x,\psi) \tag{5.25}$$

$$F_Y(x,\psi) = -L(x,\psi) sin\alpha_{in}(x,\psi) - D(x,\psi) cos\alpha_{in}(x,\psi) \tag{5.26}$$

$$M_A(x,\psi) = M_{ac}(x,\psi) \tag{5.27}$$

5.4 Transformations of the Aerodynamic Forces and Moment

The transformation of the aerodynamic forces and moment are similar as described in Section 4.4 and with respect to Fig. 4.5 and the corresponding versions of Eqs. (4.14) and (4.15) as functions of x and ψ are given below:

For Fig. 4.5(a)

$$M_E(x,\psi) = M_{ac}(x,\psi) + F_Z(x,\psi) AE = M_{ac}(x,\psi) + F_Z(x,\psi) e \tag{5.28}$$

For Fig. 4.5(c),

$$M_E(x,\psi) = M_{ac}(x,\psi) - F_Z(x,\psi)AE = M_{ac}(x,\psi) + F_Z(x,\psi)e \tag{5.29}$$

where $e = \mp AE$ used with proper sign convention discussed in Section 4.4.

5.5 Estimation of the Lift, Drag, and Moment Coefficients

Equations (4.19) and (4.20) can be rewritten for the forward flight in the following forms,

$$c_l(x,\psi) = a\alpha_a(x,\psi) \tag{5.30}$$

$$\begin{aligned}\alpha_a(x,\psi) &= \alpha(x,\psi) - \alpha_{in}(x,\psi) = \alpha_t(x) + \alpha_p(\psi) + \theta(x,\psi) - \alpha_{in}(x,\psi) \\ &= \alpha_t(x) + \alpha_{p0} + \alpha_{1c}cos\psi + \alpha_{1s}sin\psi + \theta(x,\psi) - \alpha_{in}(x,\psi)\end{aligned} \tag{5.31}$$

where $\alpha_p = \alpha_{p0} + \alpha_{1c}cos\psi + \alpha_{1s}sin\psi$ for the forward flight with α_{p0} as the collective pitch angle and α_{1c} and α_{1s} are the lateral cyclic pitch and longitudinal cyclic pitch, respectively. The proper values of α_{p0}, α_{1c}, and α_{1s} can be found by consulting the rotor propulsive trim data (Goulos et al., 2015; Ramanujam, 2015). The value of a can be approximated as 5.7/rad mentioned in Section 4.5.

By using Eqs. (4.22), (5.12), (5.20), and (5.24) into Eq. (5.31), the final form of α_a becomes:

$$\begin{aligned}\alpha_a(x,\psi) = {} & \frac{\Delta\alpha_t}{l}x + \alpha_{t_{root}} + \alpha_{p0} + \alpha_{1c}cos\psi + \alpha_{1s}sin\psi + \theta(x,\psi) \\ & - tan^{-1}\left[\frac{\dfrac{\lambda(x,\psi)\Omega R}{\sqrt{1+[w'(x,\psi)]^2}} + \Omega\overset{*}{w}(x,\psi) + \dfrac{w'(x,\psi)\mu\Omega R cos\psi}{\sqrt{1+[w'(x,\psi)]^2}}}{\Omega(x+e_1) + \Omega\overset{*}{v}(x,\psi) + \mu\Omega R sin\psi}\right]\end{aligned} \tag{5.32}$$

For the forward flight of Bo 105 helicopter, c_d and c_m are expressed as below (Wang et al., 1988):

$$c_d(x,\psi) = 0.0079 + 1.7\alpha_a^2(x,\psi) \tag{5.33}$$

$$c_m = -0.012 \tag{5.34}$$

5.6 Estimation of the Global Force and Moment

Finally, the lift, the drag, and the pitching moment in the forward flight along/about the global axes are written as:

$$f_z(x,t) = f_z(x,\psi) = F_Z(x,\psi) \tag{5.35}$$

$$f_y(x,t) = f_y(x,\psi) = F_Y(x,\psi) \tag{5.36}$$

$$m_x(x,t) = m_x(x,\psi) = M_E(x,\psi) \tag{5.37}$$

where the expression of $M_E(x,\psi)$ can be found either from Eq. (5.28) or (5.29), depending on the relative location of the shear center with respect to the aerodynamic center.

One of the physically meaningful reference planes for a hingeless helicopter rotor is the hub plane. Since the Bo 105 helicopter is the example of a hingeless rotor system, therefore, for the forward flight, all the aerodynamic forces and moment are evaluated here with reference to the hub plane. Consequently, the corresponding forced response of the helicopter rotor blade due to the aerodynamic loading is also measured from the hub plane.

CHAPTER 6

Effects of the Unsteady Motion

6.1 Complete Aerodynamic Loading Including the Unsteady Airfoil Motion

The aerodynamic forces and moment considered in Chapters 4 and 5 are the steady lift, drag, and the pitching moment components. It was intended to derive the air loads per unit span in a general form. However, the presence of the cyclic pitch, the collective pitch, and the time-dependent motion of the airfoil would require a formal splitting of the aerodynamic loading on the airfoil into distinct groups and the two-dimensional unsteady aerodynamic effects are needed to be considered for the completion of the total aerodynamic loadings acting on the airfoil. In this chapter, to clarify the various assumptions associated with the steady-state response of the helicopter rotor blade, the apparent mass effects are neglected and the corresponding formulations for the two-dimensional unsteady aerodynamics of the airfoil are represented.

6.2 Unsteady Aerodynamics: Mathematical Formulation

For the unsteady motion of a two-dimensional airfoil, determined by a general time-dependent pitch angle β_g, a downward displacement h_p of the elastic axis, and a general velocity parallel to the rotor disk plane V_g as shown in Fig. 6.1, the unsteady force and moment per unit span of the helicopter rotor blade with Theodorsen's lift deficiency function, $C(k) = 1$ can be written as (Friedmann and Tong, 1972):

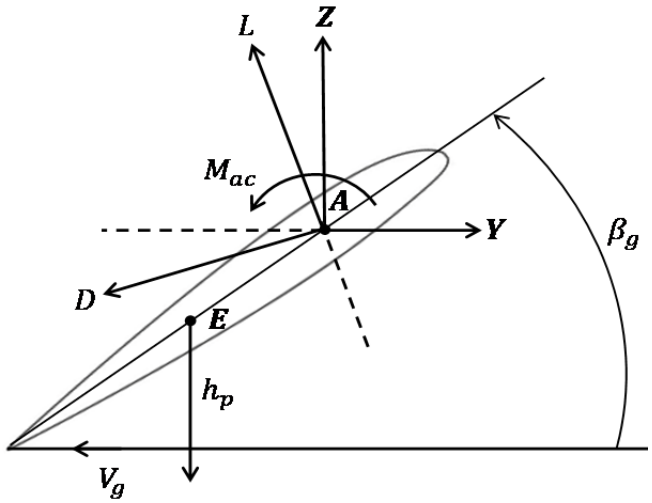

Fig. 6.1. Airfoil with unsteady motion

$$L = L_s + \frac{1}{2}\rho_{air} a \left(\frac{c}{2}\right)^2 \left[\ddot{h} + V_g \dot{\beta}_g - \left(e - \frac{c}{4}\right)\ddot{\beta}_g\right] \tag{6.1}$$

where L_s is the steady lift term defined as,

$$L_s = \frac{1}{2}\rho_{air} acV_g \left[V_g \beta_g + \dot{h} + \left(\frac{c}{2} - e\right)\dot{\beta}_g\right] \tag{6.2}$$

with V_g as the general velocity parallel to the rotor disk plane and

$$\begin{aligned} M_{ac} = M = L_s e + \frac{1}{2}\rho_{air} a \left(\frac{c}{2}\right)^3 \left(e - \frac{c}{4}\right)\left[\ddot{h} - \left(e - \frac{c}{4}\right)\ddot{\beta}_g\right] \\ -\frac{1}{2}\rho_{air} a V_g \dot{\beta}_g \left(\frac{c}{2} - e\right)\left(\frac{c}{2}\right)^2 - \frac{1}{16}\rho_{air} a \left(\frac{c}{2}\right)^4 \ddot{\beta}_g \end{aligned} \tag{6.3}$$

Equations (6.1)–(6.3) assume that the aerodynamic center is located at a distance of $c/4$ from the leading edge. Neglecting the apparent mass terms associated with h and β_g in Eqs. (6.1)–(6.3) yields,

$$L = \frac{1}{2}\rho_{air} acV_g \left[V_g \beta_g + \dot{h} + \left(\frac{3c}{4} - e\right)\dot{\beta}_g\right] \tag{6.4}$$

$$M = \frac{1}{2}\rho_{air} acV_g e\left(V_g \beta_g + \dot{h}\right) + \rho_{air} a V_g \left(\frac{c}{2}\right)^2 \left(\frac{c}{2} - e\right)\left(\frac{2e}{c} - \frac{1}{2}\right)\dot{\beta}_g \tag{6.5}$$

Using the small angle assumption and replacing $\dot{h}$ with $-u_p$, V_g with u_t, and β_g with α and converting $\dot{\alpha}$ from the time domain to the azimuth domain similar to Eqs. (5.3)–(5.7), Eqs. (6.4) and (6.5) are expressed as,

$$L(x,\psi) = \frac{1}{2}\rho_{air} u_t^2(x,\psi) c c_l(x,\psi) + \frac{1}{2}\rho_{air} acu_t(x,\psi)\left(\frac{3c}{4} - e\right)\Omega\dot{\alpha}^*(x,\psi) \tag{6.6}$$

$$\begin{aligned} M(x,\psi) = \tfrac{1}{2}\rho_{air} u_t^2(x,\psi) c c_l(x,\psi) e \\ +\rho_{air} a u_t(x,\psi)\left(\frac{c}{2}\right)^2 \left(\frac{c}{2} - e\right)\left(\frac{2e}{c} - \frac{1}{2}\right)\Omega\dot{\alpha}^*(x,\psi) \end{aligned} \tag{6.7}$$

with $c_l(x,\psi) = a\alpha_a(x,\psi)$ as mentioned by Eq. (5.30) for forward flight and from Eq. (5.31),

$$\overset{*}{\alpha}(x,\psi) = -\alpha_{1c}sin\psi + \alpha_{1s}cos\psi + \overset{*}{\theta}(x,\psi) \tag{6.8}$$

Using the small angle assumption, similar to Eqs. (4.27) and (4.28), the global aerodynamic forces and moment can be written as,

$$f_z(x,\psi) \cong F_z(x,\psi) \cong L(x,\psi) \tag{6.9}$$

$$\begin{aligned} f_y(x,\psi) \cong F_Y(x,\psi) &\cong -L(x,\psi)\alpha_{in}(x,\psi) - D(x,\psi) \\ &\cong -L(x,\psi)\frac{u_p(x,\psi)}{u_t(x,\psi)} - D(x,\psi) \end{aligned} \tag{6.10}$$

$$m_x(x,\psi) = M(x,\psi) \tag{6.11}$$

with $D(x,\psi)$ as expressed by Eqs. (5.22) and (5.33).

CHAPTER 7

Numerical Solution: Generalization of the Method of Lines

7.1 Numerical Solution: An Essential Tool for Solving Realistic Engineering Problems

In Chapter 3, the free vibration analysis of the triply coupled beam/helicopter rotor blade is taken care of by the modified Galerkin method, where the in-plane or lead-lag vibration was thought to be decoupled from the out-of-plane bending and torsional vibrations without much loss of accuracy. However, if the coupling among the out-of-plane bending, torsion, and the in-plane bending is significant for a general triply coupled beam vibration problem, then higher solution accuracy is desired. In case of strongly coupled nonlinear GDEs, the analytical solution approach might not be always viable for which a robust numerical solution technique is an alternative option. Majority of the realistic problems, after necessary mathematical modeling, appear in such forms which are not solvable theoretically and in those cases, numerical solution is the only approach. Nowadays, the promising scope of application of the numerical method has made it a highly demanding mathematical tool for engineers.

The GDEs (3.1)–(3.3) for the 1-D, forced response of a flexible helicopter rotor blade for the forward flight with strongly coupled multiple DOFs are nonlinear upon inclusion of the aerodynamic loadings described in Chapter 5. Compared to the hovering flight, the context of the dynamic characteristics of the forward flight is totally different due to the presence of the periodic forcing functions with large flapping and inflow angles, unsteady aerodynamics, torsional deformations in the pitch angle calculation, rotor inflow, and high advance ratio. Therefore, the development of a robust numerical solution for the general forced response of the flexible helicopter rotor blade is always urged, the implementation of which is the primary focus of Chapter 7.

7.2 The Method of Lines: A Robust Mathematical Tool

The MOL is a numerical procedure for solving the IBVPs in which the space derivatives are approximated algebraically by finite differences to reduce the IBVP into a set of ODEs in time. However, in literature, application of the MOL is mostly limited to simple or lower order linear GDEs with only one DOF. Therefore, the primary focus of Chapter 7 is to develop a

generalized algorithm of the MOL for the 1-D, axially loaded, coupled, forced response of the beam having multiple DOFs which is applicable to any IBVP including linear/nonlinear force with classical/moving BCs. Once the algorithm is developed, the generalized MOL is successfully applied for the solution of the linear/nonlinear GDEs in Chapter 3 with multiple DOFs. For 1-D case, the MOL is proved superior to other available numerical techniques in terms of the convergence rate and the accuracy of solutions.

7.3 Overview of the Method of Lines

The MOL is the general numerical method to convert the IBVP into an initial value problem by the use of the discretization in space, thereby reducing into a system of ODEs. The benefit of the MOL over the existing numerical methods is that the MOL is much simpler compared to the explicit methods and has more stability advantage over the implicit schemes provided an efficient numerical algorithm is used to solve the resulting system of ODEs. The system of ODEs is generally stiff (Bouhamidi and Jbilou, 2013; D'Ambrosio et al., 2017; Dekker, 2009; Izzo, 2017) and need to be solved by an efficient solution algorithm, e.g., 4th order Runge-Kutta (RK) method (Chapra and Canale, 2015; Izzo, 2017; Kalogiratou et al., 2014) which can be easily implemented in MATLAB (MathWorks Corporation, 2015).

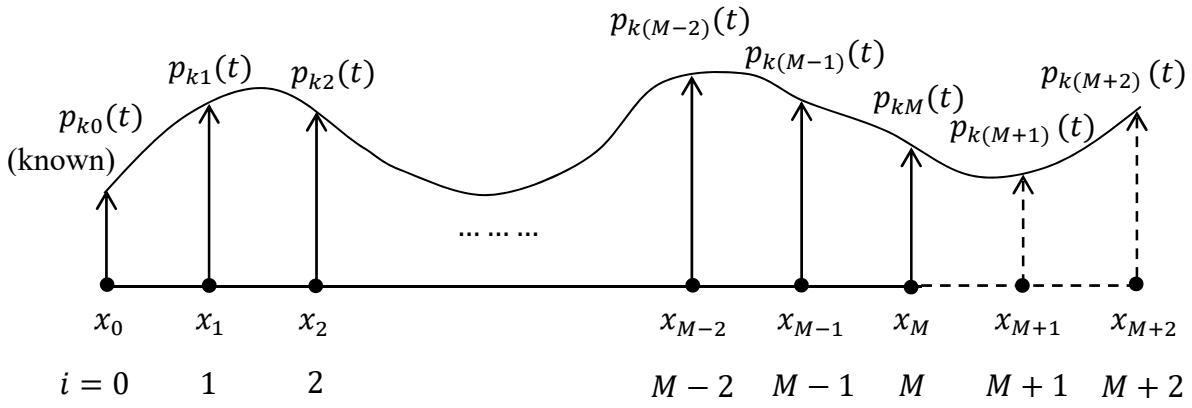

Fig. 7.1. The discretized spatial domain with the dependent variable, $p_k(t)$

Figure 7.1 describes the x domain discretized by M (M is even) uniformly spaced grid points defined by $x_i = x_{i-1} + h$, $x_0 = 0$, and $x_M = l$ with $i = 1,2, \dots M$ where the segment length, $h = l/M$ and $x_i = ih$. A second-order central finite difference approximation (Chapra and Canale, 2015) can be used to discretize the spatial derivative of any dependent variable or DOF p_k ($k = 1,2, \dots N$) at any point, i as:

$$[p_k']_i = p_{ki}' = [(p_k)_{i+1} - (p_k)_{i-1}]/(2h) \tag{7.1}$$

$$[p_k'']_i = p_{ki}'' = [(p_k)_{i+1} - 2(p_k)_i + (p_k)_{i-1}]/(h^2) \tag{7.2}$$

$$[p_k''']_i = p_{ki}''' = [(p_k)_{i+2} - 2(p_k)_{i+1} + 2(p_k)_{i-1} - (p_k)_{i-2}]/(2h^3) \tag{7.3}$$

$$[p_k'''']_i = p_{ki}'''' = [(p_k)_{i+2} - 4(p_k)_{i+1} + 6(p_k) - 4(p_k)_{i-1} + (p_k)_{i-2}]/(h^4) \tag{7.4}$$

where $[\ ]_i$ indicates evaluation of the derivatives at $i = 1,2, \dots M$. The generalized MOL applies to beams with various types of BCs, e.g., fixed-free (cantilever), pinned-pinned, or fixed-pinned end conditions. In either case, the value of the deflection, at least on one boundary is known. Therefore, only two imaginary points x_{M+1} and x_{M+2} beyond the other boundary characterize the imaginary deflections $p_{k(M+1)}$ and $p_{k(M+2)}$ after discretizing the third and the fourth spatial derivatives in Eqs. (7.3) and (7.4) at $i = M$ and are taken care of by the natural BCs.

7.4 Implementation of the Method of Lines: Decoupling of the Governing Equations

To apply the generalized MOL, at first, the coupled GDEs need to be decoupled such that the highest order time derivative of each dependent variable is explicitly expressed as the function $G_k(k = 1,2, \dots N)$ of all the other variables provided each function does not contain any highest order time derivative of any dependent variable. To visualize this, Eq. (3.1) for a single DOF, $w(x,t)$ discretized at point i can be written below:

$$\begin{aligned}\left\{\left[D_{by}(x)w''(x,t)\right]''\right\}_i - \{[T(x)w'(x,t)]'\}_i + m\ddot{w}_i - f_z(x_i,t) = 0 \\ = F(t, \ddot{w}_i, \dot{w}_i, w_1, w_2, \dots w_i)\end{aligned} \tag{7.5}$$

where the term $\ddot{w}_i$ in the function F will be expressed separately after the decoupling process. Equation (7.5) is written for only one dependent variable or DOF, w, however, in the most general case, there might be more than one DOF coupled with one another. Therefore, Eq. (7.5) can be generalized for N DOFs $p_1, p_2, \dots p_N$ as below:

$$\begin{aligned}F_1 = (t, \ddot{p}_{1i}, \ddot{p}_{2i}, \dots \ddot{p}_{Ni}, \dot{p}_{1i}, \dot{p}_{2i}, \dots \dot{p}_{Ni}, p_{11}, p_{12}, \dots p_{1i}, p_{21}, p_{22}, \dots p_{2i}, \dots \\ p_{N1}, p_{N2}, \dots p_{Ni}) = 0\end{aligned}$$

$$F_2 = (t, \ddot{p}_{1i}, \ddot{p}_{2i}, \dots \ddot{p}_{Ni}, \dot{p}_{1i}, \dot{p}_{2i}, \dots \dot{p}_{Ni}, p_{11}, p_{12}, \dots p_{1i}, p_{21}, p_{22}, \dots p_{2i}, \dots p_{N1}, p_{N2}, \dots p_{Ni}) = 0$$

$$\dots \dots \dots$$

$$F_N = (t, \ddot{p}_{1i}, \ddot{p}_{2i}, \dots \ddot{p}_{Ni}, \dot{p}_{1i}, \dot{p}_{2i}, \dots \dot{p}_{Ni}, p_{11}, p_{12}, \dots p_{1i}, p_{21}, p_{22}, \dots p_{2i}, \dots p_{N1}, p_{N2}, \dots p_{Ni}) = 0 \tag{7.6}$$

The decoupling process is to be accomplished before the spatial discretization is performed to avoid complexity, although the discretized variables $p_{11}, p_{12}, \dots p_{1i}, p_{21}, p_{22}, \dots p_{2i}, p_{N1}, p_{N2}, \dots p_{Ni}$ are symbolically written in $F_1, F_2, \dots F_N$ in Eq. (7.6). For more than one DOF, the decoupling can be done by symbolic algebraic operation in MATLAB (MathWorks Corporation, 2015). After performing the decoupling operation, the spatial discretization procedure in Eqs. (7.1)–(7.4) is followed and finally, Eq. (7.6) takes the following form in terms of all the DOFs $\ddot{p}_{1i}, \ddot{p}_{2i}, \dots \ddot{p}_{Ni}$ explicitly expressed as:

$$\ddot{p}_{1i} = G_1(t, \dot{p}_{1i}, \dot{p}_{2i}, \dots \dot{p}_{Ni}, p_{11}, p_{12}, \dots p_{1i}, p_{21}, p_{22}, \dots p_{2i}, p_{N1}, p_{N2}, \dots p_{Ni})$$

$$\ddot{p}_{2i} = G_2(t, \dot{p}_{1i}, \dot{p}_{2i}, \dots \dot{p}_{Ni}, p_{11}, p_{12}, \dots p_{1i}, p_{21}, p_{22}, \dots p_{2i}, p_{N1}, p_{N2}, \dots p_{Ni})$$

$$\dots \dots \dots$$

$$\ddot{p}_{Ni} = G_N(t, \dot{p}_{1i}, \dot{p}_{2i}, \dots \dot{p}_{Ni}, p_{11}, p_{12}, \dots p_{1i}, p_{21}, p_{22}, \dots p_{2i}, p_{N1}, p_{N2}, \dots p_{Ni}) \tag{7.7}$$

with $i = 1,2,3, \dots M$. The set of equations in Eq. (7.7) contains N second-order ODEs in time where a portion of the right-hand side of each equation contains the dependent variables generated after the spatial discretization. Therefore, G_1, G_2,…G_N are now turned into functions of time and its first derivative only and therefore, $p_{ki}(x_i, t)$ approximates $p_{ki}(t)$ in Fig. 7.1. The set of second-order ODEs in Eq. (7.7) is converted into another set of first-order ODEs by using the following transformations in terms of the generalized deflection, u as below:

$$\dot{p}_{11} = \dot{u}_1 = u_{NM+1}; \quad \dot{p}_{21} = \dot{u}_{M+1} = u_{NM+M+1}; \quad \dots \quad \dot{p}_{N1} = \dot{u}_{(N-1)M+1} = u_{2NM-M+1}$$

$$\dot{p}_{12} = \dot{u}_2 = u_{NM+2}; \quad \dot{p}_{22} = \dot{u}_{M+2} = u_{NM+M+2}; \quad \dots \quad \dot{p}_{N2} = \dot{u}_{(N-1)M+2} = u_{2NM-M+2}$$

$$\dots \dots \dots$$

$$\dot{p}_{1M} = \dot{u}_M = u_{NM+M}; \qquad \dot{p}_{2M} = \dot{u}_{2M} = u_{NM+2M}; \quad \ldots \quad \dot{p}_{NM} = \dot{u}_{NM} = u_{2NM} \tag{7.8}$$

and,

$$\ddot{p}_{11} = \dot{u}_{NM+1} = G_1(i=1); \;\; \ddot{p}_{21} = \dot{u}_{NM+M+1} = G_2(i=1); \;\; \ldots \;\; \ddot{p}_{N1} = \dot{u}_{2NM-M+1} = G_N(i=1)$$

$$\ddot{p}_{12} = \dot{u}_{NM+2} = G_1(i=2); \;\; \ddot{p}_{22} = \dot{u}_{NM+M+1} = G_2(i=2); \;\; \ldots \;\; \ddot{p}_{N2} = \dot{u}_{2NM-M+2} = G_N(i=2)$$

$$\ldots \ldots \ldots$$

$$\ddot{p}_{1M} = \dot{u}_{NM+M} = G_1(i=M); \;\; \ddot{p}_{2M} = \dot{u}_{NM+2M} = G_2(i=M); \;\; \ldots \;\; \ddot{p}_{NM} = \dot{u}_{2NM} = G_N(i=M) \tag{7.9}$$

For M spatial points and N DOFs, the transformations in Eqs. (7.8) and (7.9) contain a system of $2NM$ first-order-time ODEs with u as the generalized dependent variable (middle lanes of each column of equations) and can be solved simultaneously by the 4th order RK method (Chapra and Canale, 2015; Izzo, 2017; Kalogiratou et al., 2014). In order to ensure a converging and stable solution, the proper sequence of arranging the $2NM$ equations is very important prior to the solution. According to that, the first-order-time derivatives of all the original variables ($\dot{u}_1, \dot{u}_2, \ldots \dot{u}_{NM}$ in Eq. (7.8)) are to be written at first followed by the second-order-time derivatives of the original variables ($\dot{u}_{NM+1}, \dot{u}_{NM+2}, \ldots \dot{u}_{2NM}$ in Eq. (7.9)). The resulting $2NM$ first-order equations require $2NM$ ICs as below:

$$u_i(0) = H_1(x_i); \;\; u_{i+M}(0) = H_2(x_i); \;\; u_{i+2M}(0) = H_3(x_i); \;\; \ldots \;\; u_{i+(N-1)M}(0) = H_N(x_i) \tag{7.10}$$

$$u_{i+NM}(0) = K_1(x_i); \;\; u_{i+NM+M}(0) = K_2(x_i); \;\; u_{i+NM+2M}(0) = K_3(x_i); \;\; \ldots \;\; u_{i+NM+(N-1)M}(0) = K_N(x_i) \tag{7.11}$$

where $i = 1,2, \ldots M$. The function H in Eq. (7.10) represents the initial deflections and the function K in Eq. (7.11) defines the initial velocities.

7.5 Final Forms of the Governing Equations for the Method of Lines Solution

7.5.1 The Decoupled Governing Equations

Equations (3.1)–(3.3) in Chapter 3 represent the GDEs for the dynamic response of the helicopter rotor blade subjected to the aerodynamic forces and moment in different flight

conditions as described in Chapters 4 and 5 and are characterized by three coupled DOFs w, v, and θ. From Eqs. (3.1)–(3.3), coupling between w and θ occurs because of Ω and noncoincidence of the EA and the CA. The coupling between w and v occurs due to the asymmetric term D_{bzy}. Also, the term e disappears when θ vanishes meaning that the offset between the EA and the CA does not affect the coupling between w and v. Both w and v are affected by the centrifugal tension related terms $(Tw')'$ and $(Tv')'$, however, in addition to that, v is influenced by the centripetal term $-\Omega^2 mv$ as well. The centrifugal term increases the beam/blade stiffness in both out-of-plane and in-plane directions, while the centripetal term, due to the negative sign, decreases the stiffness in the in-plane direction and causes reduction of the chordwise vibration frequencies.

Since Eqs. (3.1)–(3.3) are triply coupled in terms of w, v, and θ, therefore, $N = 3$. To apply the MOL for the solution, a decoupling is necessary in terms of the second-order-time derivatives for the three DOFs as described in Section 7.4. Substituting w, v, and θ in Eqs. (3.1)–(3.3) by p_1, p_2, and p_3, respectively, and after performing the decoupling operation, the final forms of the decoupled GDEs are expressed as below:

$$
\begin{aligned}
\ddot{p}_{1i} = {} & f_z(x_i,t)\left\{\frac{1}{m}+\frac{e^2\cos^2\alpha_i}{m(\kappa_m^2-e^2)}\right\}-\frac{m_x(x_i,t)e\cos\alpha_i}{m(\kappa_m^2-e^2)}-\frac{f_y(x_i,t)e^2\sin\alpha_i\cos\alpha_i}{m(\kappa_m^2-e^2)} \\
& -\frac{\kappa_m^2}{m(\kappa_m^2-e^2)}(A_i p_{1i}'''' + C_i p_{2i}'''' + 2A_i' p_{1i}''' + 2C_i' p_{2i}''' + A_i'' p_{1i}'' + C_i'' p_{2i}'') \\
& +\frac{e^2\sin^2\alpha_i}{m(\kappa_m^2-e^2)}(A_i p_{1i}'''' + C_i p_{2i}'''' + 2A_i' p_{1i}''' + 2C_i' p_{2i}''' + A_i'' p_{1i}'' + C_i'' p_{2i}'') \\
& +\frac{e^2\cos\alpha_i\sin\alpha_i}{m(\kappa_m^2-e^2)}(C_i p_{1i}'''' + B_i p_{2i}'''' + 2C_i' p_{1i}''' + 2B_i' p_{2i}''' + C_i'' p_{1i}'' + B_i'' p_{2i}'') \\
& +(T_i' p_{1i}' + T_i p_{1i}'')\left\{\frac{1}{m}+\frac{e^2\cos^2\alpha_i}{m(\kappa_m^2-e^2)}\right\}-(T_i' p_{2i}' + T_i p_{2i}'')\frac{e^2\sin\alpha_i\cos\alpha_i}{m(\kappa_m^2-e^2)} \\
& +[\{p_{3i}'(x_i+e_1)+p_{3i}\}\cos\alpha_i-(x_i+e_1)p_{3i}\alpha_i'\sin\alpha_i]\left(\Omega^2 e+\frac{\Omega^2 e^3\cos^2\alpha_i}{\kappa_m^2-e^2}\right) \\
& +\{\sin\alpha_i+x_i\alpha_i'\cos\alpha_i\}\left(\Omega^2 e+\frac{\Omega^2 e^3\cos^2\alpha_i}{\kappa_m^2-e^2}\right) \\
& +\frac{\Omega^2 e^3\sin\alpha_i\cos\alpha_i}{(\kappa_m^2-e^2)}[\{p_{3i}'(x_i+e_1)+p_{3i}\}\sin\alpha_i+(x_i+e_1)p_{3i}\alpha_i'\cos\alpha_i]
\end{aligned}
\tag{7.12}
$$

$$+\frac{\Omega^2 e^3\, p_{3i} sin^2\,\alpha_i\, cos\alpha_i}{k_m^2 - e^2} - \frac{\Omega^2 e^3 sin\alpha_i cos\alpha_i}{k_m^2 - e^2}\{cos\alpha_i - (x_i + e_1)\alpha_i' sin\alpha_i\}$$

$$-\frac{\Omega^2 e^3 sin\alpha_i cos^2\alpha_i}{\kappa_m^2 - e^2} - \frac{D_t p_{3i}'' e cos\alpha_i}{m(k_m^2 - e^2)}$$

$$-\frac{\Omega^2 e^2 cos\alpha_i (p_{2i}' sin\alpha_i - p_{1i}' cos\alpha_i)(x_i + e_1)}{k_m^2 - e^2}$$

$$+\frac{\Omega^2 e(\kappa_{m2}^2 - \kappa_{m1}^2) p_{3i} cos(2\alpha_i) cos\alpha_i}{k_m^2 - e^2} + \frac{\Omega^2 e(\kappa_{m2}^2 - \kappa_{m1}^2) sin\alpha_i\, cos^2\,\alpha_i}{k_m^2 - e^2}$$

$$\ddot{p}_{2i} = f_y(x_i, t)\left\{\frac{1}{m} + \frac{e^2\, sin^2\,\alpha_i}{m(\kappa_m^2 - e^2)}\right\} + \frac{m_x(x_i, t) e sin\alpha_i}{m(\kappa_m^2 - e^2)} - \frac{f_z(x_i, t) e^2 sin\alpha_i cos\alpha_i}{m(\kappa_m^2 - e^2)}$$

$$-\frac{\kappa_m^2}{m(\kappa_m^2 - e^2)}(C_i p_{1i}'''' + B_i p_{2i}'''' + 2C_i' p_{1i}''' + 2B_i' p_{2i}''' + C_i'' p_{1i}'' + B_i'' p_{2i}'')$$

$$+\frac{e^2 cos^2\alpha_i}{m(\kappa_m^2 - e^2)}(C_i p_{1i}'''' + B_i p_{2i}'''' + 2C_i' p_{1i}''' + 2B_i' p_{2i}''' + C_i'' p_{1i}'' + B_i'' p_{2i}'')$$

$$+\frac{e^2 cos\alpha_i sin\alpha_i}{m(\kappa_m^2 - e^2)}(A_i p_{1i}'''' + C_i p_{2i}'''' + 2A_i' p_{1i}''' + 2C_i' p_{2i}''' + A_i'' p_{1i}'' + C_i'' p_{2i}'')$$

$$+(T_i' p_{2i}'' + T_i p_{2i}'')\left\{\frac{1}{m} + \frac{e^2\, sin^2\,\alpha_i}{m(\kappa_m^2 - e^2)}\right\} - (T_i' p_{1i}' + T_i p_{1i}'')\frac{e^2 sin\alpha_i cos\alpha_i}{m(\kappa_m^2 - e^2)}$$

$$-[\{p_{3i}'(x_i + e_1) + p_{3i}\} sin\alpha_i + (x_i + e_1) p_{3i}\alpha_i' cos\alpha_i]\left(\Omega^2 e + \frac{\Omega^2 e^3\, sin^2\,\alpha_i}{\kappa_m^2 - e^2}\right)$$

$$+\{cos\alpha_i - (x_i + e_1)\alpha_i' sin\alpha_i\}\left(\Omega^2 e + \frac{\Omega^2 e^3\, sin^2\,\alpha_i}{\kappa_m^2 - e^2}\right) - \frac{\Omega^2 e^3 p_{3i}\, sin^3\,\alpha_i}{\kappa_m^2 - e^2} \qquad (7.13)$$

$$-\frac{\Omega^2 e^3 sin\alpha_i cos\alpha_i}{(\kappa_m^2 - e^2)}[\{p_{3i}'(x_i + e_1) + p_{3i}\} cos\alpha_i - (x_i + e_1) p_{3i}\alpha_i' sin\alpha_i]$$

$$+\frac{\Omega^2 e^3\, sin^2\,\alpha_i\, cos\alpha_i}{k_m^2 - e^2} - \frac{\Omega^2 e^3 sin\alpha_i cos\alpha_i}{k_m^2 - e^2}\{sin\alpha_i + x_i\alpha_i' cos\alpha_i\}$$

$$+\frac{D_t p_{3i}'' e sin\alpha_i}{m(k_m^2 - e^2)} + \frac{\Omega^2 e^2 sin\alpha_i (p_{2i}' sin\alpha_i - p_{1i}' cos\alpha_i)(x_i + e_1)}{k_m^2 - e^2}$$

$$-\frac{\Omega^2 e(\kappa_{m2}^2 - \kappa_{m1}^2) p_{3i} cos(2\alpha_i) sin\alpha_i}{k_m^2 - e^2} - \frac{\Omega^2 e(\kappa_{m2}^2 - \kappa_{m1}^2)\, sin^2\,\alpha_i\, cos\alpha_i}{k_m^2 - e^2}$$

$$-\Omega^2 e p_{3i} sin\alpha_i + \Omega^2 p_{2i} + \Omega^2 e cos\alpha_i$$

$$
\begin{aligned}
\ddot{p}_{3i} = &-\frac{f_z(x_i,t)ecos\alpha_i}{m(k_m^2-e^2)} + \frac{f_y(x_i,t)esin\alpha_i}{m(k_m^2-e^2)} + \frac{m_x(x_i,t)}{m(k_m^2-e^2)} \\
&+\frac{ecos\alpha_i}{m(k_m^2-e^2)}(A_i p_{1i}'''' + C_i p_{2i}'''' + 2A_i' p_{1i}''' + 2C_i' p_{2i}''' + A_i'' p_{1i}'' + C_i'' p_{2i}'') \\
&-\frac{esin\alpha_i}{m(k_m^2-e^2)}(C_i p_{1i}'''' + B_i p_{2i}'''' + 2C_i' p_{1i}''' + 2B_i' p_{2i}''' + C_i'' p_{1i}'' + B_i'' p_{2i}'') \\
&-\frac{ecos\alpha_i}{m(k_m^2-e^2)}(T_i' p_{1i}' + T_i p_{1i}'') + \frac{esin\alpha_i}{m(k_m^2-e^2)}(T_i' p_{2i}' + T_i p_{2i}'') \\
&-\frac{\Omega^2 e^2 cos\alpha_i}{k_m^2-e^2}[\{p_{3i}'(x_i+e_1)+p_{3i}\}cos\alpha_i - (x_i+e_1)p_{3i}\alpha_i' sin\alpha_i] \\
&-\frac{\Omega^2 e^2 cos\alpha_i}{k_m^2-e^2}\{sin\alpha_i + x_i\alpha_i' cos\alpha_i\} + \frac{\Omega^2 e^2 sin\alpha_i}{k_m^2-e^2}\{cos\alpha_i - (x_i+e_1)\alpha_i' sin\alpha_i\} \\
&-\frac{\Omega^2 e^2 sin\alpha_i}{k_m^2-e^2}[\{p_{3i}'(x_i+e_1)+p_{3i}\}sin\alpha_i + (x_i+e_1)p_{3i}\alpha_i' cos\alpha_i] \\
&-\frac{\Omega^2 e^2 p_{3i}\, sin^2\,\alpha_i}{(k_m^2-e^2)} + \frac{\Omega^2 e^2 sin\alpha_i cos\alpha_i}{k_m^2-e^2} + \frac{D_t p_{3i}''}{m(k_m^2-e^2)} \\
&+\frac{\Omega^2 e(p_{2i}' sin\alpha_i - p_{1i}' cos\alpha_i)(x_i+e_1)}{k_m^2-e^2} - \frac{\Omega^2(k_{m2}^2-k_{m1}^2)p_{3i}cos(2\alpha_i)}{k_m^2-e^2} \\
&-\frac{\Omega^2(k_{m2}^2-k_{m1}^2)sin\alpha_i cos\alpha_i}{k_m^2-e^2}
\end{aligned}
\tag{7.14}
$$

where

$$A_i = A(x_i) = D_{by}(x_i) \tag{7.15}$$

$$B_i = B(x_i) = D_{bz}(x_i) \tag{7.16}$$

$$C_i = C(x_i) = D_{bzy}(x_i) \tag{7.17}$$

with $i = 1,2,\ldots M$ and $\alpha_i = \alpha(x_i)$ indicating the total blade cross-section angle at any station x_i prior to any deformation. $D_{b\eta}$ and $D_{b\xi}$ are the bending stiffnesses with respect to the principal axes η and ξ through the shear center, respectively, as shown in Fig. 3.2 with α as the angle measured between the global y-z and the principal η-ξ axis systems through the shear center. The expressions of $D_{by}(x)$, $D_{bz}(x)$, and $D_{bzy}(x)$ in terms of $D_{b\eta}$ and $D_{b\xi}$ are given by Eqs. (3.6)–(3.8) in Chapter 3.

7.5.2 Transformation of the Boundary Conditions

The corresponding BCs for the GDEs of Eqs. (3.1)–(3.3) are given by Eqs. (3.9) and (3.10) and are transformed appropriately by utilizing Eqs. (7.1)–(7.4), (3.4), and (3.11)–(3.15).

$at\ x = 0\ (i = 0)$:

$$[p_1]_{i=0} = [p_1]_0 = 0 \Rightarrow p_{10} = 0 \tag{7.18}$$

$$[p_1']_{i=0} = [p_1']_0 = 0 \Rightarrow \frac{p_{11} - p_{1(-1)}}{2h} = 0 \Rightarrow p_{1(-1)} = p_{11} \tag{7.19}$$

Similarly,

$$p_{20} = 0 \tag{7.20}$$

$$p_{2(-1)} = p_{21} \tag{7.21}$$

$$p_{30} = 0 \tag{7.22}$$

$at\ x = l\ (i = M)$:

for $S_z(l,t) = 0$,

$$\begin{aligned} &\left[-M_y' + Tw' + \Omega^2 me(x + e_1)(sin\alpha + \theta cos\alpha)\right]_{i=M} = 0 \\ &\Rightarrow [-(Ap_1'' + Cp_2'')' + Tp_1' + \Omega^2 me(x + e_1)(sin\alpha + \theta cos\alpha)]_M = 0 \\ &\Rightarrow -A_M p_{1M}''' - A_M' p_{1M}'' - C_M p_{2M}''' - C_M' p_{2M}'' + T_M p_{1M}' \\ &\qquad + \Omega^2 me(x_M + e_1)(sin\alpha_M + \theta_M cos\alpha_M) = 0 \end{aligned} \tag{7.23}$$

$T_M = T(x_M) = T(l) = 0$ from Eq. (3.4) and $x_M = l$ which can be directly used in Eq. (7.23). Using these relationships and Eq. (7.1) for A_M' and C_M' at $i = M$, Eq. (7.23) can be rewritten as:

$$\begin{aligned} &A_M \left[\frac{p_{1(M+2)} - 2p_{1(M+1)} + 2p_{1(M-1)} - p_{1(M-2)}}{2h^3}\right] \\ &+ \left[\frac{A_{M+1} - A_{M-1}}{2h}\right]\left[\frac{p_{1(M+1)} - 2p_{1M} + p_{1(M-1)}}{h^2}\right] \end{aligned} \tag{7.24}$$

$$+C_M\left[\frac{p_{2(M+2)}-2p_{2(M+1)}+2p_{2(M-1)}-p_{2(M-2)}}{2h^3}\right]$$
$$+\left[\frac{C_{M+1}-C_{M-1}}{2h}\right]\left[\frac{p_{2(M+1)}-2p_{2M}+p_{2(M-1)}}{h^2}\right]$$
$$=\Omega^2 me(l+e_1)(sin\alpha_M+\theta_M cos\alpha_M)$$

and finally,

$$A_M\{p_{1(M+2)}-2p_{1(M+1)}+2p_{1(M-1)}-p_{1(M-2)}\}$$
$$+\{A_{M+1}-A_{M-1}\}\{p_{1(M+1)}-2p_{1M}+p_{1(M-1)}\}$$
$$+C_M\{p_{2(M+2)}-2p_{2(M+1)}+2p_{2(M-1)}-p_{2(M-2)}\} \quad (7.25)$$
$$+\{C_{M+1}-C_{M-1}\}\{p_{2(M+1)}-2p_{2M}+p_{2(M-1)}\}$$
$$=2h^3\Omega^2 me(l+e_1)(sin\alpha_M+\theta_M cos\alpha_M)$$

Similarly, for the remaining BCs,

$$A_M p_{1(M+1)}+C_M p_{2(M+1)}=2A_M p_{1M}+2C_M p_{2M}-A_M p_{1(M-1)}-C_M p_{2(M-1)} \quad (7.26)$$

$$B_M\{p_{2(M+2)}-2p_{2(M+1)}+2p_{2(M-1)}-p_{2(M-2)}\}$$
$$+\{B_{M+1}-B_{M-1}\}\{p_{2(M+1)}-2p_{2M}+p_{2(M-1)}\}$$
$$+C_M\{p_{1(M+2)}-2p_{1(M+1)}+2p_{1(M-1)}-p_{1(M-2)}\} \quad (7.27)$$
$$+\{C_{M+1}-C_{M-1}\}\{p_{1(M+1)}-2p_{1M}+p_{1(M-1)}\}$$
$$=2h^3\Omega^2 me(l+e_1)(cos\alpha_M-\theta_M sin\alpha_M)$$

$$C_M p_{1(M+1)}+B_M p_{2(M+1)}=2C_M p_{1M}+2B_M p_{2M}-C_M p_{1(M-1)}-B_M p_{2(M-1)} \quad (7.28)$$

$$p_{3(M+1)}=p_{3(M-1)} \quad (7.29)$$

Equations (7.18)–(7.22) represent the transformed BCs at $x=0$ in Eq. (3.9) and Eqs. (7.25)–(7.29) give the transformed BCs at $x=l$ in Eq. (3.10). The subscripts $M-2$, $M-1$, M, $M+1$, and $M+2$ in Eqs. (7.25)–(7.29) indicate the corresponding evaluations at points x_{M-2}, x_{M-1}, x_M, x_{M+1}, and x_{M+2}, respectively. From Eqs. (7.25)–(7.28), there are four imaginary

deflections $p_{1(M+1)}$, $p_{2(M+1)}$, $p_{1(M+2)}$, and $p_{2(M+2)}$ at two imaginary points x_{M+1} and x_{M+2} outside the boundary and therefore, must be expressed in terms of the known deflections at the internal as well as the boundary points in the x domain. In order to do that, Eqs. (7.25)–(7.28) are rearranged in the following forms:

$$\begin{aligned} a_1 p_{1(M+2)} + a_3 p_{2(M+2)} + a_4 p_{1(M+1)} + a_5 p_{2(M+1)} = \; & a_6 p_{1M} + a_7 p_{2M} \\ -a_8 p_{1(M-1)} - a_9 p_{2(M-1)} + a_1 p_{1(M-2)} + a_3 p_{2(M-2)} + a_{13}(a_{14} + p_{3M} a_{15}) & \end{aligned} \tag{7.30}$$

$$a_1 p_{1(M+1)} + a_3 p_{2(M+1)} = 2a_1 p_{1M} + 2a_3 p_{2M} - a_1 p_{1(M-1)} - a_3 p_{2(M-1)} \tag{7.31}$$

$$\begin{aligned} a_3 p_{1(M+2)} + a_2 p_{2(M+2)} + a_5 p_{1(M+1)} + a_{10} p_{2(M+1)} = \; & a_7 p_{1M} + a_{11} p_{2M} \\ -a_9 p_{1(M-1)} - a_{12} p_{2(M-1)} + a_3 p_{1(M-2)} + a_2 p_{2(M-2)} + a_{13}(a_{15} - p_{3M} a_{14}) & \end{aligned} \tag{7.32}$$

$$a_3 p_{1(M+1)} + a_2 p_{2(M+1)} = 2a_3 p_{1M} + 2a_2 p_{2M} - a_3 p_{1(M-1)} - a_2 p_{2(M-1)} \tag{7.33}$$

where

$$a_1 = A_M \tag{7.34}$$

$$a_2 = B_M \tag{7.35}$$

$$a_3 = C_M \tag{7.36}$$

$$a_4 = A_{M+1} - 2A_M - A_{M-1} \tag{7.37}$$

$$a_5 = C_{M+1} - 2C_M - C_{M-1} \tag{7.38}$$

$$a_6 = 2(A_{M+1} - A_{M-1}) \tag{7.39}$$

$$a_7 = 2(C_{M+1} - C_{M-1}) \tag{7.40}$$

$$a_8 = A_{M+1} + 2A_M - A_{M-1} \tag{7.41}$$

$$a_9 = C_{M+1} + 2C_M - C_{M-1} \tag{7.42}$$

$$a_{10} = B_{M+1} - 2B_M - B_{M-1} \tag{7.43}$$

$$a_{11} = 2(B_{M+1} - B_{M-1}) \tag{7.44}$$

$$a_{12} = B_{M+1} + 2B_M - B_{M-1} \tag{7.45}$$

$$a_{13} = 2h^3\Omega^2 me(l + e_1) \tag{7.46}$$

$$a_{14} = sin\alpha_M \tag{7.47}$$

$$a_{15} = cos\alpha_M \tag{7.48}$$

Equations (7.30)–(7.33) are solved algebraically in MATLAB (MathWorks Corporation, 2015) for the four imaginary deflections $p_{1(M+1)}$, $p_{2(M+1)}$, $p_{1(M+2)}$, and $p_{2(M+2)}$ and after performing some algebraic manipulations, the four imaginary deflections are expressed in terms of the known deflections of the internal and the boundary nodes in the following form:

$$p_{1(M+2)} = 2p_{1M} - p_{1(M-1)} \tag{7.49}$$

$$p_{2(M+1)} = 2p_{2M} - p_{2(M-1)} \tag{7.50}$$

$$p_{1(M+2)} = 4p_{1M} - 4p_{1(M-1)} + p_{1(M-2)} + \frac{a_{13}[(-a_3 + a_2 p_{3M})a_{15} + (a_2 + a_3 p_{3M})a_{14}]}{a_{16}} \tag{7.51}$$

$$p_{2(M+2)} = 4p_{2M} - 4p_{2(M-1)} + p_{2(M-2)} + \frac{a_{13}[(-a_1 + a_3 p_{3M})a_{15} + (a_3 + a_1 p_{3M})a_{14}]}{a_{17}} \tag{7.52}$$

where

$$a_{16} = -a_3^2 + a_1 a_2 \tag{7.53}$$

$$a_{17} = a_3^2 - a_1 a_2 \tag{7.54}$$

7.5.3 Transformation of the Initial Conditions

For steady state response, zero ICs are used which are written below after transformation:

$at\ t = 0$:

$$p_{1i} = 0 \tag{7.55}$$

$$p_{2i} = 0 \tag{7.56}$$

$$p_{3i} = 0 \tag{7.57}$$

$$\dot{p}_{1i} = 0 \tag{7.58}$$

$$\dot{p}_{2i} = 0 \tag{7.59}$$

$$\dot{p}_{3i} = 0 \tag{7.60}$$

with $i = 1,2 \ldots M$.

Following the transformations in Eqs. (7.8) and (7.9) for $N = 3$ and by using Eqs. (7.18)–(7.22), (7.29), (7.49)–(7.52), and (7.55)–(7.60), Eqs. (7.12)–(7.14) are converted into $6M$ first-order-time ODEs and are solved numerically by MATLAB (MathWorks Corporation, 2015).

CHAPTER 8

Parameters and Properties

8.1 Free Vibration Analysis

8.1.1 Material Properties of the Proposed Cross-Section

The sectional properties of the proposed composite, sandwich beam cross-section in Fig. 2.1 are estimated by using the analytical methodology developed in Chapter 2 and are used for the free vibration analysis. The material properties constructing the proposed cross-section are given in Tables 8.1 and 8.2 (Product Information–Rohacell; HexWeb Honeycomb Attributes and Properties; Rasheed, 2014).

Table 8.1. Properties of the fiberglass-epoxy composite outer shell

Properties	Value	Properties	Value
ρ_{shell}	2100 kg/m^3	ν_{12}	0.28
E_1	45e9 Pa	G_{12}	5.5e9 Pa
E_2	12e9 Pa	h_{shell}	0.002 m

Table 8.2. Properties of the Rohacell-Honeycomb isotropic inner core

Rohacell		Honeycomb	
Properties	Value	Properties	Value
ρ_r	75 kg/m^3	ρ_h	48 kg/m^3
E_r	105e6 Pa	E_h	128e6 Pa

where ν_{12}, E_1, E_2, and G_{12} indicate the major Poisson's ratio, the elastic modulus in the fiber direction, the elastic modulus in the transverse direction, and the in-plane shear modulus of the composite shell, respectively. All the other symbols are defined in Chapter 2.

8.1.2 Parameters and Properties of the Helicopter Rotor Blade

The parameters and properties used for the free vibration analysis of the Bo 105 helicopter rotor blade having the proposed composite cross-sectional profile in Chapter 2 are the

same as those mentioned in Table 8.3 for the forced response analysis with the following exceptions:

Exceptions in using properties of Table 8.3: Free Vibration Analysis

1. The length of the blade, l is considered the same as the rotor radius, R with $e_1 = 0$.

2. No twist is considered for the free vibration analysis, i.e., $\alpha = \alpha_t = \Delta\alpha_t = 0$.

3. The sectional properties m, D_{by}, D_{bz}, and D_t of the proposed composite, sandwich beam cross-section are estimated from the analytical method developed in Chapter 2 by using the properties in Tables 8.1 and 8.2 and are different from D_{by}, D_{bz}, and D_t in Table 8.3. Following this, all the other parameters regarding the modeling of the cross-section and the calculation of the profile of the reference surface are determined by using SolidWorks (Dassault Systèmes, 2015) and MATLAB (MathWorks Corporation, 2015) including the use of the classical lamination plate theory for composites.

8.2 Forced Response Analysis

8.2.1 Parameters and Properties of the Bo 105 Helicopter Rotor Blade

The parameters and properties of the Bo 105 helicopter rotor blade used for the forced response analysis are taken from the literature (Ganguli, 2002; Goulos et al., 2015; Prouty, 2002; Staley, 1976; Wang et al., 1988) and are listed in Table 8.3.

Table 8.3. Parameters of the Bo 105 helicopter and the main rotor blade

Parameters	Value	Parameters	Value	Parameters	Value
R	4.91 m	Ω	44.50 rad/s	D_{by}	124907 Nm^2
c	0.27 m	σ	0.07	D_{bz}	199257 Nm^2
l	4.61 m	$\Delta\alpha_t$	$-8°$	D_t	45720 Nm^2
m	6.46 kg/m	κ_m/R	0.029	W_g	2200 kg
e	-0.0188 m	κ_{m1}/R	0	V_{tip}	218.5 m/s
e_1	0.30 m	DL	284.98 N/m^2	V_{NE}	69.30 m/s
A_d	75.73 m^2	C_T/σ	0.071	No. of blades	4
Lock no.	5.5	Airfoil	NACA 23012	Rotor type	Hingeless

8.2.2 Parameters and Properties of the Beam for Validation of the Numerical Model

Tables 8.4 and 8.5 give the necessary parameters and properties used in the steady-state, forced response analysis of a rotating twisted, cantilever beam with two coupled DOFs for the validation of the numerical solution obtained from the generalized MOL. The two coupled DOFs include the out-of-plane bending and the in-plane bending motions of the beam with a rectangular cross-section.

Table 8.4. Properties of the beam for numerical model validation

Properties	Value	Properties	Value
m	2.51 kg/m	l	0.46 m
D_{by}	341.4 Nm^2	e_1	0.15 m
D_{bz}	8534 Nm^2	Ω	164.09 rad/s
$\Delta\alpha_t$	–40°	e	0

Table 8.5. Forcing function parameters of the beam used for numerical model validation

Parameters	Value	Parameters	Value
f_z	$P_1 sin(\omega t)$ N/m	P_1	$200x$ N/m
f_y	$P_2 sin(\omega t)$ N/m	P_2	$4500x$ N/m

8.2.3 Control Parameters for the Forward Flight

Table 8.6 provides the flight control parameters considered for the steady-state and the unsteady forced response of the helicopter rotor blade at the forward flight for different advance ratios (Goulos et al., 2015; Ramanujam et al., 2015).

Table 8.6. Control parameters for the forward flight

	Parameters				
μ	C_T/σ	α_s	α_{p0}	α_{1c}	α_{1s}
0.197	0.071	−4.8°	12.3°	2.4°	−1.9°
0.259	0.071	−7.1°	13.5°	2.1°	−2.2°
0.313	0.071	−9.6°	15.5°	1.8°	−3°

CHAPTER 9

Results and Discussions

9.1 Free Vibration: Frequency Analysis

9.1.1 Convergence Study

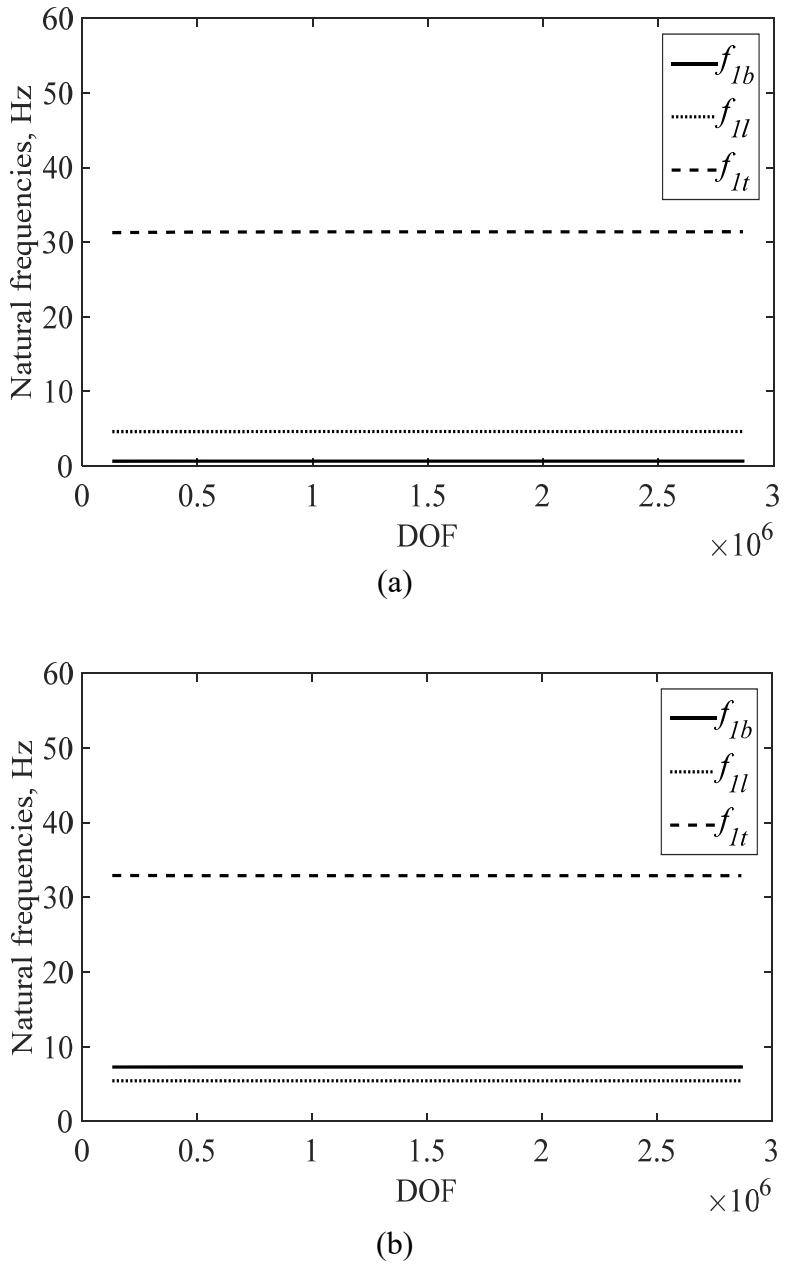

Fig. 9.1. Variations of the fundamental natural frequencies of the triply coupled vibration with DOFs for (a) the nonrotating case (b) the rotating case

Figure 9.1 explains the variation of the fundamental natural frequencies of the triply coupled vibration of the rotor blade having the proposed composite cross-section with the DOFs for the nonrotating and rotating cases. The frequencies are obtained from the FE analysis in Abaqus (Dassault Systèmes SIMULIA Corporation, 2012) with the finest element size of 0.008 m. From Fig. 9.1, as the DOF increases, the trends of the natural frequencies become flattened after showing some initial changes indicating that the solution is already converged.

9.1.2 Model Validation: Natural Frequencies and Mode Shapes—Nonrotating Case

Table 9.1 lists the natural frequencies of free vibration of the triply coupled, nonrotating helicopter rotor blade composed of the proposed composite section for the first three modes obtained by the analytical method and the FE analysis in Abaqus (Dassault Systèmes SIMULIA Corporation, 2012). Here, f_{nf}, f_{nl}, and f_{nt} indicate the n^{th} natural frequencies in Hz with the subscripts f, l, and t denoting the flapping, lead-lag, and torsional vibration modes, respectively. From Table 9.1, reasonable agreement is found between the analytical and the FE frequencies. This substantiates a good validation of the analytical method developed in Chapter 2 for estimating the properties of a composite, sandwich beam cross-section.

Table 9.1. Natural frequencies of the coupled vibration for the nonrotating blade

	Natural Frequencies, Hz					
	f_{nf}		f_{nl}		f_{nt}	
	Analytical	FE	Analytical	FE	Analytical	FE
$n = 1$	0.69	0.65	4.74	4.61	29.37	31.36
$n = 2$	4.33	4.04	29.72	28.73	88.03	93.93
$n = 3$	12.13	11.27	83.22	79.48	146.60	157.10

Table 9.2. % Error between the analytical and the FE frequencies for the nonrotating blade

	% Error		
	f_{nf}	f_{nl}	f_{nt}
$n = 1$	5.79	2.74	6.77
$n = 2$	6.69	3.33	6.47
$n = 3$	7.08	4.49	7.16

Table 9.2 lists the error level associated with the nonrotating frequencies of the triply coupled free vibration obtained from the analytical and the FE techniques. From Table 9.2, the error level of f_{nf} is slightly lower than that of f_{nt} indicating that the analytical estimate of D_t is a little higher than that from the FE method. f_{nl} has the least error level because of the much higher in-plane bending stiffness than the out-of-plane bending or torsional stiffness. It is concluded that f_{nt} would be less sensitive to error than f_{nf} for higher modes. One reason for this is, for a particular mode, f_{nt} is much higher in magnitude than f_{nf} or f_{nl}. Another explanation is that, the blade can be considered as a long, thin plate due to its geometry which is more prone to bending rather than torsion. The effect of e is small on the coupled vibration since the shear center is very close to the centroid in the proposed cross-section. This is justified by the first uncoupled bending vibration frequency as $\left[(1.875/l)^2\sqrt{D_{by}/\rho A_c}\right]/2\pi$ = 0.69 Hz which is the same as f_{1f} in Table 9.1. However, in higher modes, the coupling effect can be influential with relatively greater effect of e on the natural frequencies.

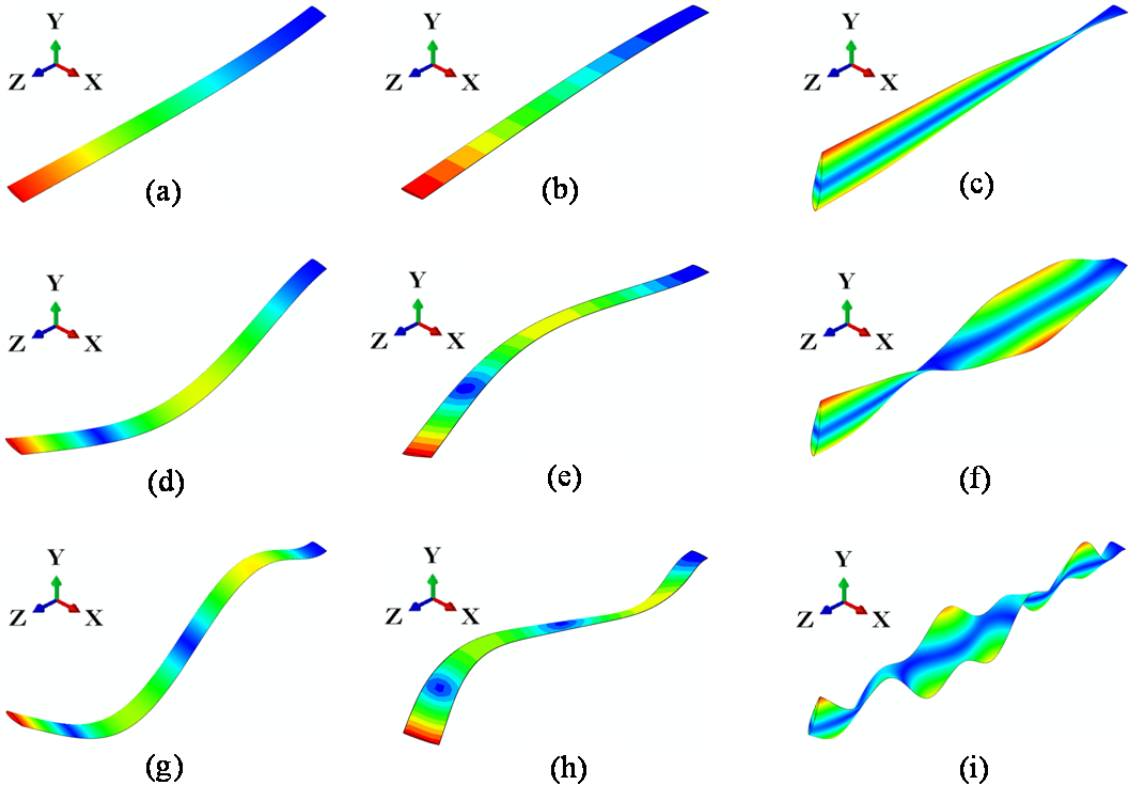

Fig. 9.2. Mode shapes of the nonrotating blade governed by (a) 1st mode flapping (b) 1st mode lead-lag (c) 1st mode torsion (d) 2nd mode flapping (e) 2nd mode lead-lag (f) 2nd mode torsion (g) 3rd mode flapping (h) 3rd mode lead-lag (i) 3rd mode torsion

Figures 9.2(a) through 9.2(i) depict the mode shapes of the triply coupled vibration of the nonrotating helicopter rotor blade with the proposed cross-section. The fundamental flapping and the lead-lag mode shapes are given in Figs. 9.2(a) and (b), respectively, with no node along the length of the blade while Fig. 9.2(c) shows the fundamental torsion governed mode having a blue axis running parallel to the elastic axis of the blade. This axis goes through the shear center suggesting that the blade is about to rotate with respect to this axis. Figures 9.2(d)–(f) explain the similar phenomena for the second mode governed by the flapping, lead-lag, and torsion, respectively, each having one node. Following this, Figs. 9.2(g)–(i) describe the third mode of the triply coupled vibration each having two nodes. Although, the coupling effect as seen from the mode shapes seems to be smaller, it can gradually become larger with higher modes as previously discussed. This seems possible from Figs. 9.2(g) and (f), where in the former, the torsional effect is obvious and in the latter, the blue axis gets distorted due to the coupled effect. From the first three mode shapes in Fig. 9.2, the blade can be considered to vibrate close to its fundamental modes.

9.1.3 Model Validation: Natural Frequencies and Mode Shapes—Rotating Case

Table 9.3. Natural frequencies of the coupled vibration for the rotating blade

	Natural Frequencies, Hz					
	f_{nf}		f_{nl}		f_{nt}	
	Analytical	FE	Analytical	FE	Analytical	FE
$n = 1$	7.76	7.27	5.65	5.42	29.37	32.88
$n = 2$	18.53	18.06	34.05	32.95	88.03	95.45
$n = 3$	32.29	30.17	88.16	83.96	146.62	161.02

Table 9.3 lists the first three frequencies of free vibration of the same triply coupled rotor blade in Section 9.1.2 but for the rotating case. This time, the f_{nf} is much higher than that for the nonrotating case. This is due to the addition of the rotational stiffness developed by the rotating blade for which the contribution is significantly greater than the nonrotating case. The high rotational stiffness weakens the coupling between bending and torsional DOFs and significantly affects the bending behavior rather than torsion. Although, the rotational stiffness also adds to the f_{nt}, however, with much less priority compared to the f_{nf}. A comparison of the f_{nt} obtained

from the FE analysis for the nonrotating and rotating cases from Tables 9.1 and 9.3 reveals that, f_{1t} increases by 4.84% for the rotating case. On the other hand, f_{1f} increases by 1018% showing the more severe influence of the rotational stiffness on f_{nb}. The associated error level in the frequency is shown in Table 9.4 which indicates that the error in the lead-lag frequencies is the least. The reason is the again the much higher in-plane bending stiffness for the lead-lag motion.

Table 9.4. % Error between the analytical and the FE frequencies for the rotating blade

	% Error		
	f_{nf}	f_{nl}	f_{nt}
$n = 1$	6.31	4.07	11.95
$n = 2$	2.53	3.23	8.43
$n = 3$	6.56	4.76	9.82

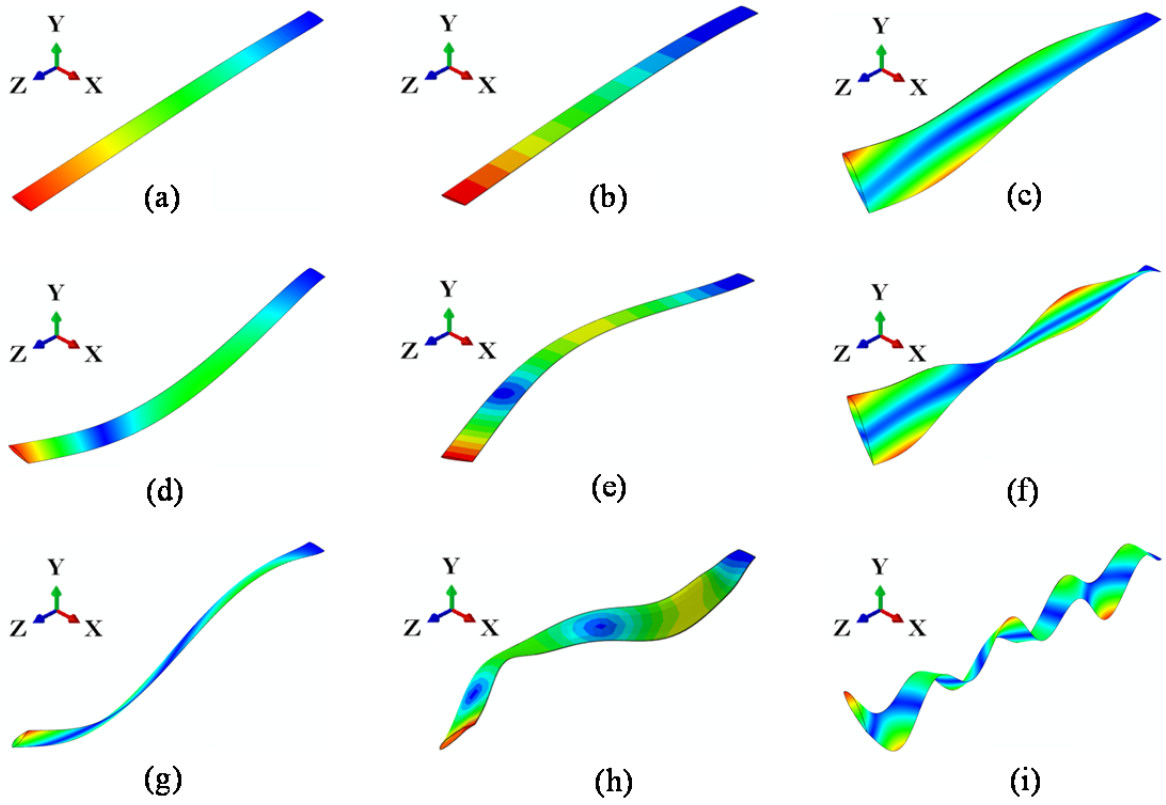

Fig. 9.3. Mode shapes of the rotating blade governed by (a) 1st mode flapping (b) 1st mode lead-lag (c) 1st mode torsion (d) 2nd mode flapping (e) 2nd mode lead-lag (f) 2nd mode torsion (g) 3rd mode flapping (h) 3rd mode lead-lag (i) 3rd mode torsion

Figures 9.3(a) through (f) describe the mode shapes of the triply coupled vibration of the rotating helicopter rotor blade. These mode shapes are similar to that of Fig. 9.2; however, unlike Fig. 9.2, they are affected by the additional rotational stiffness which makes them tauter. The effect is, as usual, more significant for the flapping modes than the torsion governed ones. The torsion governed mode shapes in Figs. 9.3(b), (f), and (i) show that they do not maintain the exact sinusoidal pattern as used in the nonrotating coupled vibration. This is also true for the bending governed modes. The first three mode shapes of the triply coupled rotating blade having the proposed composite cross-section are plotted in Figs. 9.4(a)–(c).

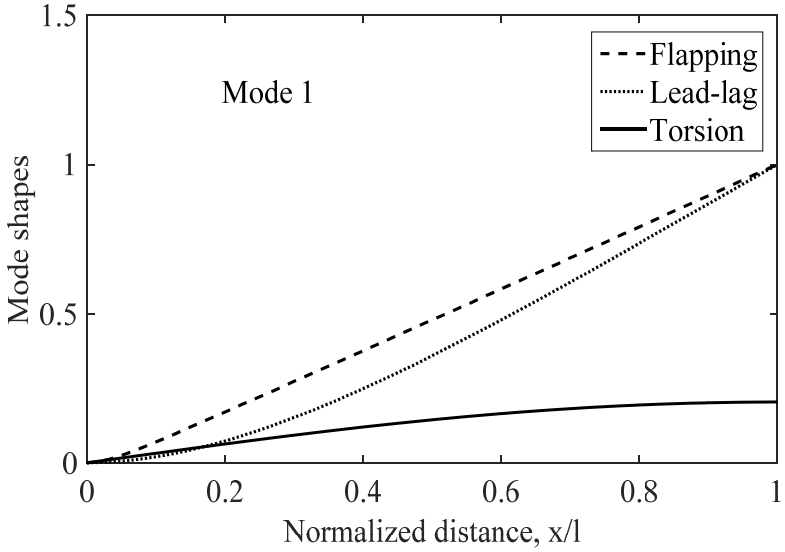

(a)

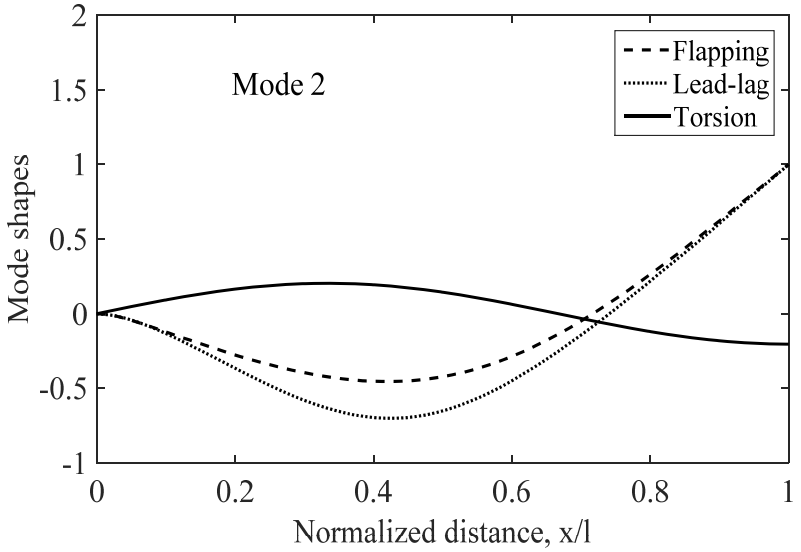

(b)

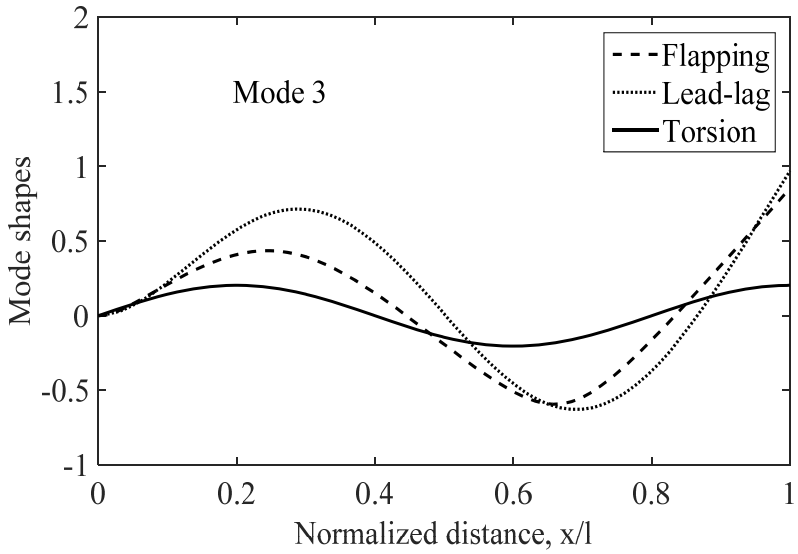

(c)

Fig. 9.4. Mode shapes of the triply coupled rotating helicopter blade (a) mode 1 (b) mode 2 (c) mode 3

9.2 Forced Response: Time-Varying Deflections and Velocities

9.2.1 Model Validation: The Generalized Method of Lines

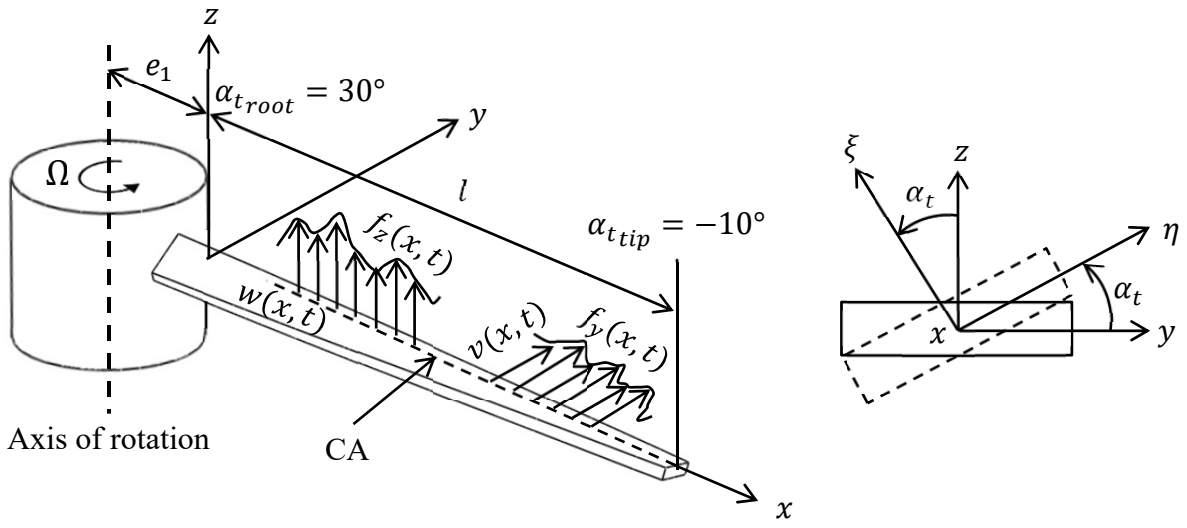

Fig. 9.5. Rotating beam under in-plane and out-of-plane distributed loads

The numerical solution offered by the generalized MOL formulated in Chapter 7 is used to estimate the forced response of the Bo 105 helicopter rotor in hovering and forward flights. In order to validate the MOL solution, the steady-state, coupled, forced vibration of a rotating, twisted cantilever beam with two DOFs is considered as shown in Fig. 9.5. The out-of-plane and

in-plane bending deflections, w and v, respectively, at the tip and at the midpoint of the beam are obtained by the generalized MOL for the parameters listed in Tables 8.4 and 8.5 in Chapter 8 with $\omega_e = 20$ rad/s and are compared directly to that obtained from Abaqus (Dassault Systèmes SIMULIA Corporation, 2012). The results are in good agreement as depicted in Figs. 9.6(a) and (b) with the maximum deviation of 3.13% and 2.91% between the peaks, for w and v, respectively, which indicates that the developed numerical solution is validated and generalized.

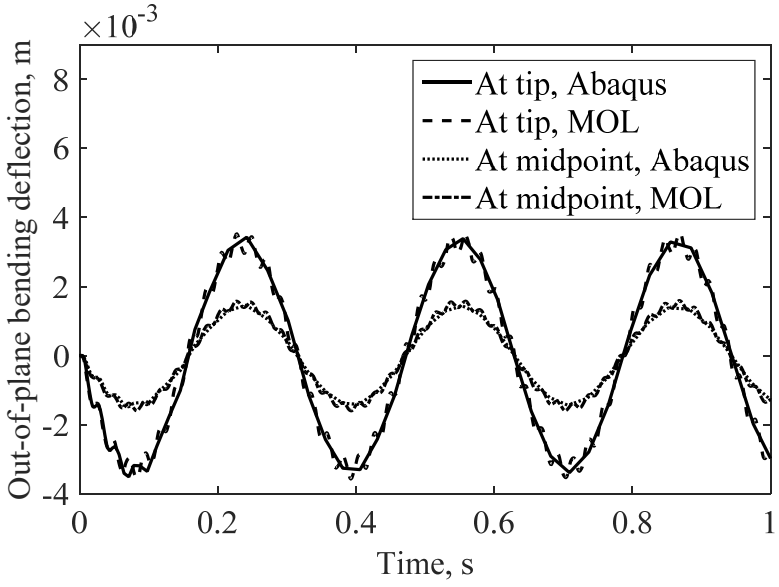

(a)

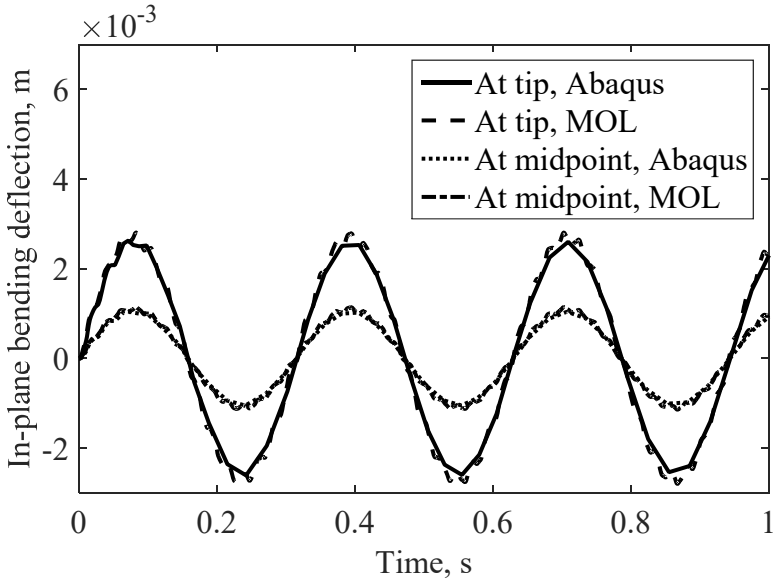

(b)

Fig. 9.6. Time-varying (a) out-of-plane (b) in-plane bending deflections at the tip and at the midpoint of the beam with $M = 20$ and $\omega_e = 20$ rad/s

9.2.2 Variations of the Rotor Blade Deflections with Time for Steady-State Hovering Flight

Figures 9.7(a)–(c) explain the characteristics of the steady-state, time-varying coupled flapping, lead-lag, and torsional deflections, respectively, at the tip of the helicopter rotor blade $(x/l = 1)$ for the hovering flight. The behaviors of the coupled DOFs with time are obtained numerically by the generalized MOL showing that they are oscillatory in nature which is due to the harmonic nature of the applied forcing functions.

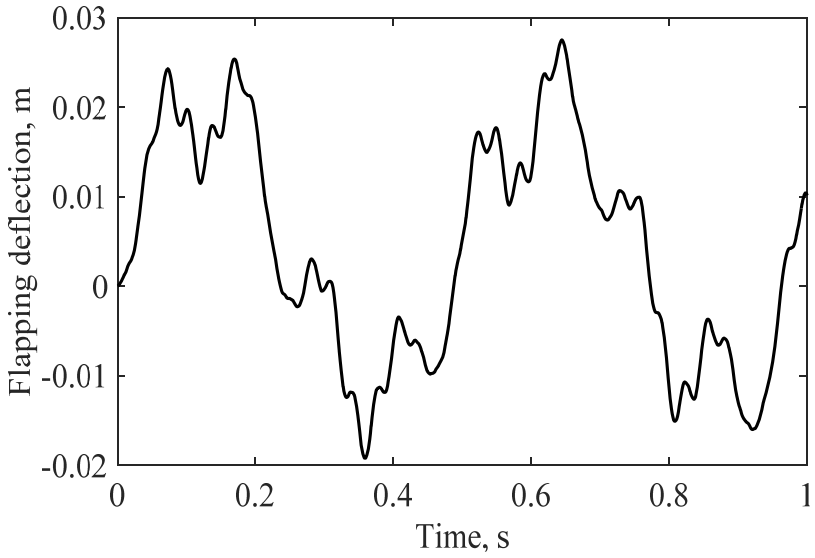

(a)

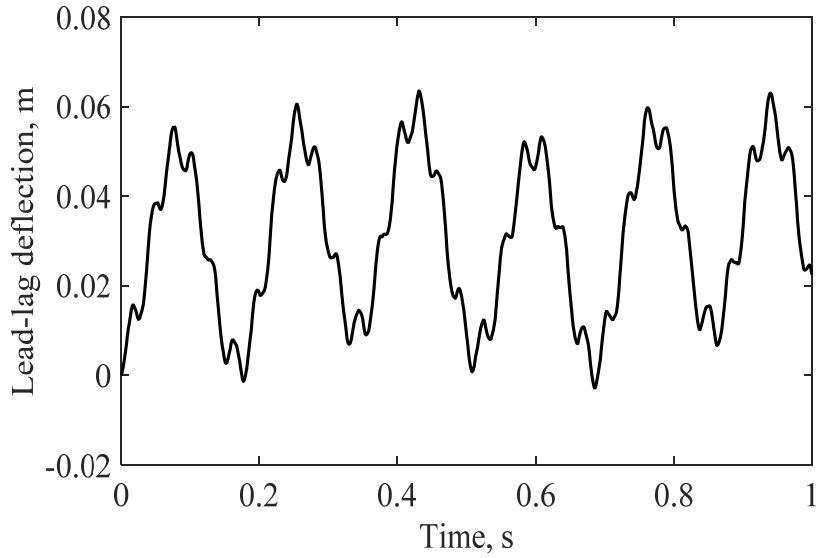

(b)

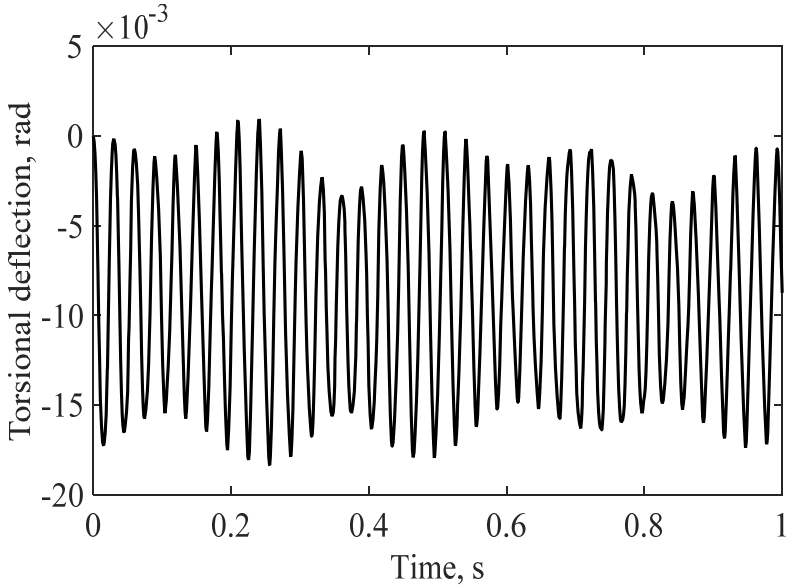

(c)

Fig. 9.7. Variations of the (a) flapping (b) lead-lag (c) torsional deflections at the tip of the helicopter rotor blade with time for steady-state hovering flight

In Fig. 9.7(a), the steady-state flapping deflection fluctuates between 0.027 m and -0.019 m, which is due to the harmonic forcing function the magnitude of which is a certain percentage of the total flapping force. The tip is subjected to upward and downward deflections from its equilibrium position. One interesting feature observed from Fig. 9.7(b) is much higher positive amplitude of the lead-lag deflection than the negative one from the initial state which is attributed to the significant contribution of the term $\Omega^2 e$ as well as the BC. The strength of the coupling between the DOFs is determined by the magnitude of e. The higher the value of e, the greater the coupling. In Fig. 9.7(c), the torsional deflection fluctuates between the maximum and the minimum values of 0.001 rad and -0.018 rad, respectively, with the tendency to show greater oscillation than that of flapping and lead-lag DOFs. This magnitude of the torsional deflection is attributable to the magnitude of the moment function generated from both the aerodynamic moment and the moment with respect to the shear center induced by the lift force.

9.2.3 Variations of the Rotor Blade Deflections with Nondimensional Time for Steady-State Forward Flight

The GDEs (3.1)–(3.3) for the coupled DOFs of motion become nonlinear upon inclusion of the aerodynamic loadings described in Chapter 5 for the forward flight. However, an efficient

numerical solution is achieved by the generalized MOL with the same number of points as used for the hovering light. The nonlinear out-of-plane flapping force f_z depends on $\dot{w}$ and $\dot{v}$ which in turn, depend on f_z thereby affecting w in a loop. The same phenomenon also applies to f_y for estimating the magnitude of v. Following this, the magnitude of θ is determined by the applied torque m_x which contains the nonlinear f_z and thereby, shows the nonlinear behavior. Since the aerodynamic damping is much higher for the flapping motion compared to that of the lead-lag motion, the periodicity of the solution for the lead-lag deflection takes more iterations for ensuring the converged results.

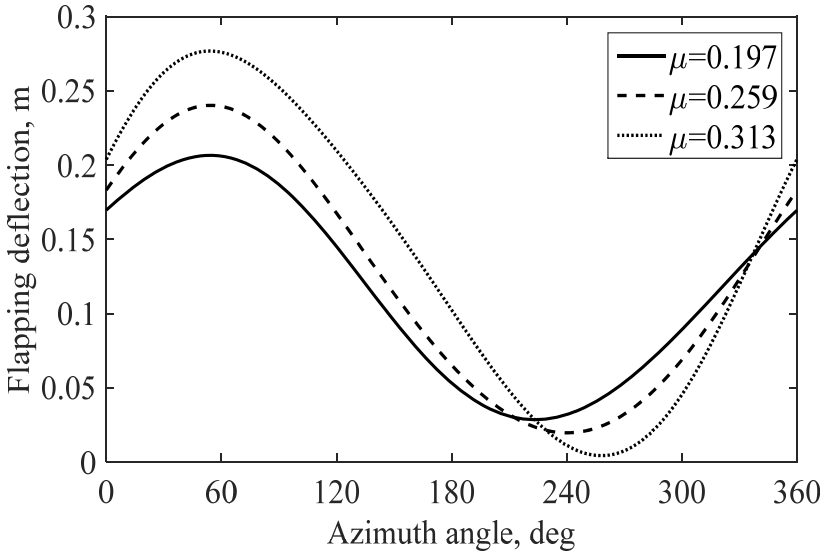

(a)

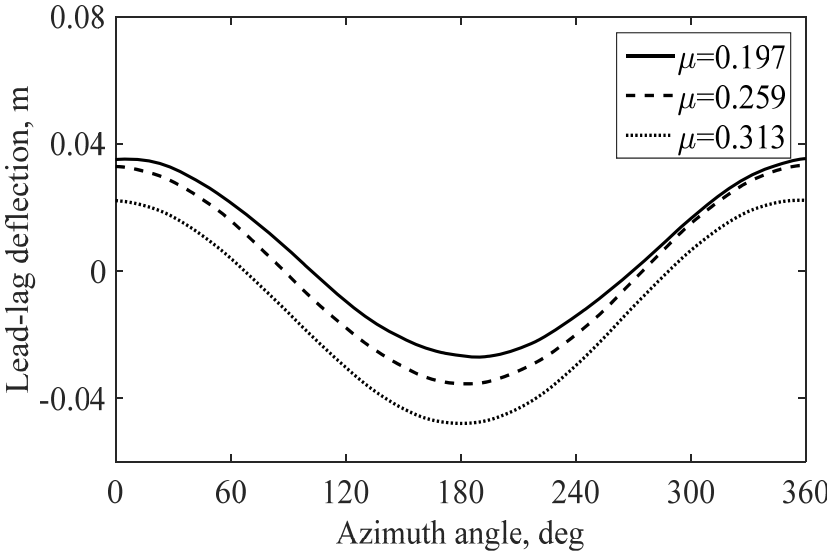

(b)

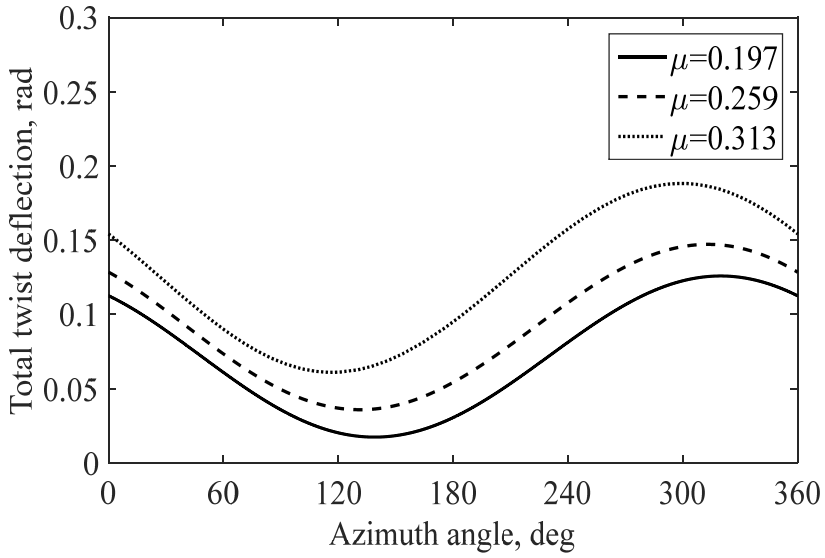

(c)

Fig. 9.8. Variations of the (a) flapping (b) lead-lag (c) total twist deflections at the tip of the helicopter rotor blade with azimuth angle for steady-state forward flight

Figures 9.8(a)–(c) describe the fully nonlinear characteristics of the steady-state, flapping, lead-lag, and twist deflections, respectively, varying with nondimensional time or azimuth angle in the forward flight at the tip of the helicopter rotor blade ($x/l = 1$) for different values of μ with necessary control parameters listed in Table 8.6. The corresponding solutions are obtained numerically from the generalized MOL. The total twist deflection in Fig. 9.8(c) represents the combination of the pitch, twist, cyclic, and torsional displacements at the blade tip. For forward flight, the blade flapping, lead-lag, and twist deflections are all periodic in nature after one rotor revolution, therefore, instead of using the dimensional time directly, the nondimensional time, i.e., the azimuth angle is used to show the variations of the deflections. It is to note that, V_{NE} for the Bo 105 helicopter is approximately 75 m/s which corresponds to $\mu = 0.34$.

From Fig. 9.8(a), the maximum values of the nonlinear flapping deflections for all the advance ratios can be located at $\psi = 55°$ and in overall nature, the peak-to-peak flapping displacement increases as μ increases. This is due to the higher values of the collective inputs for higher advance ratios. Similar behavior is visualized for the lead-lag displacement in Fig. 9.8(b), however, in a different form. The positive lead-lag amplitudes start decreasing for all the advance ratios crossing the respective equilibrium positions to reach the negative peak amplitude at $\psi = 180°$ and then increase from there to regain the positive peaks until the cycle is

completed. The overall trend reveals that the peak-to-peak lead-lag amplitudes increase with μ, however, with no self-intersection unlike the flapping displacements. In general, the lead-lag displacements for all the advance ratios are much smaller in magnitudes than the flapping displacements because of much higher magnitude of the lift force compared to drag and greater in-plane bending stiffness than the out-of-plane bending stiffness. For the twist distribution in Fig. 9.8(c), the higher the advance ratio, the greater the magnitude because of the larger values of the collective inputs and torsional deformations along with other control parameters. Nonetheless, the peak-to-peak magnitudes of the total twist increase very slightly with the increase of the advance ratios indicating that the overall range of the twist displacement is not that sensitive to the corresponding change in the advance ratio.

Although in forward flight, the overall amplitudes of the responses for the three DOFs increase with μ, the azimuth positions at which the peaks occur are different for different DOFs. While the maximum flap magnitude is observed at $\psi = 55°$, the highest positive lead-lag displacement occurs at $\psi = 0°$ for all the advance ratios. Moreover, for the retreating side of the disk, the azimuth positions of the lower peaks of the flapping displacements continue shifting to the right in Fig. 9.8(a) which are the reverse for the total twisting deflections as can be seen from Fig. 9.8(c).

9.2.4 Variations of the Rotor Blade Velocities with Nondimensional Time for Steady-State Forward Flight

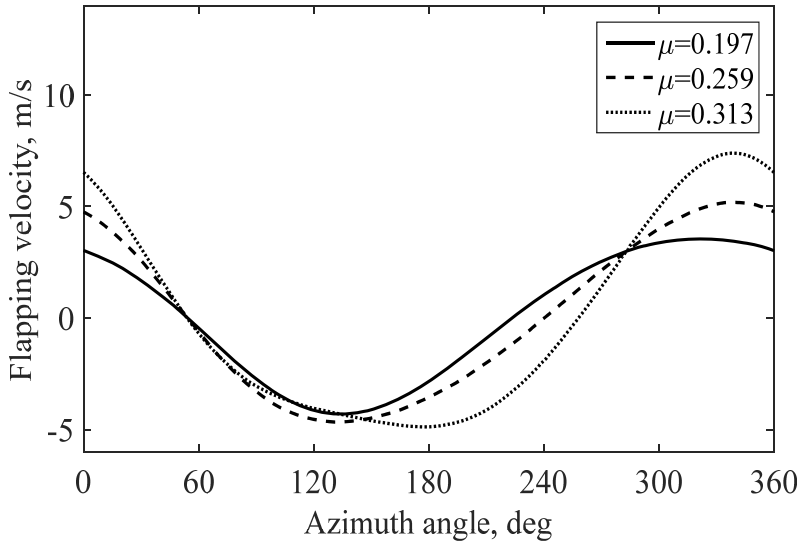

(a)

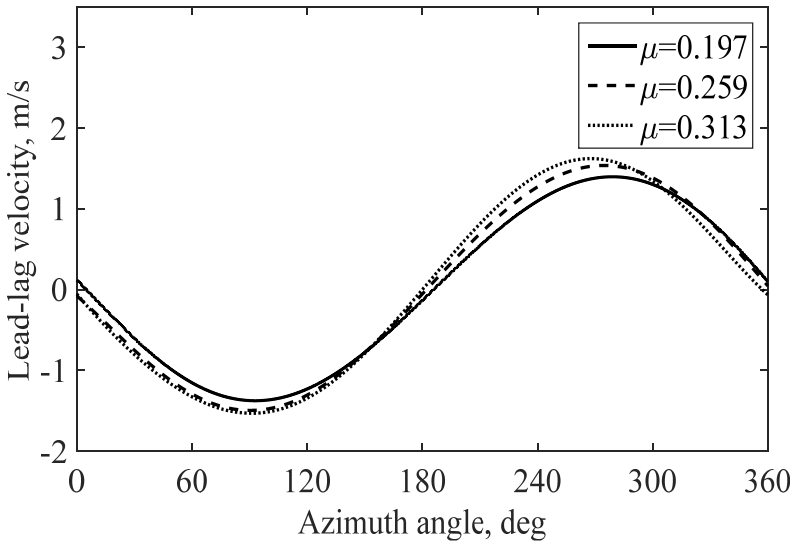

(b)

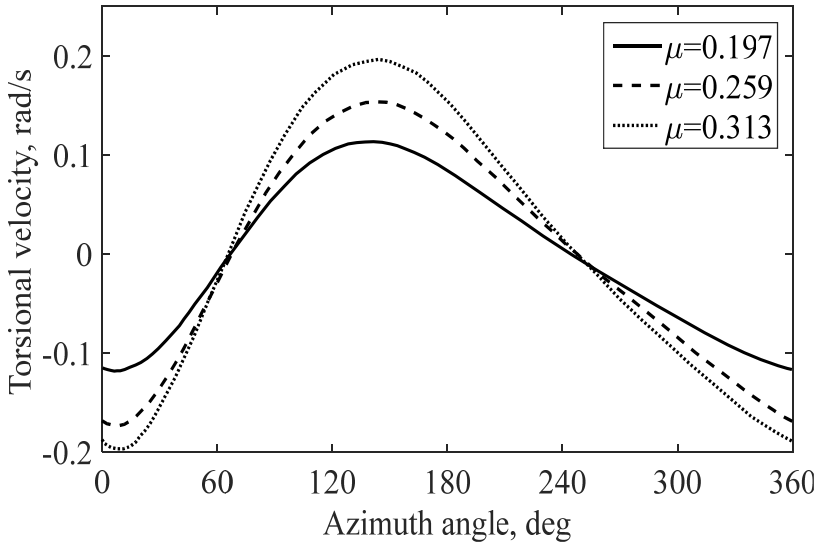

(c)

Fig. 9.9. Variations of the (a) flapping (b) lead-lag (c) torsional velocities at the tip of the helicopter rotor blade with azimuth angle for steady-state forward flight

Figures 9.9(a)–(c) describe the nonlinear velocity distributions of the coupled DOFs varying with the azimuth angle for the steady-state forward flight at the tip of the helicopter rotor blade ($x/l = 1$) for different advance ratios. Similar to the displacements, the velocity curves are also periodic in nature. From Fig. 9.9(a), the peak-to-peak deflections of the velocity curves increase as μ increases. For all values of μ, the maximum flapping velocity occurs at the retreating side of the rotor disk. The azimuth locations giving zero flapping velocities for each μ

represent the corresponding locations of the maximum and the minimum flapping displacements as can be seen from Fig. 9.8(a). Similar to flapping velocities, the lead-lag velocities in Fig. 9.9(b) give the highest magnitudes in the retreating side of the disk and the corresponding azimuth locations for each μ indicate the zero equilibrium positions for the lead-lag displacements. Compared to the flapping velocities, the lead-lag velocities do not show large deviations from each other for different advance ratios. From Fig. 9.9(c), unlike flapping or lead-lag velocities, the torsional velocities appear with peak values in the advancing side of the rotor disk. The azimuth locations representing the maximum or the minimum values for the flapping, lead-lag, and torsional velocities are the points of inflection in the corresponding displacement curves where the changes in the direction of curvatures occur.

9.2.5 Variations of the Rotor Blade Deflections with Nondimensional Time for Unsteady Motion in Forward Flight

Figure 9.10 gives the unsteady nonlinear dynamic behaviors of the coupled DOFs varying with the azimuth angle at the tip ($x/l = 1$) of the rotor blade for $\mu = 0.197$. From Fig. 9.10, the unsteady responses show deviations from the steady-state responses depicted in Fig. 9.8 in terms of the magnitudes of the DOFs and relocations of the azimuth angles representing the maximum or the minimum values of the deflections. From Fig. 9.8(a), the maximum blade tip flapping deflection for $\mu = 0.197$ is 0.206 m which takes place on the advancing side of the rotor

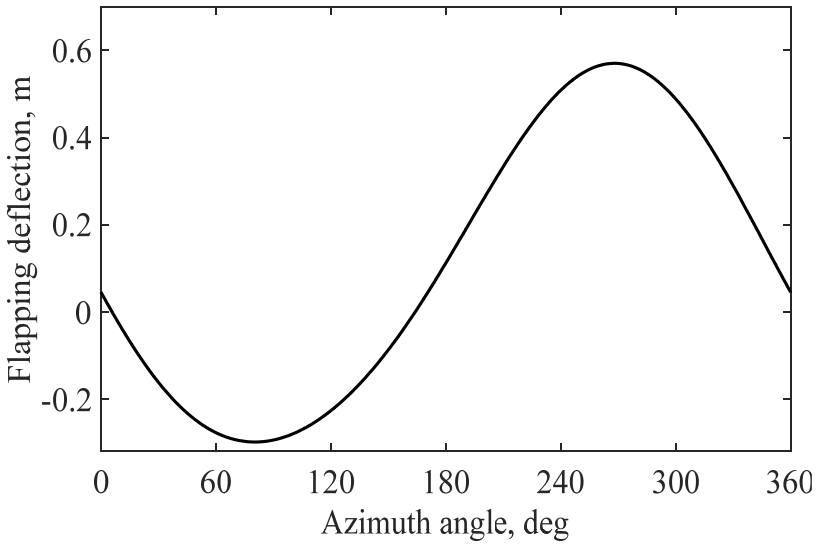

(a)

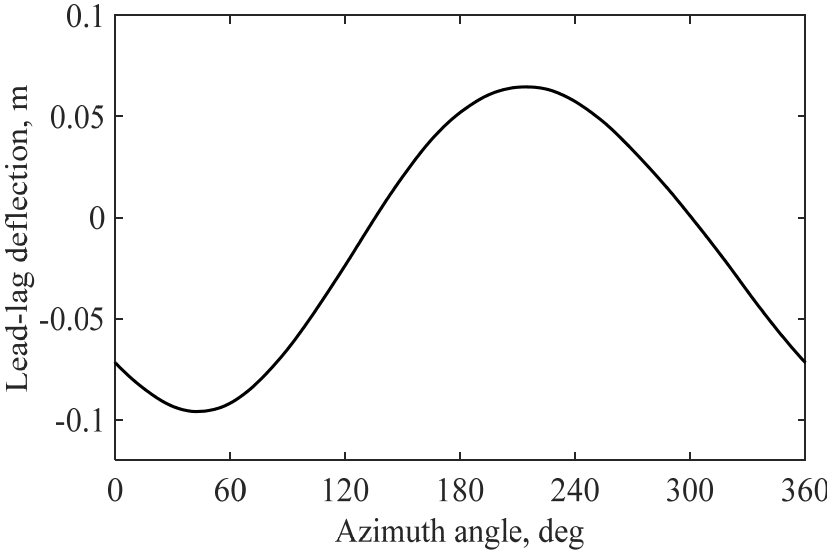

(b)

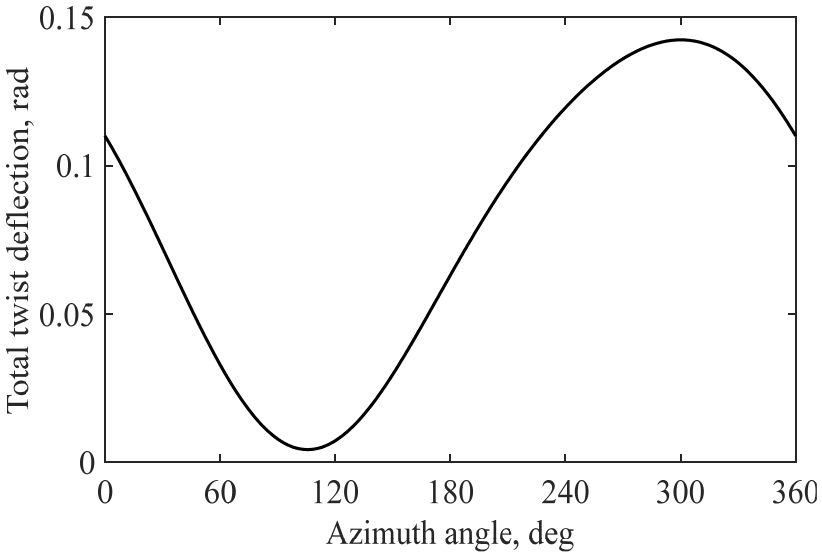

(c)

Fig. 9.10. Variations of the (a) flapping (b) lead-lag (c) total twist deflections at the tip of the helicopter rotor blade with azimuth angle for unsteady forward flight with $\mu = 0.197$

disk, whereas for the unsteady motion in Fig. 9.10(a), the maximum flapping displacement is 0.570 m and occurring on the retreating side of the disk. The rise in the magnitude of the flapping deflection of the rotor blade for the unsteady forward flight is due to the addition of the unsteady lift force which is a strong function of $\dot{\alpha}$ containing the time-variations of the torsional deformation and the cyclic parameters. Therefore, it is logical to expect the shifting of the peak value of the flapping response on the retreating side of the rotor blade.

Since the unsteady lift is also used to calculate the total in-plane aerodynamic load, the peak-to-peak magnitude of the unsteady lead-lag deflection is also increased as seen in Fig. 9.10(b) compared to Fig. 9.8(b) along with the repositioning of the peak value at an azimuth angle near the vicinity of the starting region of retreating side of the rotor disk. However, to predict the unsteady twisting deformation at the tip of the rotor blade, Fig. 9.10(c) is observed to be quite close to Fig. 9.8(c) in terms of the magnitudes of the peak values and the corresponding azimuth locations which justify that the unsteady motion has comparatively less influence over the twisting response compared to the bending response.

CHAPTER 10

Conclusions and Future Work

10.1 Conclusions

The dynamic response of the Bo 105 helicopter rotor blade is analyzed at the hovering and the forward flights in terms of three coupled degrees-of-freedom; flap, lead-lag, and torsional motions; by solving the coupled governing equations numerically. A model of the cross-section of the Bo 105 helicopter rotor blade is proposed for which a semi-analytical method is developed to estimate the sectional properties. Those properties are used for the free vibration analysis of the blade having the proposed section to estimate the natural frequencies for both the rotating and the nonrotating cases. The coupled natural frequencies are estimated analytically from the modified Galerkin method and are compared to that obtained from the finite element model. The forced response of the Bo 105 helicopter rotor blade is carried out for hovering and forward flights. The large flapping and inflow angles are introduced in the mathematical model of the forward flight. A robust numerical algorithm is developed to solve the nonlinear governing differential equations by the generalization of the method of lines. The numerical solution is presented for both hovering and forward flights in terms of the steady-state time-varying deflections for the three degrees-of-freedom. The steady-state displacements and velocities of the rotor blade are estimated for the forward flight for different advance ratios. The unsteady response of the rotor blade for the forward flight is analyzed at a specific advance ratio to compare with the corresponding steady-state response. The following conclusions are drawn from the analysis:

1. The magnitudes of the nonrotating case frequencies are smaller than those of the rotating case for flapping, lead-lag, and torsional modes. The reason behind this phenomenon is the additional stiffness developed by the centrifugal force which significantly affects the bending governed modes more than the torsion governed modes.

2. The effect of the coupling between flapping and torsion is not very significant due to the relative closeness of the locations of the centroid and the shear center of the proposed cross-section.

3. The deviations between the analytical and the finite element torsion governed frequencies are higher than those calculated for the bending governed ones. This is because of the more inaccuracy in the estimated torsional stiffness than the bending stiffness and is compensated by the additional rotational stiffness developed by the rotating blade.

4. The effectiveness of the solution strategy for the free, coupled flapping-lead-lag-torsional vibration for a rotating blade depends on the strength of the coupling, the slenderness of the blade, and the magnitude of the rotational stiffness. The uncoupled vibration solution strategy can offer an approximate solution which is reasonably accurate for a slender blade with relatively high rotational stiffness and a closer shear center relative to the centroid.

5. The forced response analysis of the helicopter rotor blade for the forward flight involves a nonlinear mathematical model. Therefore, a numerical technique is introduced for solving the nonlinear mathematical model.

6. A generalization of the method of lines is performed for one-dimensional forced beam vibration problems with coupled degrees-of-freedom. The developed algorithm is robust, easy to implement, and applicable to any number of one-dimensional, linear/nonlinear, coupled/uncoupled, steady-state/transient, forced beam vibration problems having single/multiple degrees-of-freedom with classical/moving boundary conditions. This generalized numerical method is used for solving the corresponding mathematical models of the forced response of the rotor blade at hovering and forward flights.

7. The time-varying flapping, lead-lag, and torsional deflections show oscillatory behaviors for the hovering flight. The tendency of oscillation for the torsional degree-of-freedom is found greater than that of the bending degrees-of-freedom. The deflections are generated due to the input forcing functions which are harmonic in nature.

8. The variations of flapping, lead-lag, and torsional deflections of the rotor blade around the azimuth are analyzed for different advance ratios for the steady-state forward flight. The coupled responses of the blade are nonlinear and periodic in nature. Moreover, the azimuth angle positions at which the deflections are the maximum or the minimum, vary for different degrees-of-freedom.

9. The peak-to-peak deflections for the steady-state forward flight are increased with the increase of the advance ratios. The maximum flapping deflection takes place in the advancing side of the rotor disk. The negative peak amplitude for the lead-lag displacement takes place at the transition region between the advancing and the retreating sides of the rotor disk.

10. The higher the advance ratio, the greater the magnitude of the total twist displacement for the steady-state forward flight. This is because of the higher values of the collective inputs and torsional deformations along with other control parameters. The peak-to-peak magnitudes of the total twist increase very slightly with the increase of the advance ratios which indicates that the overall range of the twist displacement is not that sensitive to the corresponding change in the advance ratio.

11. The steady-state velocity distributions of the rotor blade at the forward flight are nonlinear and periodic in nature, similar to the blade displacements and indicate that the peak-to-peak velocity magnitudes increase with the advance ratios. The maximum flapping and lead-lag velocities occur at the retreating side of the rotor disk and the torsional velocities appear with peak values in the advancing side of the rotor disk.

12. The characteristics of the dynamic response of the rotor blade for the unsteady motion of the airfoil at the forward flight are periodic and nonlinear similar to that of the steady-state response. However, the unsteady flapping and lead-lag responses show deviations from the steady-state case in terms of the increased magnitudes of the displacements and the relocated positions of the azimuth angles representing the maximum or the minimum displacements in one complete rotor revolution.

13. The peak-to-peak flapping deflection of the rotor blade for the unsteady forward flight is higher than that of the steady-state case due to the addition of the unsteady lift force to the steady lift which is a strong function of the time-dependent pitch angle containing the time-variations of the torsional deformation and the cyclic parameters. This additional unsteady lift is also responsible for the increased peak-to-peak lead-lag displacement.

14. The unsteady behavior of the total twist displacement of the rotor blade in the forward flight is similar to that of the steady-state case in terms of the magnitudes of the peak values and

the corresponding azimuth locations which justify that the unsteady motion has a less influence on the total twisting response than that of the bending case.

15. The method of lines is one of the few viable numerical solutions to select for the forced beam vibration problems where the force varies nonlinearly depending on the time derivative or the space derivative of the solution.

16. The periodicity of the solution for the lead-lag deflection requires more iterations to provide the converged results because of the much lower aerodynamic damping for the lead-lag motion compared to that for the flapping motion.

17. The solution of the one-dimensional vibration problem by the method of lines can be extended to two-dimensional vibration problems. This generalized method can be applied with the appropriate solver depending on the stiff or the less stiff nature of the problems.

10.2 Future Work

In this study, the dynamic analysis of the hingeless helicopter rotor blade is carried out in terms of the natural frequencies and the steady-state, forced blade response at hovering and forward flights for coupled, three degrees-of-freedom of motion. The unsteady blade response for the forward flight is also analyzed. The total task combines both the aerodynamic and structural analyses and can be improved further by following the recommendations below:

1. For the steady-state blade response at hovering and forward flights, the effects of compressibility and dynamic stall are neglected in this study and can be included for further analysis. At the forward flight on the retreating blade region, the angle of attack is higher than that on the advancing side to overcome the asymmetry of lift. However, the presence of the unsteady aerodynamic environment assisted by the high angle of attack results in the dynamic stall for which the aerodynamic loading on the helicopter rotor blade is totally different.

2. The comprehensive forced response analysis can be conducted for other different models of hingeless helicopter rotors and for other different rotor types, e.g., articulated and semi-rigid rotors including the three degrees-of-freedom to ensure the generalization of the mathematical model. The mathematical model can be modified to include the characteristics of

the tapered helicopter rotor blades which take into account the varying mass per unit length of the blade thereby justifying the efficacy of the numerical model.

3. The climbing velocity may be included in the aerodynamics of hovering and forward flights which changes the corresponding induced inflow distribution as well as the cyclic control angles.

4. The fuselage drag is recommended to be considered for estimating the total power required for operating the helicopter.

5. The dynamic analysis of the tail rotor blade of the helicopter including the three degrees-of-freedom might contribute to reveal some new insights to explain the overall behavior of the helicopter for both the steady and the unsteady aerodynamic environments. The inclusion of the mathematical model of the forced response of the tail rotor blades is encouraged in parallel to that of the main rotor blades.

References

Abbott, I.H., Doenhoff, A.E.V., Stivers, Jr., L.S., 1945. Summary of Airfoil Data. NACA Report 824, Langley Memorial Aeronautical Laboratory, Virginia, USA.

Ahmed, H., Ahmed, R., Indaleeb, M.M., Banerjee, S., 2018. Multifunction acoustic modulation by a multi-mode acoustic metamaterial architecture. Journal of Physics Communications, 2(11), 1–11.

Aksencer, T., Aydogdu, M., 2015. Flapwise vibration of rotating composite beams. Composite Structures. 134, 672–679.

Alonso, R.L., Ribeiro, P., 2008. Flexural and torsional non-linear free vibrations of beams using a p-version finite element. Computers and Structures, 86(11–12), 1189–1197.

Banerjee, J.R., Williams, F.W., 1994. Coupled bending-torsional dynamic stiffness matrix of an axially loaded Timoshenko beam element. International Journal of Solids and Structures. 31(6), 749–762.

Bekhoucha, F., Rechak, S., Duigoub, L., Cadoub, J.M., 2016. Nonlinear free vibrations of centrifugally stiffened uniform beams at high angular velocity. Journal of Sound and Vibration. 379, 177–190.

Benedict, M., Jarugumilli, T., Chopra, I., 2013. Effect of rotor geometry and blade kinematics on cycloidal rotor hover performance. Journal of Aircraft. 50(5), 1340–1352.

Bouhamidi, A., Jbilou, K., 2013. A fast block Krylov implicit Runge-Kutta method for solving large-scale ordinary differential equations, in: Optimization, Simulation, and Control, Springer, New York, USA, pp. 319–330.

Bousman, W.G., 2003. Aerodynamic characteristics of SC1095 and SC1094 R8 airfoils. NASA Technical Paper 212265, Ames Research Center, California, USA.

Bramwell, A.R.S., Done, G., Balmford, D., 2001. Bramwell's Helicopter Dynamics. AIAA, Oxford, England.

Brooks, T.F., Jolly, Jr., J.R., Marcolini, M.A., 1988. Helicopter main-rotor noise: determination of source contributions using scaled model data. NASA Technical Paper 2825, Langley Research Center, Virginia, USA.

Carrera, E., Filippi, M., Mahato, P.K., Pagani, A., 2016. Free-vibration tailoring of single- and multi-bay laminated box structures by refined beam theories. Thin-Walled Structures. 109, 40–49.

Carrión, M., Woodgate, M., Steijl, R., Barakos, G.N., Gomez-Iradi, S., Munduate, X., 2015. Understanding wind-turbine wake breakdown using computational fluid dynamics. AIAA Journal. 53(3), 588–602.

Chapra, S.C., Canale, R.P., 2015. Numerical Methods for Engineers, seventh ed. McGraw-Hill Education, New York, USA.

Dassault Systèmes, 2015. SolidWorks, Software Package, Version 2015. Waltham, Massachusetts, USA.

Dassault Systèmes SIMULIA Corporation, 2012. Abaqus, Software Package, Version 6.12. Providence, Rhode Island, USA.

D'Ambrosio, R., Moccaldi, M., Paternoster, B., 2017. Adapted numerical methods for advection–reaction–diffusion problems generating periodic wavefronts. Computers and Mathematics with Applications. 74(5), 1029–1042.

Dekker, K, 2009. Partitioned Krylov subspace iteration in implicit Runge–Kutta methods. Linear Algebra and its Applications. 431, 488–494.

Farrugia, R., Sant, T., Micallef, D., 2016. A study on the aerodynamics of a floating wind turbine rotor. Renewable Energy. 86, 770–784.
Fossati, M., 2015. Evaluation of aerodynamic loads via reduced-order methodology. AIAA Journal. 53(8), 2389–2405.
Friedmann, P.P., Glaz, B., Palacios, R., 2009. A moderate deflection composite helicopter rotor blade model with improved cross-sectional analysis. International Journal of Solids and Structures. 46, 2186–2200.
Friedmann, P.P., Tong, P., 1972. Dynamic nonlinear elastic stability of helicopter rotor blades in hover and in forward flight. NASA Contractor Report 114485, Aeroelastic and Structural Research Laboratory, Cambridge, Massachusetts, USA.
Ganesh, B., Komerath, N., 2004. Unsteady aerodynamics of rotorcraft in ground effect. AIAA Paper, Fluid Dynamics Meeting, Portland, Oregon, USA.
Ganguli, R., Chopra, I., 1996. Aeroelastic optimization of a helicopter rotor with two-cell composite blades. AIAA Journal. 34(4), 835–841.
Ganguli, R., 2002. A fuzzy logic system for ground based structural health monitoring of a helicopter rotor using modal data. Journal of Intelligent Material Systems and Structures. 12(6), 397–407.
Garinis, D., Dinulović, M., Rašuo, B., 2012. Dynamic analysis of modified composite helicopter blade. Faculty of Mechanical Engineering Transactions. 40(2), 63–68.
Genta, G., 2005. Dynamics of Rotating Systems. Springer, New York, USA.
Gerstenberger, W., Wagner, R.A., Kelley, B., Ellis, C.W., 1957. The rotary round table: How can helicopter vibrations be minimized. Journal of the American Helicopter Society. 2(3).
Ghafari, E., Rezaeepazhand, J., 2016. Vibration analysis of rotating composite beams using polynomial based dimensional reduction method. International Journal of Mechanical Sciences. 115–116, 93–104.
Gibertini, G., Boniface, J.C., Zanotti, A., Droandi, G., Auteri, F., Gaveriaux, R., Pape, A.L., 2015. Helicopter drag reduction by vortex generators. Aerospace Science and Technology. 47, 324–339.
Gilad, M., 2011. Evaluation of Flexible Rotor Hover Performance in Extreme Ground Effect. Master's Thesis, Department of Aerospace Engineering, University of Maryland.
Glauert, H. 1926. A general theory of the autogyro. Reports and Memoranda No. 1111, Aeronautical Research Council.
Goulos, I., Pachidis, V., Pilidis, P., 2015. Flexible rotor blade dynamics for helicopter aeromechanics including comparisons with experimental data. The Aeronautical Journal. 119(1213), 301–342.
Guo, J.X., Xiang, J.W., 2004. Composite rotor blade design optimization for vibration reduction with aeroelastic constraints. Chinese Journal of Aeronautics. 17(3), 152–158.
Han, D., Pastrikakis, V., Barakos, G.N., 2016a. Helicopter flight performance improvement by dynamic blade twist. Aerospace Science and Technology. 58, 445–452.
Han, D., Pastrikakis, V., Barakos, G.N., 2016b. Helicopter performance improvement by variable rotor speed and variable blade twist. Aerospace Science and Technology. 54, 164–173.
Hashemi, S.M., Richard, M.J., 2000. Free vibrational analysis of axially loaded bending-torsion coupled beams: A dynamic finite element. Computers and Structures. 77(6), 711–724.
HexWeb Honeycomb Attributes and Properties. Hexcel Corporation, Stamford, Connecticut, USA.

Hodges, D.H., Atilgan, A.R., Fulton, M.V., Rehfield, L.W., 1991. Free-vibration analysis of composite beams. Journal of the American Helicopter Society. 36(3), 36–47.
Hodges, D.H., Ormiston, R.A., 1976. Stability of elastic bending and torsion of uniform cantilever rotor blades in hover with variable structural coupling. NASA Technical Note D-8192, Ames Research center, California, USA.
Hopkins, S.A., Ormiston, R.A., 2003. An examination of selected problems in rotor blade structural mechanics and dynamics. 59th Annual Forum of the American Helicopter Society, Phoenix, Arizona, USA.
Houbolt, J.C., Brooks, G.W., 1957. Differential equations of motion for combined flapwise bending, chordwise bending, and torsion of twisted nonuniform rotor blades. NACA Technical Note 3905, Langley Aeronautical Laboratory, Virginia, USA.
Izzo, G., Jackiewicz, Z., 2017. Highly stable implicit-explicit Runge-Kutta methods. Applied Numerical Mathematics. 113, 71–92.
Islam, A.B.M.I., Kelkar, A., 2017a. Prospects and challenges of nanomaterial engineered prepregs for improving interlaminar properties of laminated composites—a review. MRS Communications. 7(2), 102–108.
Islam, A.B.M.I., Kelkar, A., 2017b. Fabrication and characterization of nanofiber enhanced prepregs. MRS Advances. 2(17), 951–956.
Jardin, T., Doué, N., Prothin, S., Moschetta, J.M., 2016. Numerical analysis of pitching-rotor aerodynamics. Journal of Fluids and Structures. 62, 172–186.
Jin, X., Koya, N.G., 2016. Prediction of coupled torsional–axial vibrations of drilling tool with clamping boundary conditions. CIRP Journal of Manufacturing Science and Technology. 13, 24–36.
Jin, Y., Yu, L., Yong, L., 2015. Vibration reduction of a bearingless helicopter rotor with composite tailored couplings. Procedia Engineering. 99, 1372–1379.
Johnson, W., 1994. Helicopter Theory. Dover Publications, Princeton, New Jersey, USA.
Kalogiratou, Z., Monovasilis, T., Psihoyios, G., Simos, T.E., 2014. Runge–Kutta type methods with special properties for the numerical integration of ordinary differential equations. Physics Reports. 536(3), 75–146.
Karimi, A.H., Ziaei-Rad, S., 2015. Vibration analysis of a beam with moving support subjected to a moving mass travelling with constant and variable speed. Communications in Nonlinear Science and Numerical Simulation. 29(1–3), 372–390.
Kaya, M.O., Ozgumus, O.O., 2007. Flexural-torsional-coupled vibration analysis of axially loaded closed-section composite Timoshenko beam by using DTM. Journal of Sound and Vibration. 306, 495–506.
Leishman, J.G., 2006. Principles of Helicopter Aerodynamics. Cambridge University Press, New York, USA.
Li, Q., Kamada, Y., Maeda, T., Murata, J., Nishida, Y., 2016a. Effect of turbulent inflows on airfoil performance for a horizontal axis wind turbine at low Reynolds numbers (Part II: Dynamic pressure measurement). Energy. 112, 574–587.
Li, Q., Kamada, Y., Maeda, T., Murata, J., Nishida, Y., 2016b. Visualization of the flow field and aerodynamic force on a horizontal axis wind turbine in turbulent inflows. Energy. 111, 57–67.
Lind, A.H., Jones, A.R., 2016. Unsteady airloads on static airfoils through high angles of attack and in reverse flow. Journal of Fluids and Structures. 63, 259–279.

Loewy, R.G., 1980. Helicopter vibrations: a technological perspective. Journal of the American Helicopter Society. 29(4), 4–30.
Lynch, L.E., Prosser, D.T., Smith, M.J., 2014. An efficient actuating blade model for unsteady rotating system wake simulations. Computers and Fluids. 92, 138–150.
Majhi, J.R., Ganguli, R., 2008. Modeling helicopter rotor blade flapping motion considering nonlinear aerodynamics. Computer Modeling in Engineering and Sciences. 27(1), 25–36.
MathWorks Corporation, 2015. MATLAB, Software Package, Version R2015a. Natick, Massachusetts, USA.
Murugan, S., Ganguli, R., Harursampath, D., 2008. Robust aeroelastic optimization of composite helicopter rotor. International Conference on Engineering Optimization, Rio de Janeiro, Brazil.
Murugan, S., Ganguli, R., 2008. Influence of inflow models on helicopter aeroelastic optimization. Computational Fluid Dynamics Journal. 16, 444–455.
Panda, B., Chopra, I., 1986. Dynamic stability of hingeless and bearingless rotors in forward flight. Computers and Mathematics with Applications. 12A(1), 111–130.
Park, S., Baek, N., Ryu, K., 2012. A dynamics model of rotor blades for real-time helicopter simulation. International Journal of Multimedia and Ubiquitous Engineering. 7(2), 209–220.
Pertsch, A., Sawodny, O., 2016. Modeling and control of coupled bending and torsional vibrations of an articulated aerial ladder. Mechatronics. 33, 34–48.
Peters, D.A., He, C.J., 1989. Comparison of measured induced velocities with results from a closed-form finite state wake model in forward flight. 45th Annual Forum of the American Helicopter Society, Boston, Massachusetts, USA.
Peters, D.A., Hsieh, M.A., Torrero, A., 2007. A state-space airloads theory for flexible airfoils. Journal of the American Helicopter Society. 52(4), 329–342.
Peterson, R.L., 1995. Full-scale hingeless rotor performance and loads. NASA technical memorandum 110356, Ames Research Center, California, USA.
Pitt, D.M., Peters, D.A., 1981. Theoretical prediction of dynamic inflow derivatives. Vertica. 5(1), 21–34.
Product Information-Rohacell RIST. Evonik Industries, Essen, Germany.
Prouty, R.W., 2002. Helicopter Performance, Stability, and Control. Krieger Publishing Company, Florida, USA.
Qin, Y., Li, X., Yang, E.C., Li, Y.H., 2016. Flapwise free vibration characteristics of a rotating composite thin-walled beam under aerodynamic force and hygrothermal environment. Composite Strucutres. 153, 490–503.
Ramanujam, R., Rao, S., Abhishek, 2015. Stability analysis of variable geometry helicopters. 4th Asian/Australian Rotorcraft Forum, Bengaluru, Karnataka, India.
Rand, O., Barkai, S.M., 1995. Numerical evaluation of the equations of motion of helicopter blades with symbolic exactness. Journal of the American Helicopter Society. 40(1), 59–71.
Rasheed, H.A., 2014. Strengthening Design of Reinforced Concrete with FRP. CRC Press, Boca Raton, Florida, USA.
Salkind, M., Hollister, G., 1973. Applications of Composite Materials. ASTM, Pennsylvania, USA.
Sarker, P., Theodore, C.R., Chakravarty, U.K., 2016. Vibration analysis of a composite helicopter rotor blade at hovering condition. ASME International Mechanical Engineering Congress and Exposition, Phoenix, Arizona, USA.

Sheikh, A.H., Asadi, A., Thomsenb, O.T., 2015. Vibration of thin-walled laminated composite beams having open and closed sections. Composite Structures. 134, 209–215.
Shinoda, P.M., 2004. Investigation of a full-scale wide chord blade rotor system in the NASA Ames 40- by 80-foot wind tunnel. American Helicopter Society 4th Decennial Specialist's Conference on Aeromechanics, San Francisco, California, USA.
Staley, J.A., 1976. Validation of rotorcraft flight simulation program through correlation with flight data for soft-in-plane hingeless rotors. USAAMRDL Technical Report 75-50, Virginia, USA.
Taha, H.E., Hajj, M.R., Beran, P.S., 2014. State-space representation of the unsteady aerodynamics of flapping flight. Aerospace Science and Technology. 34, 1–11.
Vasiliev, V.V., Morozov, E.V., 2013. Advanced Mechanics of Composite Materials and Structural Elements. Elsevier, Oxford, England.
Vu, N.A., Lee, J.W., 2015. Aerodynamic design optimization of helicopter rotor blades including airfoil shape for forward flight. Aerospace Science and Technology. 42, 106–117.
Wang, J., Jang, J., Chopra, I., 1988. Air resonance stability of hingeless rotors in forward flight. 14th European Rotorcraft Forum, Milan, Lombardy, Italy.
Wang, Q., Zhao, Q., 2016. Unsteady aerodynamic characteristics investigation of rotor airfoil under variational freestream velocity. Aerospace Science and Technology. 58, 82–91.
Yang, X., Yang, A., Si, J., 2015. Efficient numerical techniques for simulating a rotorcraft flow field with overlapping grids. AIAA Journal. 53(5), 1372–1383.
Youzera, H., Meftah, S.H., Challamel, N., Tounsia, A., 2012. Nonlinear damping and forced vibration analysis of laminated composite beams. Composites Part B: Engineering. 43(3), 1147–1154.
Yu, A.M., Yang, J.W., Nie, G.H., Yang, X.G., 2011. An improved model for naturally curved and twisted composite beams. Composite Structures, 93, 2322–2329.
Yuan, K.A., Friedmann, P.P., 1998. Structural optimization for vibratory loads reduction of composite helicopter rotor blades with advanced geometry tips. Journal of the American Helicopter Society. 43(3), 246–256.
Zaw, M.T., Tun, H.M., Naing, Z.M., 2014. Development of mathematical model and stability analysis for UAH. International Journal of Scientific and Research Publications. 4(5), 1–10.
Zhang, Z., Chen, P.C., Yang, S., Wang, Z., Wang, Q., 2015. Unsteady aerostructure coupled adjoint method for flutter suppression. AIAA Journal. 53(8), 2121–2129.
Zhao, J., 2005. Dynamic Wake Distortion Model for Helicopter Maneuvering Flight. Ph.D. Thesis, School of Aerospace Engineering, Georgia Institute of Technology.

Vita

The author was born in the city of Kishoreganj, Bangladesh and passed his early school and college years in Dhaka, Bangladesh. He obtained his B.S. in Mechanical Engineering in June 2007 from the Bangladesh University of Engineering and Technology. After graduation, he joined the Karnaphuli Fertilizer Company (KAFCO) in Chittagong, Bangladesh and served there up to April 2011 as a Mechanical Maintenance Engineer. He joined the Primeasia University in the Textile Engineering Department in June 2011 and worked as a lecturer for almost one year. In the Spring 2013, he joined the University of New Orleans to pursue his Ph.D. in Mechanical Engineering. In December 2014, as part of the Ph.D. program, he obtained his M.S. in Engineering and Applied Science with major in Mechanical Engineering.